MONASH University

Proximal Estimation of Soil Density using Sensing and Modelling

Amir Tophel

B.Tech, M.Tech

A thesis submitted for the degree of

Doctor of Philosophy at

Monash University in 2023

Department of Civil Engineering

Copyright notice

© *Amir Tophel* (*2023*).

I certify that I have made all reasonable efforts to secure copyright permissions for third-party content included in this thesis and have not knowingly added copyright content to my work without the owner's permission.

Abstract

The measurement of density or void ratio during the compaction of geomaterials, such as soils and unbound granular materials, is crucial for ensuring superior performance in road construction. However, estimating density evolution non-destructively and in real-time during the compaction process has been a challenging task. This research aims to develop a methodology that enables the non-destructive estimation of density in geomaterials during compaction. The research is structured around three objectives, to:

1. Systematically review different density measurement systems and their relationship with the constitutive behaviour of geomaterials during compaction.
2. Develop a simplified constitutive model to study the behaviour of geomaterials during compaction.
3. Develop a methodology utilizing advanced instrumentation and analytics to estimate the density of geomaterials during compaction in a proximal manner.

These objectives guide the development of a new approach to estimate soil density during the compaction process.

The first objective is addressed by reviewing density estimation and measurement techniques in earthwork construction, with a focus on the importance of quality assurance (QA) and quality control (QC) criteria in ensuring the quality and safety of infrastructure projects. Conventional field-based density measurement techniques are hazardous, slow, and limited to point-based measurements. Non-invasive surface-based techniques, such as the Moisture and Density Indicator (MDI), Electrical Resistivity Tomography (ERT), Electrical Density Gauge (EDG), and Ground Penetrating Radar (GPR), offer alternative approaches. However, these methods are more influenced by water content than density, limiting their applicability in certain scenarios. The chapter emphasizes the need for suitable constitutive models and explores physics-based and machine-learning approaches to address challenges in modelling unsaturated material behaviour and nonlinear compaction.

The second objective is addressed by developing a constitutive model based on two different laboratory-scale tests: the constant-stress test and the constant load test. The constant stress model developed in Chapter 4 is extended to a constant load model by considering the geometric relationship between contact area and incremental plastic deformation. The effect of moisture content, plasticity, and initial void ratio on the compaction process is investigated,

and simplified equations for dynamic parameters are proposed. This developed model provides insights into the behaviour of materials subjected to field compaction and can determine unknown parameters such as initial density.

To address the third objective, this study introduces a novel methodology that includes measuring surface deformation using advanced instrumentation. Accurate deformation measurement is achieved using Light Detection and Ranging (LiDAR) systems attached to rollers. Laser/LiDAR sensors, roll correction, and signal pre-processing are employed to minimize measurement errors in deformation. The use of multiple sensors and various models, such as 1-D compaction and machine learning-based classification, demonstrate the ability to estimate density with high accuracy.

This novel instrumentation enables the measurement of density during compaction with unprecedented accuracy, presenting advantages over conventional invasive and pointwise approaches. This ensures the expeditious construction and satisfactory functioning of roads while minimizing the occurrence of premature failures. Continual density measurement during compaction also facilitates the maintenance of density uniformity, reducing the potential for excessive differential deformations.

Publications during enrolment

Refereed papers:

1. **Tophel A**, Walker JP, Dutta TT, Kodikara J (2022) Theory-guided machine learning to predict density evolution of sand dynamically compacted under Ko condition. *Acta Geotechnica*. https://doi.org/10.1007/s11440-021-01431-2

2. **Tophel, A**, Walker, JP, Lu, Y., Kodikara, J (2022) Proximal Sensing of Density During Soil Compaction by Instrumented Roller. *Australian Geomechanics Journal*. 57, 161–169. (https://doi.org/10.56295/AGJ5739)

3. **Tophel A**, Walker JP, Dutta TT, Bodin D, Kodikara J (2023) Model development to predict dynamic interactions of roller and geomaterial using simulated roller compaction. *Transportation Geotechnics* 39:100946. (https://doi.org/10.1016/j.trgeo.2023.100946)

Patent Application

4. **Tophel A**, Kodikara J, Walker JP. (2021) Systems and methods for measuring/estimating geomaterial layer properties due to compaction. Patent Application: PCT/AU2021/051505. (https://patentscope.wipo.int/search/en/detail.jsf?docId=WO2023108190)

Refereed Conference paper

4. **Tophel A**, Walker JP, Dutta TT, Kodikara J. (2023). Using a Novel Instrumented Roller to Estimate Soil Dry Density During Compaction. In: Gomes Correia, A., Azenha, M., Cruz, P.J.S., Novais, P., Pereira, P. (eds) Trends on Construction in the Digital Era. ISIC 2022. Lecture Notes in Civil Engineering, vol 306. Springer, Cham. https://doi.org/10.1007/978-3-031-20241-4_38

Under review/working papers:

5. Tophel, A., Dutta, T. T., Walker, J. P., Bodin, D., & Kodikara, J. Effect of stress history and initial state on the evolution of mechanical response for granular soils. Submitted.

6. Tophel, A., Walker, J. P., Dutta, T. T. & Kodikara, J. Estimation of Material Density During Compaction Using Advanced Instrumentation. Manuscript under preparation.

Awards during enrolment

1. Monash University Postgraduate Publication Award (PPA) (June 2023)
2. Finalist, Australian Geomechanics Society (AGS) Best PhD research award (2022)
3. Monash Research Impact Fund of 50,000 AUD, Monash University (Oct 2022)
4. Monash University Postgraduate Travel grant to attend International Conference (Sept 2022)
5. Winner and People's choice award winner (3MT round, Department of Civil Engineering 2021)
6. People's choice award winner (3MT round, Faculty of Engineering 2021)
7. Runner up (3MT round, Monash Wild card entry 2021)
8. Monash University Graduate Scholarship (MGS) (2019)
9. Faculty of Engineering International Postgraduate Research Scholarship (FEIPRS) (2019)

Thesis including published works declaration

I hereby declare that this thesis contains no material which has been accepted for the award of any other degree or diploma at any university or equivalent institution and that, to the best of my knowledge and belief, this thesis contains no material previously published or written by another person, except where due reference is made in the text of the thesis.

This thesis includes two original papers published in peer reviewed journals and no submitted publications. The core theme of the thesis is to develop a methodology to estimate the geomaterial's density during compaction. The ideas, development and writing up of all the papers in the thesis were the principal responsibility of myself, the student, working within the Department of Civil Engineering under the joint supervision of Prof. Jayantha Kodikara, Prof. Jeffrey Walker, Dr Ye Lu.

The inclusion of co-authors reflects the fact that the work came from active collaboration between researchers and acknowledges input into team-based research. In the case of *Chapters 4 and 5* my contribution to the work involved the following:

Thesis Chapter	**Publication Title**	**Status**	**Nature and % of student contribution**	**Co-author name(s) Nature and % of Co-author's contribution***	**Co-author(s), Monash student Y/N***
Chapter 4	*Theory-guided machine learning to predict density evolution of sand dynamically compacted under Ko condition.*	Published	Data Curation, Methodology, Formal analysis, Writing – Original draft (75%)	Kodikara, J.- Conceptualisation, Review & Editing (10%) Dutta, T.T.- Methodology, Review & Editing (10%) Walker, J.- Review & Editing (5%)	N
Chapter 5	*Model development to predict dynamic interactions of roller and geomaterial using simulated roller compaction.*	Published	Methodology, Formal analysis, Writing – Original draft (65%)	Kodikara, J.- Conceptualisation, Review & Editing (10%) Dutta, T.T.- Methodology, Review & Editing (10%) Bodin, D.- Data Curation, Methodology, Review & Editing (10%) Walker, J.- Review & Editing (5%)	N

I have not renumbered sections of submitted or published papers in order to generate a consistent presentation within the thesis.

Student name: Amir Tophel

Student signature:

Date: 18/09/2023

I hereby certify that the above declaration correctly reflects the nature and extent of the student's and co-authors' contributions to this work. In instances where I am not the responsible author I have consulted with the responsible author to agree on the respective contributions of the authors.

Main Supervisor name: Prof. Jayantha Kodikara

Main Supervisor signature:

Date: 18/09/2023

This work is
dedicated to my
Amma and Abba
for their
continual love
and support

Acknowledgements

I would like to take this opportunity to express my heartfelt gratitude to the numerous individuals and organizations who have played a significant role in the completion of my thesis. Without their unwavering support, guidance, and contributions, this achievement would not have been possible.

First and foremost, I am immensely grateful to my main supervisor, Prof. Jayantha Kodikara. His exceptional guidance, support, and constant encouragement throughout this journey have been invaluable. His dedication, responsiveness, and expertise have shaped my research and significantly contributed to the success of my thesis. I consider myself truly fortunate to have had him as my supervisor.

I would also like to extend my deepest appreciation to my co-supervisor, Prof. Jeffrey Walker, and Dr. Ye Lu. Their valuable suggestions, motivation, and continuous guidance have been instrumental in shaping the direction and quality of my work. Their combined expertise and mentorship have provided me with invaluable insights and have greatly contributed to the success of my research.

I am grateful to Monash University and the Department of Civil Engineering for providing me with endless opportunities to enhance my technical and non-technical skills. The opportunities such as the 3 Minute Thesis competition, travel grants to attend conferences, the MGA mentorship program, and my involvement in the Civil Engineering Postgraduate Committee (CEPC) have all contributed to my growth and development as a researcher.

I would like to acknowledge the members of my PhD review panel, Prof. Wing Chiu, Dr. Asadul Haque, Dr. Yihai Fang, and Prof. Ranjith Pathegama Gamage, for their valuable suggestions and feedback. Their expertise and critical insights have greatly strengthened the quality and rigor of my work.

A special thanks goes to Dr. Troyee Dutta for his outstanding support in all of my publications and his invaluable insights during our discussions. His contributions have been truly appreciated. I would also like to express my gratitude to Dr. Didier Bodin from ARRB for providing the extra-large wheel tracker test data to extend my developed model. Additionally, I am thankful to all the technical staff of the Civil Engineering Department, especially Pascal Mater, John Beadle, John Rebolledo, Gordon Privitera, Richard Williamson, and Mike Leach,

for their assistance with the soil box experimental equipment. Their support has been instrumental in the successful execution of my research.

I am grateful for the collaborative experience with the members of the Smart Pavements Australia Research Collaboration (SPARC) Hub and Prof. Jeffrey Walker's group. Working with them has been a tremendous learning experience, and I appreciate their contributions to my research. A special shout-out goes to Dr. Arooran Sounthararajah, the Manager of SPARC Hub, for his exceptional support in handling all the contingencies during the experiment. I am also thankful to all the seniors, Leslie, Sameera, Rukshan, Ravin, and Ben, for their guidance and support throughout the research journey.

I would like to acknowledge the financial support provided by SPARC Hub, the Australian Research Council (ARC), Construction, Infrastructure, Mining and Concessions (CIMIC), and Engineering, Innovation, and Capability (EIC) activities. Their funding has been crucial in enabling the progress and success of my research.

I would also like to express my gratitude to all the professors and lecturers, including Professor Jayantha Kodikara, Dr. Asadul Haque, Associate Professor Ha Bui, Professor Malek Bouzza, and Dr. Parikshit Verma, who trusted me as a Teaching Associate (TA) for their units. This opportunity has allowed me to grow professionally and has introduced me to amazing colleagues such as TAs Yingnan, Shashika, Babak, Fiona, Betty, Zunaira, and many others. The time spent teaching has been undoubtedly the best part of my week.

I want to emphasize the importance of maintaining a balance between work and personal life, especially during the challenging times of the COVID-19 pandemic. I am deeply indebted to my colleagues Asanka, Chathuri, Felipe, Gopu, Harini, Liuxin, Mai, Rajitha, and Sutha for their companionship, outings, and dining gatherings, which have provided much-needed moments of relaxation and joy amidst the demands of my research. Special thanks to my mint partners Kaushal, Nikhil, Havi, and Arjoon for their company during these times. Many thanks to my friends from India, Himanshu, Rahul, Garg, Bhawana, Prem, Kalu, and Nikol whom I may have troubled during my frequent trips, but who always welcomed me with smiles on their faces. To all those mentioned and the countless others (Aman, Sumit, Akanksha, Tejashwini, Abhishek, Sai, Anand, Ankita) who have supported me along the way, I am sincerely grateful for their contributions and the beautiful memories we have created together.

Lastly, I would like to express my deepest gratitude to all my family members. To my mother, Amma, who would call me countless times every day just to ask if I had eaten something, your constant love and care have been my greatest motivation. To my father, Abba, you are my inspiration in life. Your dedication and hard work, even at your age, uplift me and remind me to persevere. To my elder brother, thank you for showing me the way from a young age and constantly motivating me to strive for excellence. I am incredibly proud to see my younger brother excelling in college, as his achievements inspire me. I also want to mention my beautiful sister, Ayesha, whose frequent video calls during office hours served as a stress buster. Lastly, I am deeply grateful for the blessings and support of my grandparents (Dada, Didi, Nani), as well as all my extended family members who have been a source of strength throughout my entire journey.

To everyone mentioned above and to countless others who have supported me in various ways, I extend my sincere appreciation and gratitude. Thank you for being a part of my journey and for contributing to the successful completion of my thesis.

Contents

List of Figures

List of Tables

Part 1: Introduction

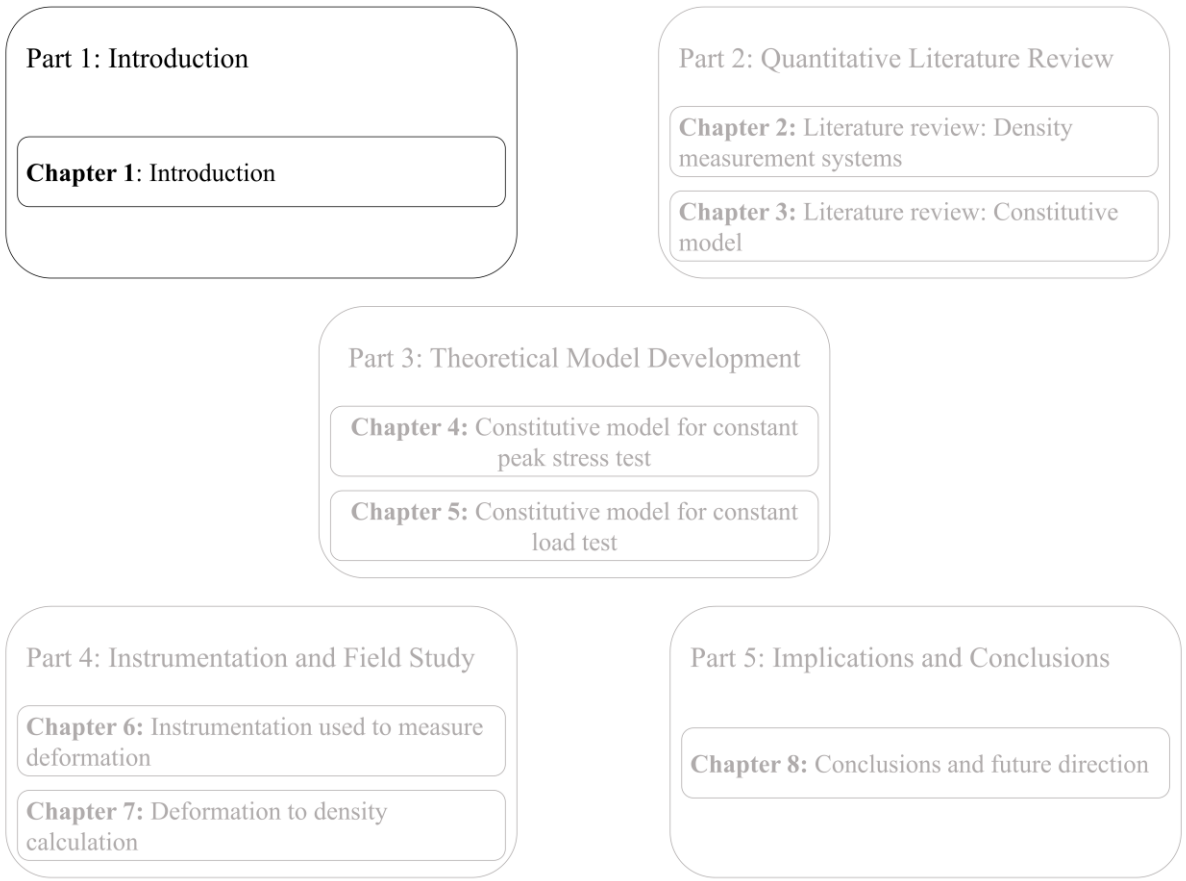

Chapter 1 Introduction

This thesis has developed a methodology to accurately estimate the density of geomaterials' during the compaction process. The objective was to employ a new and innovative approach to density estimation using instrumented rollers at different scales. The motivation behind this research arose from the crucial role of proper compaction in construction and mining activities. Compaction is critical in ensuring the stability, durability, and performance of various geomaterials, including soil and unbound granular material layers in construction projects such as buildings and roads. However, measuring the density of these materials accurately during compaction can be challenging and time-consuming using traditional methods. This thesis addressed this challenge by developing a methodology that enabled real-time density estimation during compaction. The objectives included investigating the feasibility of the proposed hypothesis, validating its effectiveness through experimental tests, and exploring various applications and potential benefits of the methodology.

1.1 Importance of Density

Estimating the ground condition competence of a construction area is essential for most construction works. This includes assessing the quality and characteristics of the geomaterial layers, such as soil, on which structures like buildings or roads are to be built. Inadequate soil compaction can lead to unsatisfactory performance of the constructed structure. For example, loosely compacted soil in road construction can result in a reduced service life and premature failure (Kodikara et al. 2018).

The geomaterial layers are typically constructed to achieve a designated density to ensure quality assurance (QA) of engineered soil compaction. Laboratory studies have demonstrated that higher material density generally improves rutting resistance, thereby enhancing a pavements' service life (Allen and Thompson 1974; Lekarp and Dawson 1998; Li et al. 2020). Additionally, minimising variability within the geomaterial layers is crucial to reducing serviceability failures caused by excessive differential deformations. To achieve the desired density, materials are compacted in layers using different types of rollers, depending on the specific material being used. Figure 1-1 depicts a typical cross-section illustrating the layers of a road section. Compacting loose material reduces air content, densifying the material. Increased density brings particles closer together, improving load-bearing capacity (Figure

1-2). Higher density also helps prevent settlement/rutting, reduces water seepage, and minimises contraction.

Not only is under-compaction a concern, but over-compaction can also pose problems. It is recommended to compact materials close to their maximum dry density (MDD) and optimum moisture content corresponding to the optimum degree of saturation (S_{ropt}). Based on experimental evidence, Tatsuoka and Gomes Correia (2018) highlighted that S_{ropt} is mostly unique for a certain soil, regardless of the mode of compaction, whether by Proctor hammer or by field rollers. Kodikara (2012) and Kodikara et al. (2020) emphasised the significance of S_{ropt}, when the air phase is trapped in a relatively continuous water phase. Hence, attempts to compact beyond this state (S_{ropt}) result in the material becoming overly wet, leading to undesirable effects of "over-compaction", such as material heaving with multiple shear planes and loosening of the already compacted material due to chaotic motions of the roller (Anderegg and Kaufmann 2004; Liu et al. 2019). Furthermore, experimental evidence indicates that material compacted beyond the optimum saturation generally undergoes undesirable plastic deformation under repetitive loading, similar to what would be expected from traffic loading (Brown and Hyde 1975; Monismith et al. 1975; Lekarp and Dawson 1998).

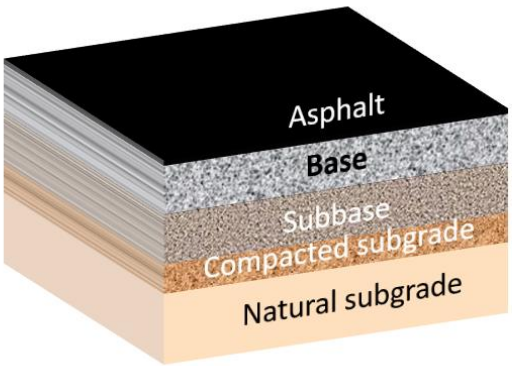

Figure 1-1. Typical cross-section of road pavement layers.

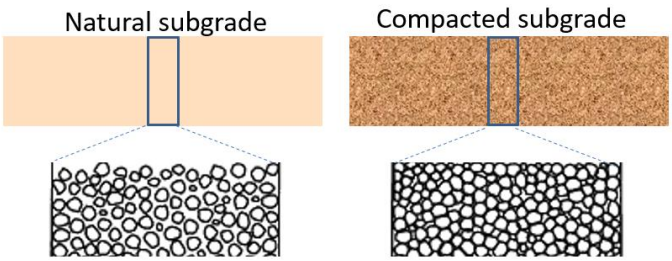

Figure 1-2. Particle packing in the natural subgrade and compacted subgrade.

In the realm of pavement construction, density measurements have traditionally been the cornerstone of quality control for compaction. Yet, there's an emerging trend where modulus and stiffness measurement methods are gaining traction. This shift is largely driven by the convenience and user-friendliness modulus techniques offer over their density counterparts. Furthermore, modulus-based approaches can determine the necessary material modulus for the mechanistic-empirical (ME) design of pavement layers. However, the adoption of these methods as a full-fledged replacement for density measurements in quality control is still in its infancy. Material properties such as modulus and stiffness often exhibit a non-linear relationship with density. As the density of a material increases, its modulus and stiffness tend to increase as well, but not always in a direct proportional manner. Stiff soils are not necessarily dense and can collapse when wetted. This non-linearity can be attributed to various intrinsic and extrinsic factors, including atomic arrangements, grain boundaries, and the presence of impurities or defects. S_{ropt} is an optimized value that is often used in material science to describe the optimal relationship between these properties for specific applications. Further discussion to this topic is discussed in Chapter 5.

1.2 Statement of problem

Despite its importance, no existing methodology can comprehensively estimate the density of a geomaterial layer during compaction across the entire compacted area. The traditional quality assurance measurements, such as nuclear density gauge (NDG), sand cone tests, and gravimetric tests based on field sampling, have limitations and issues. Invasive methods that require sampling or disturbance of the compacted area can disrupt the compaction process. These methods, including sand replacement, rubber balloon density, and borehole shear testing, provide density measurements but have a lag time of around 2-7 days for results to be available (Lee et al. 2017; Look 2020). The use of NDG involves harmful radiation emission and is time-consuming due to the need for multiple pointwise measurements over a large area.

With the advancement of mechanistic-empirical (ME) pavement design and performance-based construction specifications, there is a growing interest in methods that quantify performance-related soil parameters such as modulus and stiffness. Portable spot test methods, including lightweight deflectometer (LWD), Clegg hammer, Briaud compaction device (BCD), static plate load test (PLT), and GeoGauge, have been developed to measure soil stiffness and moduli. These devices require less time than density measurement methods and are gaining popularity (Look 2020). Another development is continuous control compaction (CCC), also known as intelligent compaction (IC), which equips compactors with sensors such as accelerometers and GPS. These sensors provide measurements related to stiffness or modulus, referred to as intelligent compaction meter values (ICMVs), overcoming the limitations of point-based measurement devices. Researchers have explored the correlation between modulus and density, aiming to eliminate the need for density measurement in the quality assurance of compacted geomaterials (Mooney and Rinehart 2007; Xu et al. 2012; Imran et al. 2018; Hu et al. 2020; Look 2020). However, a unique relationship between stiffness (unit, kN/mm), modulus (unit, kPa), and material properties such as density after compaction has not been established (Meehan et al. 2012; Lee et al. 2017; Wang et al. 2022), with further studies being needed. Previous research has also indicated that the relationship between modulus and density is not unique due to variations in moisture content (Li and Selig 1994; Tatsuoka et al. 2021).

1.3 Research aim and objectives

The aim of the research presented in this thesis was to:

> *Develop a methodology to estimate the density of a geomaterial during compaction proximally.*

The objectives supporting the project aim are as follows:

> **Objective 1:** Systematically review different density measurement systems and their geomaterials' constitutive relationship during compaction.
>
> **Objective 2:** Develop a simplified constitutive model to study the geomaterial behaviour during compaction.
>
> **Objective 3**: Develop a methodology using advanced instrumentation and analytics to estimate the density of a geomaterial during compaction proximally.

1.4 Research context and approach

The primary purpose of this work was to explore an alternative method that could better estimate geomaterial density in the field in real-time during compaction. The proposed methodology for estimating the density assumes the thickness (surface deformation) reduction of the layer during compaction as the vital indicator of the level of compaction achieved (Figure 1-3). The deformation during compaction is measured with the help of a suitable distance measurement technique, as shown in Figure 1-4. The diagram illustrates that by using two LiDAR systems, one at the front of the drum and the other at the rear of the drum, the plastic deformation during the compaction can be measured, being $D_b - D_a$. The density can then be estimated by correlating the plastic deformation with the density using advanced analytics, including physics-based and machine learning-based models.

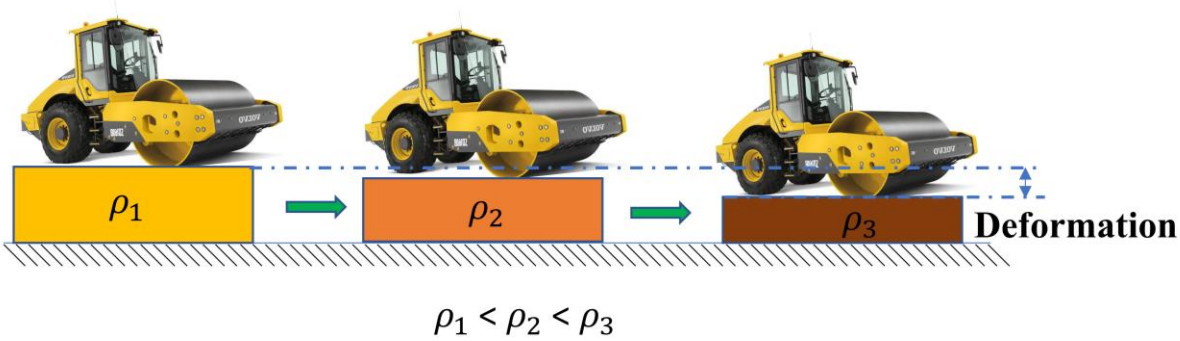

Figure 1-3. Illustration of material plastic deformation during compaction and the associated increase in density ($\boldsymbol{\rho}$).

Overall, this system is designed for estimating the density of a geomaterial layer resulting from compaction by a smooth drum compactor. The system comprises a distance sensor system that continuously measures the plastic deformation of a geomaterial during compaction. It also includes an electronic processing system that automatically generates/estimates the geomaterial layer property based on the measured plastic deformation and a pre-defined constitutive relationship/model.

The system does not require physical contact with the geomaterial, thereby avoiding the limitations and disadvantages associated with invasive methods. Additionally, the electronic processing system includes an inertial measurement unit (IMU) to measure the orientation of the compactor synchronously with the measurements of the distance sensor system. This information corrects the deformation measurement based on the measured orientations. Furthermore, the system incorporates a geolocation unit that measures/determines the

geolocation of the geomaterial synchronously with the measurements of the distance sensor system, allowing for the measurement of the plastic deformation of the entire area along with associated coordinates.

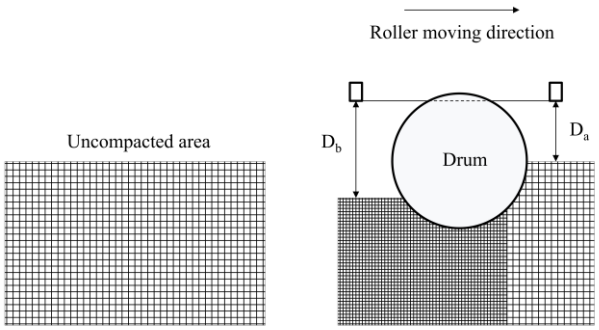

Figure 1-4. Material compaction using roller and plastic deformation measurement using LiDAR systems during compaction.

1.5 Organisation of thesis

This thesis is divided into five parts, which serve to:

- Introduce and set the context for this research (Part 1),
- Review the current density measurement systems and constitutive model of geomaterials during compaction (Part 2),
- Develop a simplified constitutive model suitable for a real-time application (Part 3),
- Develop a methodology to measure the deformation and estimate the density during compaction (Part 4),
- Summarise the research findings in the context of research and practice (Part 5).

The structure of the thesis is illustrated in Figure 1-5.

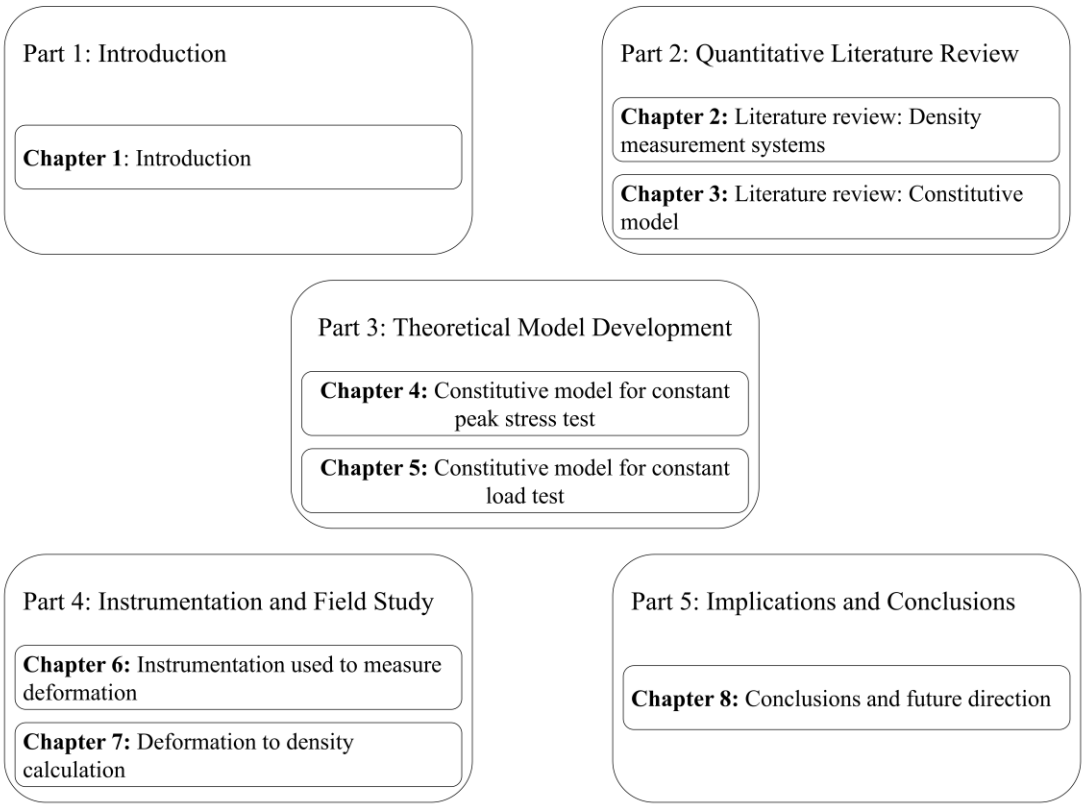

Figure 1-5. Thesis structure.

The thesis aims to advance density estimation during compaction and comprehensively overview the topic. The thesis is presented in a total of eight chapters, the contents of which are summarised below:

Part 1: Introduction

Chapter 1 - Introduction (this chapter)

Part 2 : Quantitative Literature Review

Chapter 2 - Literature Review: Density measurement systems

Chapter 2 provides a literature review of current density estimation and measurement techniques used in the field. It also discusses non-density-based quality assurance (QA) and quality control (QC) criteria.

Chapter 3 - Literature Review: Constitutive model

Chapter 3 summarizes the literature on constitutive models for capturing the complex compaction process. It includes a detailed explanation of the model referred to in this thesis.

Part 3: Theoretical Model Development

Chapter 4 - Constitutive model for constant peak stress test

Chapter 4 introduces a Theory-Guided Machine Learning (TGML) framework that combines a theoretical model with machine learning to predict compaction density under cyclic loading. It develops a constitutive model suitable for real-time applications by replicating roller loading conditions and conducting laboratory tests with constant peak stress loading.

Chapter 5 - Constitutive model for constant load test

Chapter 5 focuses on the challenges of variable stress in roller compaction and proposes a simplified constitutive model, which relates density to load level instead of stress. It uses the relationship between contact width and incremental plastic deformation to predict compaction density accurately. Experimental data from laboratory-scale steel foot compactor tests are employed in model development.

Part 4: Instrumentation and Field Study

Chapter 6 - Instrumentation used to measure deformation

Chapter 6 discusses the instrumentation required for accurate deformation measurement during compaction. It outlines the use of precise equipment and advanced data analysis techniques. The instrumentation and methodology are developed in stages, including an indoor trial and subsequent outdoor field experiment.

Chapter 7 - Deformation to density calculation

Chapter 7 expands on the instrumentation and field study, concentrating on estimating density using deformation data. Various approaches, such as 1-D compaction and a machine learning-based classification model, are explored to improve density estimation accuracy. The chapter highlights the potential of the models from Chapters 4 and 5.

Part 5: Implications and Conclusions

Chapter 8 - Conclusions and future direction

Chapter 8 presents the implications of the developed methodology for estimating density during compaction. It also identifies future research directions for advancing the methodology.

Overall, the thesis comprehensively explores density estimation during compaction, covering a literature review, theoretical model development, instrumentation, and field study.

Part 2: Quantitative Literature Review

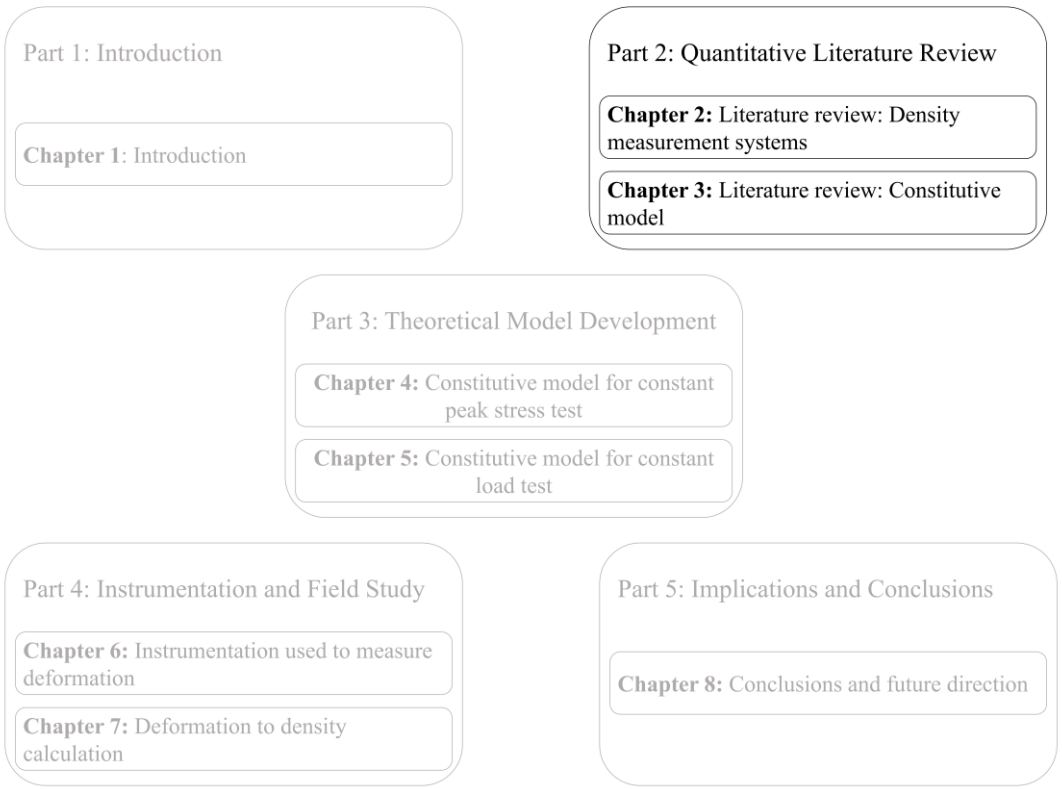

Chapter 2 Literature review: Density measurement systems

This is the first chapter of Part 2: Quantitative Literature Review. The chapter provides a literature review of current density estimation and measurement techniques used in the field. It also discusses non-density-based quality assurance (QA) and quality control (QC) criteria. Also, it highlights the advantages and disadvantages associated with their use.

2.1 QA/QC criteria for earthwork

Earthwork construction is a vital process in civil engineering involving excavation, embankment, grading and compaction of soil to construct infrastructure such as roads, railways, and buildings. The quality of the earthwork construction is critical to ensure the infrastructure's safety, stability, and durability. One essential aspect of quality assurance (QA) and quality control (QC) in earthwork construction is to check the material state and compare it with design specifications to ensure compliance. During the construction of road pavement layers, geomaterials are compacted using rollers to reach a target dry density or void ratio close to optimum moisture content (OMC) and maximum dry density (MDD) to ensure satisfactory performance over time as shown in Figure 2-1. The Density measurement has also been recommended by most road authorities in Australia and the Department of Transportation (DoT) worldwide. Different tests in QA/QC for Australia for measuring density are shown in Table 2-1.

With the advancement of mechanistic-empirical (ME) pavement design and performance-based construction specifications, methods that quantify performance-related soil parameters, such as modulus and stiffness, are gaining popularity in the field. So, as per Figure 2-2, the QA/QC can be divided into density-based and stiffness/modulus-based measurements, which can be further divided into invasive, non-invasive surface-based, and proximal measurements. Invasive or destructive approaches are methods that require sampling or disturbing the area by hammering or inserting the measurement system. Non-invasive tests are done on the surface of the compacted area but do not disturb the soil. They measure properties such as deflection, deformation, dielectric constant or resistivity for determining the geomaterial properties using correlation. Proximal measurements are implemented close to the surface but do not touch the ground to measure the geomaterial properties.

Table 2-1. QA/QC recommendation by road authorities in Australia.

Road Authority	Test	Standard
VicRoads, VIC	Nuclear Gauge	AS1289.5.8.1 (Standards Australia 2007)
Department of Planning, Transport and Infrastructure, SA	Nuclear Gauge	AS1289.5.8.1 (Standards Australia 2007)
Main Roads Western Australia, WA	Nuclear Gauge and Sand replacement	WA 324.1 (Main Roads 2012), WA 324.2 (Main Roads 2013)
Roads and Marine Services, NSW/ACT	Sand replacement and Fixed volume extractive method	T119 (Roads and Marine Services 2012a), T165 (Roads and Marine Services 2012b)
Queensland Department of Transport and Main Roads	Relative compaction, Density index	Q140A (Queensland Department of Transport and Main Roads 2017), AS1289.5.5.1 (Standards Australia 1998a), AS1289.5.6.1 (Standards Australia 1998b)
Department of State Growth, TAS	Nuclear Gauge and Sand replacement	AS1289.5.8.1 (Standards Australia 2007), AS 1289.5.3.1 (Standards Australia 2004), AS 1289.5.3.2 (Standards Australia 2002)
Department of Infrastructure, Planning, and Logistics, NT	Nuclear Gauge	NTCP 102.1 (Department of Infrastructure, Planning, and Logistics)

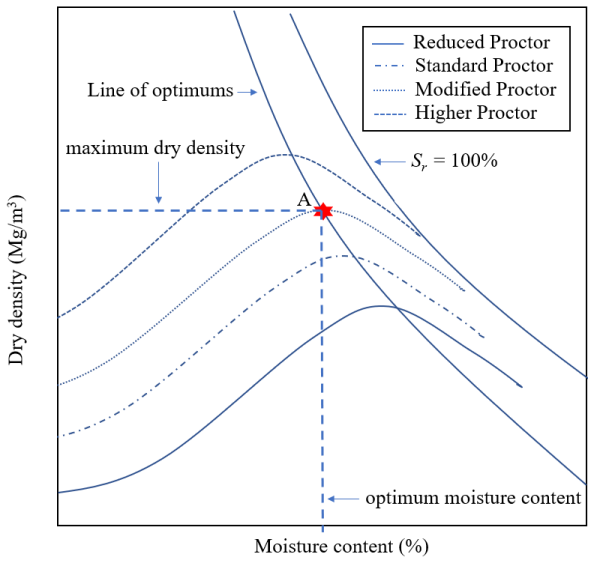

Figure 2-1. Family of Proctor curves. The applied energy decreases in the following order: higher Proctor, modified Proctor, standard Proctor, and reduced Proctor.

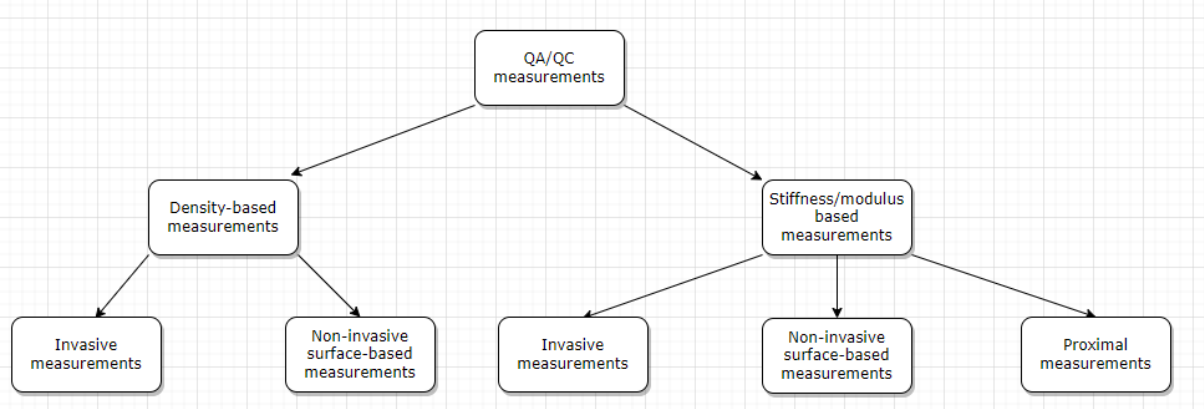

Figure 2-2. QA/QC measurements for field compaction.

2.2 Density-based QA and QC measurements

2.2.1 Invasive measurements for density

2.2.1.1 Nuclear Density Gauge (NDG)

The Nuclear Density Gauge (NDG) or Nuclear Gauge (NG) is the most widely used density test for QA and QC of earthworks. The method involves drilling a hole, driving a rod into the material, and lowering a source rod into the hole. NDG includes a Cs-137 gamma radiation source and two gamma detectors (Figure 2-3) (American Portable Nuclear Gauge Association (APNGA) 2009). The NDG measures the wet density of the soil by counting the radiation transmitted through the soil. Denser soil absorbs more radiation than loose soil, and thereby the radiation count can be converted to wet density. NDG can also be used to estimate the water content of the material. The NDG test also requires a soil sample to be taken and tested, which takes at least 24 hours to turn around (potentially longer for high plasticity soils), and a moisture content measurement to determine density ratios.

The main drawback of using the NDG is that it emits harmful rays, so prolonged exposure harms human bodies. This has led to its limited use and the need for special training and safety precautions with an additional license requirement (Latter et al. 2019).

Figure 2-3. Photo of NDG taking the density measurement.

2.2.1.2 Sand replacement or sand cone test

The sand cone test is another common field-testing method used to determine the in-place density of soils, for materials that can't be tested by NDG for example, coarse soils or mostly clay soils with a rock content higher than 20 percentage (Standards Australia 2007). It is a destructive testing method that involves excavating a small hole in the soil to be tested and then filling the hole with dry sand of a known density. The volume of the hole is determined by measuring the amount of sand used to fill the hole, and this volume is used to calculate the in-place density of the soil, as shown in Figure 2-4. The water content and dry mass of the removed soil are determined in the laboratory by drying the sample using the Microwave or Convection oven method.

Figure 2-4. Sand cone apparatus.

2.2.1.3 Rubber balloon density test

The rubber balloon density test is a simple and quick field-testing method that uses destructive testing to determine soil density in the field. Similar to the sand cone test, it involves excavating a small hole in the soil to be tested. The volume of the hole is then measured using a balloon. The balloon is inflated in the hole until it is full. Then the volume of the balloon is measured using a graduated cylinder, as shown in Figure 2-5. The soil density is calculated by dividing the mass of the soil in the hole by the volume of the hole. It is a useful tool for identifying areas of non-uniform soil density in the field and can be used to check the compaction of soil layers during earthwork projects. However, the rubber balloon density test may not be as accurate for some geomaterials as NDG and sand cones.

Figure 2-5. Rubber balloon apparatus.

2.2.1.4 Fixed Volume Extractive (FVE) method

The Fixed Volume Extractive (FVE) method involves excavating a hole in the soil and filling it with water. The volume of water used to fill the hole is then measured and used to determine the volume of the soil displaced. The dry mass of the soil is then determined in the laboratory after measuring the moisture content using a convection or microwave oven. The density is calculated by dividing the dry mass of the soil by the volume of the hole.

The drawback of the density-based methods is that they are time-consuming and a lag indicator of the density as it can take around 2-7 days for the result to be available, as the measurement of MDD in the lab to calculate the relative density or the density index requires time. Moreover the depth of excavation is limited to 300 mm (Lee et al. 2017).

2.2.2 Non-Invasive surface-based measurements for density

2.2.2.1 Moisture and Density Indicator (MDI)

The Moisture and Density Indicator (MDI) test is a non-destructive testing method used to measure a geomaterials' in-situ density and moisture content. The test uses a portable device that measures the material's dielectric constant utilising a series of radio frequency pulses. The dielectric constant is related to the density and moisture content of the material, allowing for the calculation of the in-situ density and moisture content. The MDI test is a rapid and non-destructive testing method that can be used in various soil types, including cohesive and non-cohesive soils. The device is portable and easy to use, making it ideal for field measurement (Berney and Kyzar 2012). While MDI offers potential advancements for earthworks, its adoption has been limited. The device's complex and time-consuming calibration process is ill-suited for the fast-paced nature of construction. Additionally, its inability to test high plasticity clay, a common soil type in many regions, further curtails its practicality. These constraints overshadow the MDI's potential benefits, hindering its widespread use (Lee et al. 2017).

2.2.2.2 Electrical Resistivity Test (ERT)

Electrical Resistivity Tomography (ERT) is a geophysical method used to measure the apparent electrical resistivity of soil and other subsurface materials. The technique involves injecting a low-frequency electrical current into the ground through electrodes and measuring the resulting potential difference at a second pair of electrodes. The measured potential difference is related to the apparent electrical resistivity of the soil, which is influenced by its

density and moisture content (Pandey et al. 2015; Neyamadpour 2019; Swileam et al. 2019; Yuan et al. 2020). ERT can generate a three-dimensional image of the subsurface resistivity distribution, providing information on the spatial variability of soil density and moisture content (Laloy et al. 2011). The method is particularly useful for characterising subsurface structures and variations in soil properties, such as stratigraphy and heterogeneities. ERT can effectively test a 300mm thick layer by using appropriate electrode spacing, ensuring accurate data acquisition, and utilizing inversion techniques to interpret the measured data. Additionally, ERT requires specialised equipment and expertise and can be time-consuming and expensive compared to other testing methods.

2.2.2.3 Electrical Density Gauge (EDG)

An Electrical Density Gauge (EDG) is a device used in the construction industry to measure the density of soil and asphalt. It is a handheld device that uses the principle of electrical impedance to determine the density of the material under test. The device consists of two electrodes inserted into the soil or asphalt (Anderson et al. 2001). An electrical current is then passed between the electrodes, and the impedance of the material measured. The impedance is directly related to the density of the material, and so the EDG can display the density measurement on a digital screen. EDG offer potential in soil testing, but their limited adoption stems from a few challenges. Firstly, their complex and time-consuming calibration procedures can be cumbersome, especially in fast-paced project settings. Additionally, they require Nuclear Density Meters (NDM) for calibration, adding a layer of dependency and the need for dual expertise. Furthermore, EDGs struggle with certain soil types, notably their incapacity to test high plasticity clays accurately (Lee et al. 2017).

2.2.2.4 Ground Penetrating Radar (GPR)

Ground Penetrating Radar (GPR) is a non-invasive geophysical technique that uses electromagnetic waves to investigate subsurface structures and materials. While GPR is primarily used to identify and locate buried objects and structures, it can also be used to measure the density of soil and other subsurface materials. When using GPR to measure soil density, a high-frequency antenna is typically used to send short pulses of electromagnetic energy into the soil. As these pulses travel through the soil, they encounter different materials with varying densities. The waves the antenna receives are then analysed to determine the soil density (Wang et al. 2018). The soil density is determined by measuring the time it takes for the electromagnetic wave to travel through the soil and be reflected to the antenna. The longer

the travel time, the denser the soil. The reflected waves are also affected by the electrical properties of the soil, such as its moisture content and salinity, which can further aid in determining soil density. GPR can measure soil density over a large area quickly and non-invasively, making it a valuable tool in geotechnical investigations and environmental assessments. It can also identify soil areas with varying densities, which can help plan construction projects and identify potential hazards, such as sinkholes. However, it should be noted that GPR is not a precise tool for measuring soil density. It should be used with other methods, such as the Electrical Density Gauge (EDG), for more accurate measurements.

Non-invasive surface-based measurements, such as MDI, ERT, EDG, and GPR, have also emerged as practical and effective methods for measuring soil density in situ without disturbing the soil. These methods offer several advantages over conventional methods, including their speed, accuracy, and cost-effectiveness. They also provide real-time measurements to aid decision-making and quality control during construction projects. The MDI test is particularly useful for measuring the density and moisture content of soils and compacted materials, making it an ideal tool for assessing soil quality during construction projects. Conversely, ERT and GPR offer three-dimensional imaging capabilities that can provide valuable information on the spatial distribution of soil properties, including density and moisture content. The EDG is a handheld device that is quick and easy to use, making it a popular choice for construction workers and engineers. Overall, non-invasive surface-based measurements offer a practical and efficient solution for measuring soil density, allowing for more accurate and informed decision-making during construction projects. However, it is important to note that these methods have limitations as they have a relationship with both water content and density and are affected more heavily by water content than density (Plati and Loizos 2013).

The conventional approach to measuring soil density involves collecting physical samples, measuring their mass and volume, and analysing them, which can be time-consuming, especially when multiple samples are required. This can be problematic for contractors eager to compact another layer of soil promptly to avoid additional costs for equipment and labour. As a result, alternative QA/QC criteria have been developed to assess earthwork quality.

2.3 Stiffness/modulus-based QA/QC measurements

2.3.1 Invasive methods for measuring stiffness/modulus

2.3.1.1 Dynamic Cone Penetration Test (DCPT)

The dynamic cone penetration test (DCPT) is a simple and cost-effective method used to evaluate the strength and stiffness of soil layers in the field (Abu-Farsakh et al. 2005). It involves driving a metal cone with a standardised mass and dimensions into the soil using a hammer and measuring the penetration depth. During the test, the cone is dropped from a standardised height and allowed to penetrate the soil. The number of blows required to penetrate a certain depth is then recorded. The number of blows is correlated with the stiffness or density of the geomaterial; however, there is significant scatter, limiting its use.

2.3.1.2 Clegg Hammer

The Clegg Hammer device works by dropping a standardised weight (typically 2.25 kg) onto the soil surface and measuring the rebound. The degree of rebound is correlated with the stiffness and density of the soil, with denser and stiffer soils producing a lower rebound. The device is portable and easy to use, making it ideal for field measurements (Jaffar et al. 2022).

2.3.1.3 Static plate load test

The static plate load test is a field test used to evaluate the strength and stiffness of soils. The test involves loading a circular steel plate with a standardised diameter and thickness onto the surface of the soil and measuring the deformation of the soil surface in response to the applied load. During the test, a load is applied incrementally to the plate, and the corresponding vertical deformation of the soil surface is measured using a dial gauge or displacement transducer. The soil's density and stiffness can be estimated from the static plate load test results by using empirical correlations between the plate load test load-deformation data and soil density and stiffness (Tompai 2008).

2.3.2 Non-invasive surface-based measurements for stiffness/modulus

2.3.2.1 Falling Weight Deflectometer (FWD)

The Falling Weight Deflectometer (FWD) is a device used to measure a geomaterials' stiffness and load-bearing capacity. The device works by dropping a weight onto the pavement or soil surface and measuring the resulting deflection with sensors. The deflection measurements

obtained from the FWD can be used to estimate the stiffness and load-bearing capacity related to their density and other properties (Livneh and Goldberg 2001). The FWD is particularly useful for evaluating the in-situ density and stiffness of soils beneath pavements and other structures where access is limited or performing more invasive testing methods is not feasible.

2.3.2.2 Portable Seismic Pavement Analyser (PSPA)

A Portable Seismic Pavement Analyser (PSPA) is a device used to evaluate pavement's structural integrity and strength on roads. The PSPA uses seismic technology to measure the velocity of surface waves that propagate through the pavement. By measuring the velocity of these waves, the PSPA can determine the stiffness and thickness of the pavement layers, as well as identify any voids or delamination within the pavement structure. The PSPA consists of a small, portable unit mounted on a cart and rolled over the pavement surface, as shown in Figure 2-6. The unit contains a seismic source that generates a slight, controlled vibration and an array of sensors that measure the resulting surface waves. The PSPA's software then processes the data collected by the sensors to calculate the pavement's structural properties.

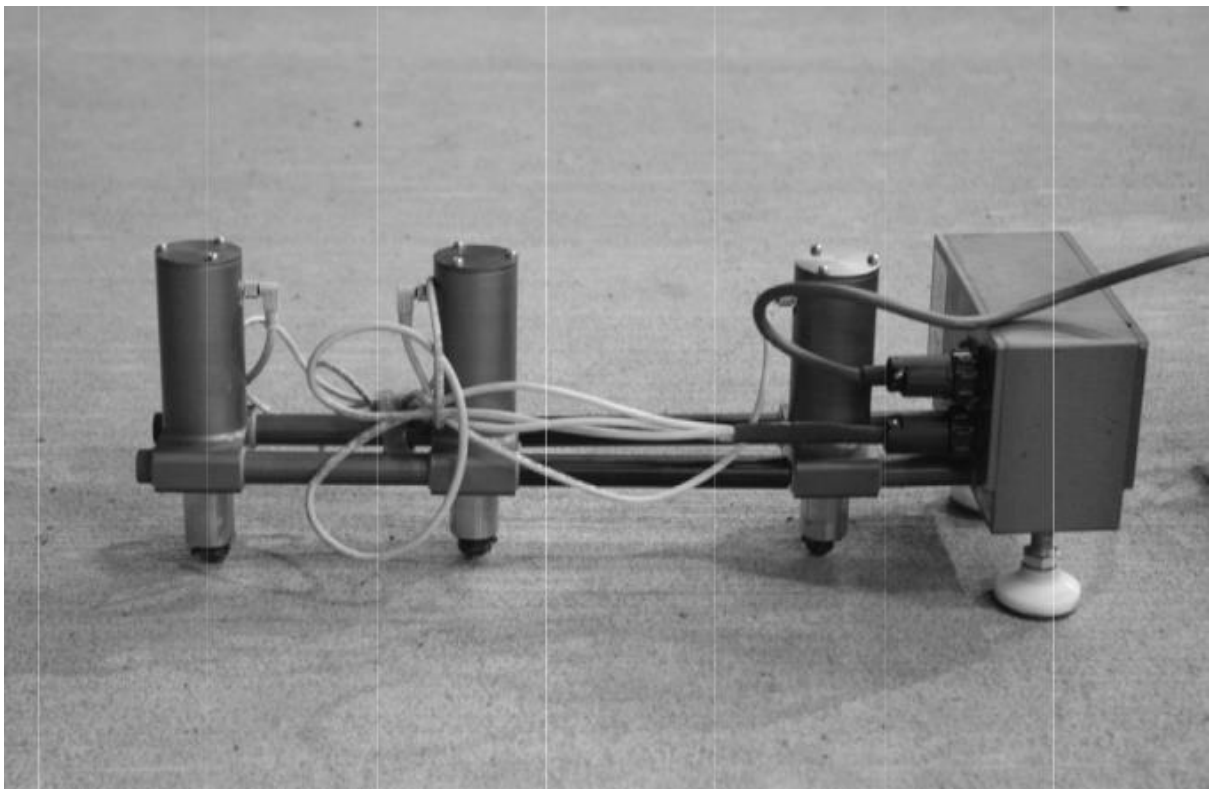

Figure 2-6. Schematic of Portable Seismic Pavement Analyzer (PSPA) (Li and Garg 2015).

2.3.2.3 GeoGauge

The GeoGauge is a device used to measure the in-situ stiffness of soils. It is a non-destructive testing method that provides rapid and accurate results. The GeoGauge works by measuring the response of the soil to a small dynamic load applied by a spring-loaded foot attached to the bottom of the device. The foot is pressed against the surface of the soil, and the device measures the resulting deformation of the soil surface. The GeoGauge can therefore measure the deformation at a specified depth within the soil, providing a profile of the soil stiffness with depth. The GeoGauge device is portable and can be used in various soil types, including cohesive and non-cohesive soils.

As with all testing methods, the results should be interpreted in the context of the specific site conditions and in conjunction with other testing methods to understand the soil properties comprehensively. It should also be noted that correlations to density are typically site-specific and may not apply to other sites (Caicedo 2019). They are also very complex requiring extensive operator training (Weber 2018).

2.3.3 Proximal measurements for measuring stiffness/modulus

2.3.3.1 Intelligent Compaction

Intelligent Compaction (IC), developed in the 1970s, utilises roller drums fitted with accelerometers to measure soil and asphalt compaction through acceleration patterns (White et al. 2007; Hu et al. 2017, 2020; Foroutan and Ghazanfari 2018; Imran et al. 2018; Liu et al. 2019; An et al. 2020). It has already gained popularity in the United States. It is being accepted as an alternative QA/QC for density measurement. The IC roller is integrated with sensors such as temperature, accelerometer, Global Positioning System (GPS), and a display monitor. The continuous recording of the GPS and accelerometer data provides a user indirectly with real-time information about the compaction degree. The data from accelerometers, combined with other equipment parameters such as rolling speed, frequency, and amplitude of the compaction drum, are analysed. Through this analysis, and by leveraging correlations established from initial calibration efforts, the degree of compaction is inferred. The recorded drum response is used to calculate different Intelligent Compaction Measurement Values (ICMVs), which correlate with density. The correlation between ICMVs and density is poor; however, the correlation between ICMVs and modulus is good for some range of moisture content of the material (Zargar and Lee 2019; Hu et al. 2020).

The stiffness/modulus-based QA is shown to be quicker than density measurement and thus is preferred by the practitioners over the density-based QA. The modulus, which is considered to have a unique and direct correlation with density, is considered to replace the density measurement. However, researchers have also found that the correlation between density and modulus is not unique, depending also on the water content of the sample (Tophel et al. 2023).

2.4 Summary

Chapter 2 of Part 2: Quantitative Literature Review focuses on density estimation and measurement techniques in earthwork construction. It emphasizes the importance of quality assurance (QA) and quality control (QC) criteria for ensuring the quality and safety of infrastructure projects. Earthwork construction involves activities like excavation, grading, and soil compaction, which are crucial for developing infrastructure such as roads and buildings. QA and QC procedures are essential to evaluate and compare the material state with design specifications.

Density measurement serves as a critical component of QA and QC for road pavement layers. Various road authorities, including VicRoads in Victoria and the Department of Transportation (DoT) globally, recommend density-based tests such as the Nuclear Gauge (NDG) and sand replacement methods. The NDG is widely employed and involves drilling a hole, inserting a rod into the material, and utilizing gamma radiation to measure the wet density of the soil which is harmful to human health. Conversely, the sand replacement method is a destructive test that entails excavating a small hole, filling it with dry sand of known density, and measuring the volume of the hole to calculate the in-place density of the soil.

In addition to invasive density-based measurements, non-invasive surface-based techniques are gaining popularity in the field. These methods encompass the Moisture and Density Indicator (MDI), Electrical Resistivity Tomography (ERT), Electrical Density Gauge (EDG), and Ground Penetrating Radar (GPR). However, these methods have limitations, as they are more influenced by water content than density.

The chapter also discusses stiffness/modulus-based QA and QC measurements. Invasive methods like the Dynamic Cone Penetration Test (DCPT), Clegg Hammer, and static plate load and non-invasive techniques such as the Falling Weight Deflectometer (FWD) and Portable Seismic Pavement Analyzer (PSPA) tests are used to assess the strength and stiffness of soil layers. These, however, do not correlate very well with the density of the material.

Chapter 3 Literature review: Constitutive model

This is the second chapter of Part 2: Quantitative Literature Review. This chapter explores the need and importance of a proper constitutive model in the context of proximal density estimation and presents the current availability and past relevant works. It considers both physics-based theoretical models and machine learning-based models as potential solutions to address the challenges of modelling unsaturated material behaviour and capturing the complex nonlinear elastic-plastic behaviour of field compaction.

Quality assurance requires achieving specified dry density (ρ_d) or void ratio (e) for the geomaterial layers, along with other properties like stiffness (K) and modulus (E).

The compaction of geomaterial involves increasing ρ_d by reducing e through minimising air voids through the application of loads using different types of rollers, as shown in Table 3-1.

Table 3-1. Types of roller for various materials (VicRoads 1998).

Material type	Roller type
Heavy clay	Static tamping foot, Pneumatic multi-tyred, Vibrating sheep foot
Sandy clay	Static tamping foot, Pneumatic multi-tyred, Vibrating sheep foot
Crushed rock	Smoothed steel drum, Pneumatic multi-tyred, Vibrating smooth drum
Sand and rockfill	Grid Roller, Vibrating smooth drum

These rollers can be divided into two major categories, static and vibratory. The static apply load with their weight only while vibratory apply dynamic load in addition to static load. The constitutive model for compaction can be divided primarily into two major categories: (a) physics-based and machine learning-based models.

3.1 Physics-based theoretical model

The compaction process involves cyclic loading and unloading caused by the movement of a roller. Field compaction of soils using rollers is challenging to analyse due to large deformations and complex nonlinear elastic-plastic behaviour (Xu and Chang 2020). Analytical and finite element formulations have been used to model the behaviour of unsaturated materials under complex cyclic loading (Pestana et al. 2002; Wichtmann 2005; Modoni et al. 2011; Pasten et al. 2014; Chong and Santamarina 2016; Park and Santamarina 2019; Chen et al. 2021). However, these models often require sophisticated and time-

consuming tests to determine the model parameters. The interaction among soil, water, and air phases makes modelling unsaturated material behaviour even more challenging, limiting the practical use of complex numerical models in real-time field applications.

Constitutive models for unsaturated soils can be classified based on the work input relationship. Houlsby (1997) introduced thermodynamic work input in the volumetric deformation of unsaturated soils, considering variables such as void ratio (e), net stress (p_{net}), suction (s), moisture ratio (e_w), and degree of saturation (S_r), which is calculated as the ratio of e_w to e. Alonso, Pinyol, and Gens (2013) and Wheeler and Sivakumar (1995) used specific volume (v), p_{net}, and s as variables in their models, without directly coupling the specific moisture volume (v_w) or S_r. Other approaches employed effective stress ($p + \chi\, s$) where χ is a function of suction (s) (Loret and Khalili 2002) or used Bishop's effective stress ($p\ +\ S_r\, s$), considering S_r as a separate variable (Wheeler et al. 2003). Recently, based on the MPK framework, researchers (Kodikara 2012; Kodikara et al. 2020) proposed that net stress and moisture content or degree of saturation can be used to model volumetric behaviour, without directly coupling suction (s) when the material is compacted on the dry side of the line of optimum (LOO). Moreover, Kodikara et al. (2020) reported that Bishop's effective stress is applicable for materials compacted on the wet side of LOO which requires the knowledge of suction. However, measuring suction, especially in field conditions, is challenging. Therefore, this thesis proposes a constitutive model based on net stress, extending the model proposed by Sawicki and Swidzinski (1995), which also utilized net stress (total stress) and water content as input parameters. Since field compaction is typically performed at a constant moisture content of $\pm$2% of the optimum moisture content (OMC), for simplicity, this study utilizes constant moisture content as one of the input variables for the model development. In addition, this model, known as the theoretical model (TM), offers simplicity and requires only three parameters to capture cyclic behaviour. The TM enables real-time use and data processing, making it a practical choice for compaction analysis.

3.1.1 Cyclic compaction model by Sawicki and Swidzinski (1995)

The work by Sawicki and Swidzinski (1995) aimed to investigate the behaviour of particulate materials, including soils, grains, and powders, under cyclic loading in uniaxial deformation. The mechanical behaviour of these materials was analysed under uniaxial cyclic deformation in oedometric conditions (Figure 3-1). A constitutive equation describing cyclic compaction was proposed based on the concept of a standard compaction curve.

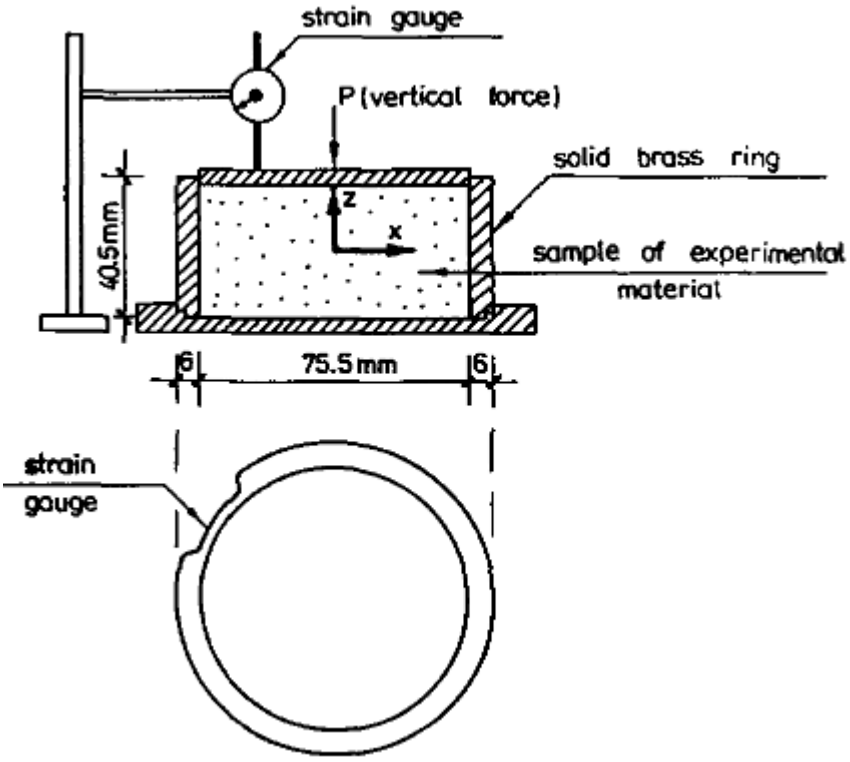

Figure 3-1. Figure of the oedometer setup used in the study by Sawicki and Swidzinski 1995.

Each sample underwent ten loading and unloading cycles, with controlled vertical stress and measurement of lateral stress and vertical strain. The results revealed similarities among different sands, leading to several general conclusions: compaction increases with the number of loading cycles but the rate of compaction decreases with the cycle number; compaction is influenced by the maximum vertical stress with higher stress resulting in greater compaction; residual lateral stresses generally increase with the number of cycles but the rate of increase decreases; the value of residual lateral stress depends on the maximum vertical stress with the initial cycle having a predominant influence. The equation developed for plastic strain (ϵ^p) accumulation with the number of cycles (N) when the sample was subjected to static vertical stress (σ_z) is

$$\epsilon^p = C_1 \ln(1 + C_2(1 - K_0)^m N \sigma_z^m), \quad (1)$$

where σ_x is the lateral normal stress and the stress invariant (stress tensor responsible for compaction) is considered to be $(\sigma_z - \sigma_x)^m$, which becomes $(1 - K_0)^m \sigma_z^m$ with ($K_0 =$

$\frac{\sigma_x}{\sigma_z}$) denoting the coefficient of lateral pressure, and C_1, C_2 and m are the material parameters. Modification of the model for 1D compaction of soil and variation of the parameters with material properties is presented in Chapter 4 for a constant stress cyclic test carried out in the laboratory.

Similar to other constitutive models, this model unfortunately requires input parameters such as stress, which varies during compaction. When using a roller, geomaterial properties (stiffness, ρ_d, modulus) and geomaterial-compactor interactions (contact width, contact stress) vary even when the applied load remains constant (Kargl 1995; Hager et al. 2021). For example, research has shown that the contact width reduces with an increase in ρ_d, leading to increased contact stress as compaction progresses (Ghorbani et al. 2021). Calculating stresses using Hertz's theory requires knowledge of either Young's modulus or the contact width, which changes during compaction. These parameters are difficult to measure or estimate during the compaction process. Detailed numerical modelling approaches often assume constant parameters during simulation, limiting their capability (Kenneally et al. 2015). For instance, some models assume a constant modulus for the geomaterial during compaction, while it has been demonstrated that the modulus depends on ρ_d and increases as ρ_d increases (Tatsuoka et al. 2021). Therefore, it is important to have a constitutive model which can accommodate the change of material properties during compaction.

Recent developments in data science, such as ML and especially deep learning (DL) models, including artificial neural network (ANN), support vector machines (SVMs), and Gaussian process regression (GPR), have allowed the data available from measurements be used for modelling in various geotechnical applications (Liu et al. 2015; Pooya Nejad and Jaksa 2017; Makasis et al. 2018; He et al. 2020; Kang et al. 2021; Zhang and Jin 2021; Zhang et al. 2021). For instance, data-driven models for capturing the complex behaviour of soil compaction in estimating the material properties for quality assurance (QA) and quality control (QC) purposes have recently been considered and integrated with IC (Imran et al. 2018). In particular, the response of the drum reaction (i.e. the acceleration history) of the roller's vibratory drum is used to estimate the in-situ states of the compacted material (e.g., modulus and roller-related stiffness) (Commuri et al. 2011; Cao et al. 2021). This study also explored the use of machine learning (ML) models to capture complex behaviour during compaction. This is particularly useful when the data collected is very large and requires a model which

can handle large datasets. For this thesis, a regression-based ML model (ANN) and classification-based ML model (stochastic gradient descent (SGD) are explored.

3.2 Machine learning-based models

3.2.1 Artificial Neural Networks (ANNs)

ANNs are an ML tool for modelling and solving nonlinear relationships between input and output data (Braspenning et al. 1995). They are considered data-driven models with an unrestricted number of model parameters, and so are very useful when there is a large amount of data. There are numerous applications of ANNs, and some examples include image classification (Park et al. 2004), regression (Rezaie-Balf and Kisi 2018), forecasting (Kolarik and Rudorfer 1994) and real-time optimisation (Wang and Salehi 2015).

A neural network structure consists of three distinct layers: input, hidden, and output. This multi-layer system is also known as a multi-layer perceptron (MLP), and a typical structure is shown in Figure 3-2. During ANN model training, the input layer, which can have one or many nodes, passes the information to the nodes of the hidden layers. The information from a node is multiplied by a weight matrix, denoted as W, and added to a value called a bias matrix, denoted as b. The output is then passed to an activation function F. This process continues between each node until the information reaches the output layer. Function F is the activation function, which in this study, incorporates a rectified linear unit (ReLU) for the hidden layers, and a linear function at the output layer (Géron 2017).

The predicted output (Y_{ML}) is compared to the actual output (Y) by computing the loss function (L) according to standard metrics such as mean absolute error (MAE) or root mean squared error (RMSE) and the regularization loss function L_{reg} as

$$\text{Loss function (MAE)} = L(Y, Y_{ML}) = \frac{1}{len(Y)} \sum_{i=1}^{len(Y)} |Y - Y_{ML}|, \quad (2)$$

$$L_{reg} = \lambda_{reg} \parallel W \parallel, \quad (3)$$

$$\mathrm{RMSE}(Y, Y_{ML}) = \sqrt{\frac{1}{len(Y)} \sum_{i=1}^{len(Y)} (Y - Y_{ML})^2}, \tag{4}$$

where, $len(Y)$ represents the length of matrix Y and λ_{reg} represents the regularization hyperparameter (Géron 2017). The total loss $L + L_{reg}$ is minimised using the back-propagation algorithm by adjusting the values of W and b. Once training of the model is achieved, the trained model is used to predict new sets of data.

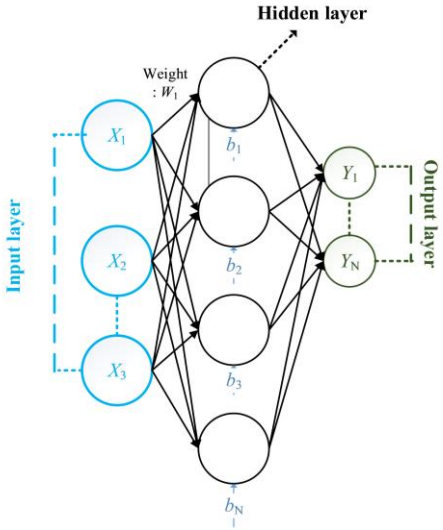

Figure 3-2. Architecture of a simple ANN with three input nodes, one hidden layer of four nodes and two output nodes (the bias nodes are shown but are usually implicit in the structure).

3.2.2 Stochastic Gradient Descent (SGD) classification model

The Stochastic Gradient Descent (SGD) classification model was explored as part of the study to capture the complex behaviour during compaction using machine learning (ML) models. The SGD classification model is an optimization algorithm commonly used in machine learning for training classification models, especially when dealing with large datasets. The SGD classification model works by iteratively updating the model's parameters based on the gradients of the loss function for those parameters. Unlike traditional Gradient Descent, which considers the entire dataset in each iteration, SGD randomly selects a single training sample

or a small batch of samples to compute the gradient. During training, the SGD classification model adjusts its parameters to minimize a predefined loss function, such as the cross-entropy loss for binary or multiclass classification. The goal was to find the optimal set of parameters that best fit the training data and generalize well to unseen data. After training, the SGD classification model could predict new data by applying the learned parameters to the input features and a decision rule (e.g., thresholding or SoftMax) to determine the predicted class.

However, purely data-driven ML models like SGD have some disadvantages. They do not adhere to underlying physics, as they are trained on limited data and may produce results that deviate from known mechanistic behaviour or scientific principles (Karpatne et al. 2017a). They are prone to overfitting, learning the training data rather than the underlying patterns and performing poorly on unseen test data (Roelofs et al. 2019). ML models also have limited interpolation and extrapolation abilities, leading to errors in sparse datasets and challenges in making correct predictions beyond the range of training data (Rai and Sahu 2020).

3.3 Comparison of theoretical model (TM) and machine learning (ML) model

Developing a TM for complex processes like field compaction requires understanding the intricate interactions between the material and the roller compactor. However, the availability of parameters and incomplete technical embodiment can limit the development of such models. Additionally, calibrating the parameters of a TM can be challenging due to the combinatorial nature of the search space, which may lead to overly complex models (Karpatne et al. 2017b).

In contrast to TM algorithms, ML algorithms have been criticized for being "black boxes" due to their hidden complexity and the potential for producing outputs that lack physical meaning. This limitation restricts their use in certain domains (Kumar et al. 2017). It is therefore beneficial to combine TM and ML algorithms to overcome these challenges, leveraging their respective strengths and mitigating their drawbacks (Raissi et al. 2017a; Raissi and Karniadakis 2018; Jia et al. 2018; Rai and Sahu 2020). This approach, known as Theory-Guided Machine Learning (TGML), involves incorporating theoretical and scientific knowledge from the TM into the construction and training of ML and Deep Learning (DL) models (Rai and Sahu 2020).

The TGML framework can be applied to any domain using theoretical and physics-based knowledge and available data. TGML techniques have been successfully applied in solving

differential equations (Raissi and Karniadakis 2018) and addressing cyber-physical systems (Rai and Sahu 2020). However, in the Civil or Geotechnical engineering domains, particularly in areas like liquefaction assessment and groundwater flow modelling, TGML has been limited (Zhang et al. 2020; Depina et al. 2021). Chapter 4 of the study presents the TGML framework, which combines the TM and ML in three ways to predict material density during compaction.

By integrating TM and ML, it is possible to reduce the complexity of ML models while incorporating valuable theoretical knowledge. This hybrid approach has the potential to enhance the accuracy and reliability of predictions, addressing the challenges faced by purely data-driven ML models.

3.4 Summary

The success of civil engineering projects depends on evaluating ground conditions, particularly geomaterial layers that support structures. Inadequate compaction can lead to poor performance and premature failure, impacting the infrastructure's lifespan. Ensuring quality involves achieving specific properties like density and stiffness. The compaction process uses static or vibratory rollers. Accurate modelling requires a precise constitutive model, but existing models require complex tests. This chapter explored the need for suitable constitutive models, considering physics-based and machine-learning approaches to address challenges in modelling unsaturated material behaviour and nonlinear compaction. This chapter also discussed the development of a model which can be used for a real-time application.

Part 3: Theoretical Model Development

Publications:

- **Chapter 4: Tophel A**, Walker JP, Dutta TT, Kodikara J (2022) Theory-guided machine learning to predict density evolution of sand dynamically compacted under Ko condition. *Acta Geotechnica*. https://doi.org/10.1007/s11440-021-01431-2
- **Chapter 5: Tophel A**, Walker JP, Dutta TT, Bodin D, Kodikara J (2023) Model development to predict dynamic interactions of roller and geomaterial using simulated roller compaction. *Transportation Geotechnics* 39:100946. https://doi.org/10.1016/j.trgeo.2023.100946

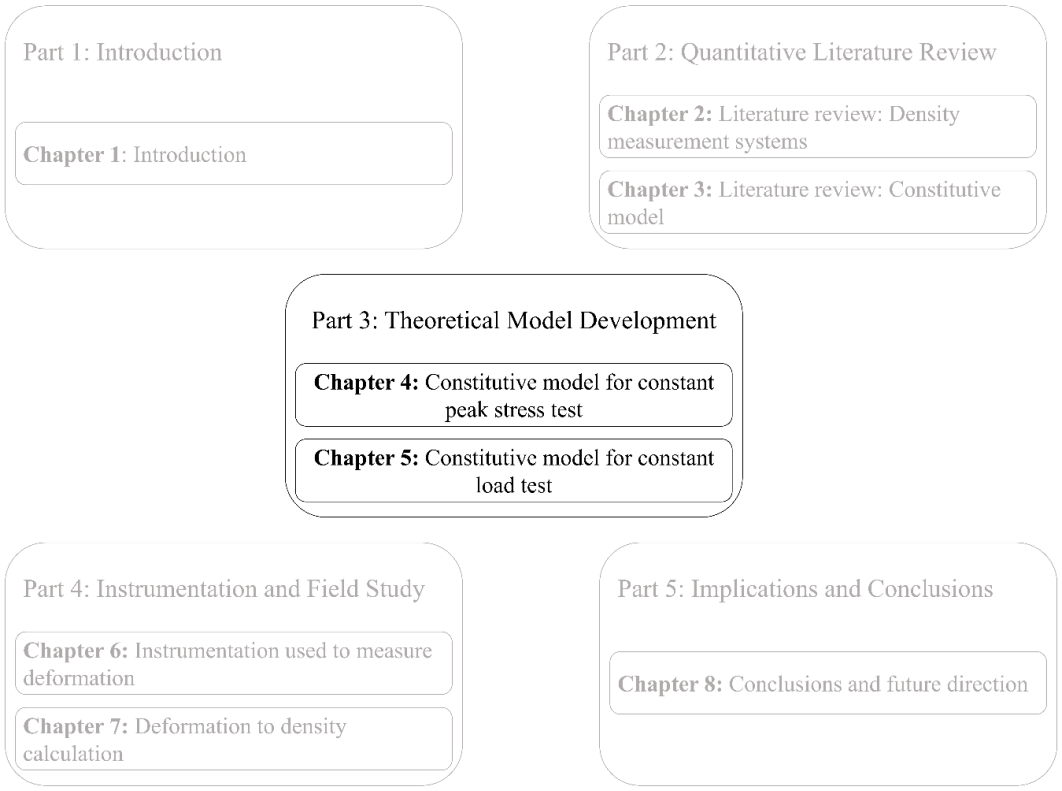

Chapter 4 Constitutive model for a constant peak stress test

This is the first chapter of Part 3: Theoretical Model Development. The chapter presents a Theory-Guided Machine Learning (TGML) framework that combines a theoretical model with machine learning to predict compaction density under cyclic loading. Part 1 of the thesis emphasized the importance of a simplified constitutive relationship in studying material behaviour under dynamic load. However, there has been limited investigation into the behaviour of geomaterials subjected to vibratory load and frequency similar to field compaction. This study replicated roller loading conditions and conducted a series of constant peak stress 1D cyclic loading experiments on uniformly graded sand to study its behaviour and develop a constitutive model with relatively few parameters, making it suitable for real-time applications. While uniformly graded sand is not a common choice for field compaction, it was selected in our laboratory testing for its simplicity, primarily to eliminate the effects of variables such as gradation and fines content. The chapter also introduces a novel TGML framework that combines the advantages of physics and machine learning. Later in Chapter 7, the developed TGML framework is used to denoise the deformation data measured from the sensors. The simplification of models to facilitate machine learning (ML) applications introduces inherent philosophical challenges. While ML promises to derive patterns from data autonomously, practical implementations often lean towards guided methodologies, akin to calibrating theoretical models. This balance between data-driven insights and imposed constraints is pivotal. It suggests that even as ML tools offer profound insights, their results remain influenced by the boundaries set. Such considerations are vital when interpreting the implications and breadth of machine learning outcomes within this domain.

This chapter is based on the published research paper:

- **Tophel A**, Walker JP, Dutta TT, Kodikara J (2022) Theory-guided machine learning to predict density evolution of sand dynamically compacted under Ko condition. *Acta Geotechnica*. https://doi.org/10.1007/s11440-021-01431-2.

The chapter concludes with a section including the errata and addenda followed by a section summarizing the findings of this part of the study.

4.1 Theory-Guided Machine Learning to Predict Density Evolution of Sand Dynamically Compacted Under K_o Condition

Acta Geotechnica
https://doi.org/10.1007/s11440-021-01431-2

RESEARCH PAPER

Theory-guided machine learning to predict density evolution of sand dynamically compacted under K_o condition

Amir Tophel[1] · Jeffrey P. Walker[2] · Troyee Tanu Dutta[1] · Jayantha Kodikara[1]

Received: 1 August 2021 / Accepted: 28 November 2021
© The Author(s), under exclusive licence to Springer-Verlag GmbH Germany, part of Springer Nature 2022

Abstract
This paper introduces a theory-guided machine learning (TGML) framework, which combines a theoretical model (TM) and a machine learning (ML) algorithm to predict compaction density under cyclic loading. Several 1-D tests were conducted on uniformly graded fine sand compacted at varying moisture contents (w), stress levels (σ_z) and loading frequencies (f), simulating the field compaction of materials using a vibratory roller. The laboratory compaction data were first analysed using a revised TM and an artificial neural network (ANN), and their performance was measured using mean absolute error (MAE). Next, the data were analysed using the TGML framework, which involves three different techniques. TGML1 increased the ML's ability to extrapolate (MAE improved from 2.2×10^{-3} to 1.2×10^{-3}); TGML2 ensured ML and TM complemented each other to model observations better (MAE improved from 2.3×10^{-3} to 7.9×10^{-4}); and TGML3 assisted in regularising the ML with an additional loss function which ensured the model followed the mechanistic understandings of the underlying physics (MAE improved from 9.2×10^{-3} to 2.7×10^{-3}). Considering TGML3 during modelling is essential when dealing with noisy field datasets, and this is the highlight of this paper. TGML frameworks showed less error and lower model uncertainty, estimated using the novel Monte Carlo dropout technique. Furthermore, the developed TGML framework was used to demonstrate a termination criterion, i.e. the number of cycles of roller movement required to achieve the desired degree of compaction. Finally, an approach is proposed by which a simplified TM and ML model can estimate field compaction behaviour during roller movement.

Keywords Compaction · Density · Monte Carlo dropout · Termination criteria · Theory-guided machine learning · Uncertainty

List of symbols

F	Activation function
Y	Actual output or observation
ANN	Artificial neural network
e^p	Axial or volumetric plastic strain
b_i	Bias matrix
C_C	Coefficient of curvature
K_0	Coefficient of lateral pressure
C_u	Coefficient of uniformity
DL	Deep learning
FS	Fine sand
f	Frequency of vibration
$\mathcal{N}$	Gaussian noise
z_i	Hidden layer output
λ_{reg}	Hyperparameter for L2 regularization
N_{initial}	Initial guess of no. of cycles in termination criteria
e_0	Initial void ratio
X	Input matrix
GPR	Gaussian process regression
IC	Intelligent compaction
ML	Machine learning
Y_{ML}	Machine learning prediction
MDD	Maximum dry density

✉ Jayantha Kodikara
jayantha.kodikara@monash.edu

Amir Tophel
amir.tophel@monash.edu

Jeffrey P. Walker
jeff.walker@monash.edu

Troyee Tanu Dutta
troyee.dutta@monash.edu

[1] ARC Industrial Transformation Research Hub (ITRH) – SPARC Hub, Department of Civil Engineering, Monash University, Clayton Campus, Clayton, VIC 3800, Australia

[2] Department of Civil Engineering, Monash University, Clayton Campus, Clayton, VIC 3800, Australia

Published online: 04 February 2022

σ_z	Maximum vertical stress
MAE	Mean absolute error
μ	Mean of the noise
D_{50}	Median diameter
C_1, C_2 and m	Model parameters
w	Moisture content
MLP	Multi-layer perceptron
Y_{Noisy}	Noisy observations
$\frac{e_0-e_{30}}{e_0}$	Normalized relative change in void ratio
NDG	Nuclear density gauge
N	Number of cycles
η	Optimization rate
f_{opt}	Optimum compaction frequency
S_{ropt}	Optimum degree of saturation
OMC	Optimum moisture content
U	Output after applying activation function
Y	Output matrix
$\hat{Y}$	Prediction of ANN
e_{proctor}	Proctor void ratio
QA	Quality assurance
QC	Quality control
σ_x	Radial stress
RF	Random forest
ReLU	Rectified linear unit
RNN	Recurrent neural network
$e_0 - e_{30}$	Relative change in void ratio
G_S	Specific gravity
σ_s	Static stress
SGD	Stochastic gradient descent
SVM	Support vector machine
SVR	Support vector regression
N_{target}	Target number of passes
e_{target}	Target void ratio
TM	Theoretical model
Y_{TM}	Theoretical model prediction
TGML	Theory-guided machine learning
T_V	Duration for vibratory load
s^2	Variance of the noise
σ_v	Vibratory stress
e	Void ratio
e_1	Void ratio after the first cycle
e_N	Void ratio at Nth cycle
W_i	Weight matrix

1 Introduction

Compaction of materials (soils and unbound granular materials) in the field is required to ensure satisfactory performance under external factors such as repeated traffic loads and environmental effects. Density is an indicator of the degree of compaction, and is commonly characterised with respect to the maximum dry density (MDD) determined at the optimum moisture content (OMC) using Proctor compaction in the laboratory. Achievement of the designated dry density (DD) and OMC in the field is crucial, as under-compacted or over-compacted materials lead to premature failure and/or undesirable permanent deformation or rutting. Various laboratory studies have shown that in general, greater material density results in better resistance to rutting, thus enhancing the service life of pavements [30, 31, 2]. Current density measurement techniques (nuclear density gauge (NDG), sand cone tests and gravimetric tests based on field sampling) can only measure density levels after compaction is complete; moreover, these measurements are confined to a discrete location and are time-consuming. It has been reported that compliance with field specifications following these density measurements either unacceptably delays construction or becomes practically difficult to accomplish [29, 34]. Conversely, there is a significant push to adopt continuous compaction control (CCC) as in intelligent compaction (IC), but it is limited by the inability to estimate geomaterial density proximally. Hence, a genuine need exists to develop methodologies to predict density during compaction using appropriate numerical modelling.

The compaction of material in the field is an example of cyclic loading and unloading because of the movement of road compactors. Modelling the response of unsaturated materials to complex cyclic loading at laboratory scale has been attempted by various researchers using sophisticated analytical and finite element formulations [9, 37, 41–43, 69]. These models may capture complex behaviour well, but require sophisticated and time-consuming tests to determine the model parameters. Generally, the behaviour of unsaturated material is more complicated to model than that of its saturated counterpart because of the interaction among the three medium phases, i.e. soil, water, and air. This drawback limits the use of numerical models for field applications, especially for the real-time prediction of material behaviour. In the field, compaction using a roller

involves large deformation with complex nonlinear elastic–plastic behaviour, limiting the development of an adequate theoretical solution [71]. A close examination of the compaction process in the field allows several assumptions to be made, simplifying the modelling process. First, the compaction of the material is commonly performed at a designated moisture content, which is known a priori. The fact that the material is normally compacted at a moisture content usually at $\pm$ 2% of OMC simplifies model development [24]. In addition, the 3-D response of the material under field conditions may be approximated using a 1-D model discussed in detail in the Discussion section.

The material compaction response is crucial to calculate the number of passes of the roller required to achieve a target density. The problem of estimating the number of passes has been well-identified, and this estimation is commonly undertaken by trial and error. Figure 1 depicts the compaction process in the field or laboratory at a target moisture content, where the density increases (A, B, C, D) as the energy input to the soil increases, either by increased number of roller passes or blows of the Proctor hammer. It can be considered that the material is initially at a low-density state (point A) corresponding to a nominal pressure. As the energy input increases with the number of cycles (N) of compaction, the material state moves from point A to B to C, where the material reaches the line of optimums (LOO) corresponding to the optimum degree of saturation (S_{ropt}). On the basis of experimental evidence, Tatsuoka and Gomes Correia [60] highlighted that LOO is mostly unique for a certain soil, regardless of the mode of compaction, whether by Proctor hammer or by field rollers. Kodikara [23] and Kodikara et al. [25] highlighted the significance of S_{ropt}, when the air phase is trapped in a relatively continuous water phase. Hence, attempts to compact beyond this density (i.e. D) cause the material state to go to the wet side of the LOO, which can have undesirable effects of "over-compaction", such as heaving of the material with multiple shear planes and loosening of the already compacted material due to chaotic motions of the roller [4, 33]. Furthermore, experimental evidence indicates that material compacted to the wet side of LOO generally undergoes undesirable plastic deformation under repetitive loading similar to that expected from traffic loading [6, 30, 38]. It therefore follows that knowledge of the evolution of the density, and hence the degree of saturation, is beneficial for the development of an effective termination criterion during field compaction. This aspect is also addressed in the present paper.

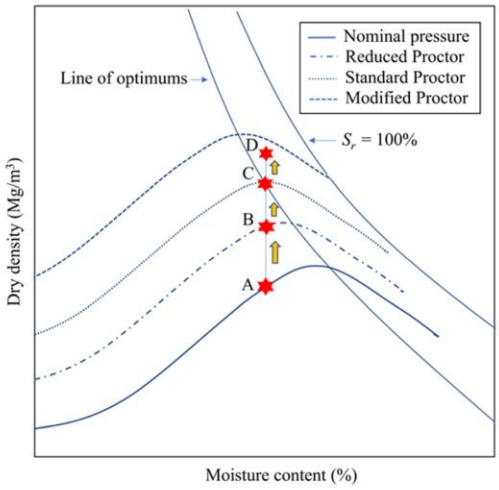

Fig. 1 Compaction process illustrated with a family of Proctor curves. The applied energy decreases in the following order: modified Proctor, standard Proctor, reduced Proctor, and nominal pressure

Based on the assumptions noted above, this paper attempts to simulate the compaction process using a simplified theoretical model (TM) based on the literature. The compaction behaviour of the material with respect to the degree of saturation is also highlighted using the simplified model. The lack of an appropriate constitutive model and a generalised TM necessitates the development of a data-driven machine learning (ML) model, as explored in this study. Further, the fusion of TM and ML models is also investigated. This paper shows that the fusion of TM and ML is a better model for noisy data which may come from data collected from the field because of uncertainties involved with testing, measurement, limitations of the equipment used, and human error.

2 Machine learning approaches

2.1 Artificial neural networks (ANNs)

ANNs are an ML tool for modelling and solving nonlinear relationships between input and output data [5]. They are considered to be data-driven models with an unrestricted number of model parameters, and are very useful when there is a large amount of data. There are numerous applications of ANNs, and some examples include image classification [40], regression [49], forecasting [26] and real-time optimisation [63].

A neural network structure consists of three distinct layers: an input layer, hidden layer, and an output layer. This multi-layer system is also known as a multi-layer perceptron (MLP). During ANN model training, the input layer, which can have one or many nodes, passes the information to the nodes of the hidden layers. The

information from a node is multiplied by a weight matrix, denoted as W, and added to a value called a bias matrix, denoted as b. The output is then passed to an activation function F. This process continues between each node until the information finally reaches the output layer. Function F is the activation function, which in this study, incorporates a rectified linear unit (ReLU) for the hidden layers, and a linear function at the output layer [14]. The network architecture and equations for a fully connected network can be found in any standard textbook, for example [14].

The predicted output (Y_{ML}) is compared to the actual output (Y) by computing the loss function (L) according to the mean absolute error (MAE), for this study and the regularisation loss function L_{reg}, as

$$\text{Loss function (MAE)} = L(Y, Y_{\mathrm{ML}}) = \frac{1}{\mathrm{len}(Y)} \sum_{i=1}^{\mathrm{len}(Y)} |Y - Y_{\mathrm{ML}}|, \quad (1)$$

$$L_{\mathrm{reg}} = \lambda_{\mathrm{reg}} \parallel W \parallel, \quad (2)$$

where, $\mathrm{len}(Y)$ represents the length of matrix Y and λ_{reg} represents the regularisation hyperparameter [14]. The total loss $L + L_{\mathrm{reg}}$ is minimised using the back-propagation algorithm by adjusting the values of W and b. Once training of the model is achieved, the trained model is used to predict new sets of data.

The performance of the models was also measured using root mean-squared error (RMSE), which is defined as

$$\mathrm{RMSE}(Y, Y_{\mathrm{pred}}) = \sqrt{\frac{1}{\mathrm{len}(Y)} \sum_{i=1}^{\mathrm{len}(Y)} (Y - Y_{\mathrm{pred}})^2}, \quad (3)$$

where Y_{pred} in general is the predicted output from any models.

2.2 Machine learning approaches to geotechnical prediction

Recent developments in data science, such as ML and especially deep learning (DL) models including ANNs, support vector machines (SVMs), and Gaussian process regression (GPR), have helped research scientists and engineers use the data available from measurements in various geotechnical applications [16, 19, 32, 35, 44, 73, 75]. For instance, data-driven models for capturing the complex behaviour of soil compaction in estimating the material properties for quality assurance (QA) and quality control (QC) purposes have recently been considered and integrated with IC [17]. In particular, the response of the drum reaction (i.e. the acceleration history) of the roller's vibratory drum is used to estimate the in situ states of the compacted material (e.g. modulus and roller-related stiffness) [7, 10]. However, the use of the purely data-driven ML models has the following disadvantages:

(1) *Non-adherence to underlying physics* Data-driven ML models are generally not able to follow the underlying physics, since the models are normally trained on a limited set of data representing limited conditions. In other words, they have been found to produce results which deviate from known mechanistic behaviour or scientific principles [20].
(2) *Prone to overfitting* Data-driven models may learn the training data rather than the underlying patterns and perform poorly on unseen test data [51]. Various regularisation techniques address this issue and are discussed later in this article.
(3) *Less interpolation ability* ML models tend to have greater errors in a sparse dataset even when predicting within the range of training datasets [45].
(4) *Less extrapolation ability* Similar to all empirically based models, ML models have found it challenging to make correct predictions beyond the range of training data [45].

2.3 Comparison of TM and ML

The development of a TM for a complex process, such as field compaction, requires an understanding of the complex interactions between the material and the roller compactor, and is limited by parameter availability and incomplete technical embodiment. Calibration of a TM's parameters can also be a challenge because of the combinatorial nature of the search space, which may result in over-complex models [21]. Conversely, ML algorithms have been considered a "black box" because of the models' hidden complexity and the fact that they may produce outputs which lack physical meaning, and this limits their use [27]. Hence, it is prudent to consider combining the TM and ML algorithms with a view to utilising their respective strengths and reducing their respective drawbacks [18, 45–48]. In other words, ML model complexity is reduced by incorporating theoretical and scientific knowledge through the TM [45]. This approach is known as theory-guided machine learning (TGML), which uses theoretical knowledge or frameworks to guide the construction and training of ML and DL.

The TGML framework can be applied to any domain using theoretical and physics-based knowledge and available data. TGML techniques have been applied to solve differential equations [46] and cyber-physical systems [45], but there has been very limited use in the Civil or Geotechnical engineering domains focused on liquefaction assessment and groundwater flow modelling [11, 74]. Accordingly, this paper presents the TGML framework,

combining the use of TM and ML in three other ways to predict material density during compaction. The first technique (TGML1) addresses the ability to interpolate and extrapolate ML models by generating additional observations using already developed TM models. The second technique (TGML2) considers TM prediction as an additional input to ML training, and TGML3 presents a novel way of training ML models based on the underlying physics.

2.4 Bias variance trade-off

It is crucial to understand the bias variance trade-off to understand the workings of models, TM, ML and TGML. Models are developed on the training data, whereas, test data are used to evaluate the performance of developed models. Bias is the difference between a prediction of the model and the corresponding observed value, while variance is the variability of the model prediction for a given dataset, and reflects a measure of the prediction spread. A high-bias model is an oversimplified model which pays little attention to the data and thus fits the data poorly. Similarly, a high-variance model is a complex model which sometimes models the noise or error in the data, potentially leading to high error when unseen inputs are given to the model.

Figure 2 shows three models, A, B and C, representing a low bias-high variance model, a high bias high variance model and a low bias low variance model, fitted to a random dataset. The *X* and *Y* parameters in Fig. 2 represent the input and output data, respectively, for illustration purposes. Although Model A performs better on the training dataset, it is very complex, has more parameters, and may show poor prediction in the test dataset. Additional parameters imply a greater capacity for memorisation capacity and therefore perfect mapping with the expected and predicted values. Conversely, Model B may have a high bias representing significantly fewer parameters, producing poor predictive capability and high errors on both training and test data. Model C, which has low variance and low bias, is expected to yield better accuracy in both the training and test datasets.

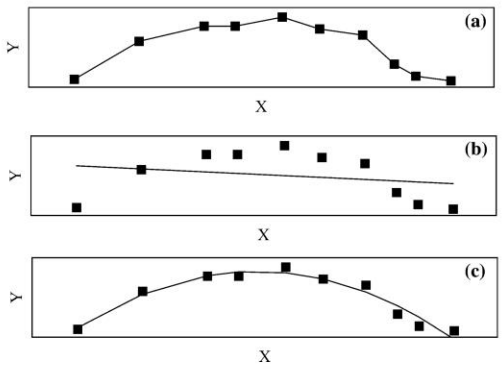

Fig. 2 **a** Model A: Low bias high variance model, **b** Model B: High bias high variance model, **c** Model C: Low bias low variance model (X and Y represent input and output data for illustration purposes)

Both TM and ML can be any of the above models; usually, ML and highly complex TM fall into the Model A category. Preferably, a model should fall into the category of Model C; this concept is further explained and used later in this paper.

2.5 Uncertainty in ML models

Trained neural network (NN) models produce only a single set of predictions when fed with test data or new data. Sometimes it is essential to know the level of confidence of the model outputs; hence, careful uncertainty quantification is crucial for practical applications.

Despite being able to handle complex processes with significant accuracy, NNs are poor at quantifying predictive uncertainty and often produce over-confident predictions [13, 28]. For example, suppose a NN trained on one dataset is evaluated on a completely different dataset. In that case, the network outputs high predictive uncertainty together with the prediction. The uncertainties associated with the model may also be because of uncertainties with the estimation of appropriate model weights and biases or be due to limited data availability. A measure of uncertainty provides users' confidence in the results obtained. Bayesian neural networks (BNNs), part of Bayesian approaches, are used to tackle uncertainties in NNs [22]. However, it has been found that BNNs can be very computationally expensive and require substantial customisation to training procedures [28, 53]. Recently, Gal and Ghahramani [12] introduced the Monte Carlo (MC) dropout to estimate model uncertainty. MC dropout is a variant of dropout used to prevent over-fitting [55]. Dropout refers to the temporary removal of nodes in a NN; as shown in Fig. 3, the dropped nodes are represented by shaded nodes. The selection of units to drop is random, with a dropout rate varying between 0 and 0.5, and the dropout rate refers to the fraction of nodes to be temporarily deactivated [55]. Uncertainty estimation using MC dropout requires making multiple predictions with different sets of nodes being dropped out. After the multiple predictions are completed, the mean and variance of the prediction are calculated.

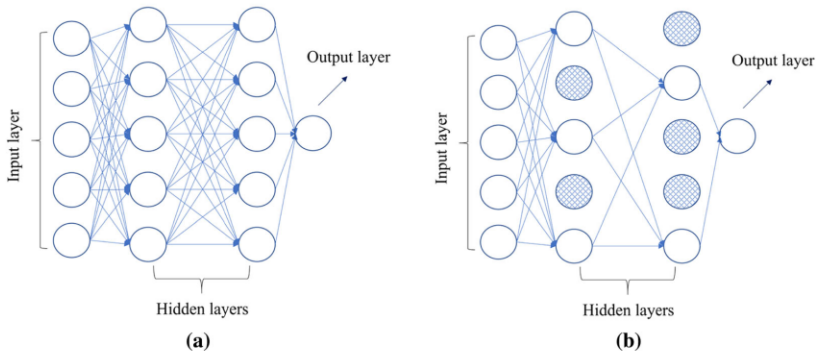

Fig. 3 Comparison between **a** A standard NN and **b** NN after dropout (shaded nodes have been dropped) (modified after Srivastava et al. 2014)

3 Materials and testing method

The simulation of field compaction in a laboratory is a challenge, and very limited data are available in the literature, as it involves loading the sample up to 2 MPa of stress at around 18–30 Hz of vibratory loading [39, 50]. Hence, experiments were carried out in the laboratory with loading conditions which had some essential features of field compaction by roller. Table 1 shows the physical properties of the uniformly graded fine sand (FS) used for this study. One load cycle of repetitive loading simulating compaction is shown in Fig. 4. The samples were compacted at different initial void ratios (e_0) and moisture contents (w) in a modified Proctor mould (diameter 151.5 mm and height 132.2 mm) and were subjected to varying loading conditions, as given in Table 2.

All the samples were subjected to a total of 30 cycles (N). Static stress (σ_s), vibratory stress (σ_v), duration for vibratory load (T_v), and frequency of vibration (f) were chosen such that they imitated actual field compaction and were varied to determine their effects on compaction. The static stress (σ_s) reflects the stress due to the static weight of the roller, whereas σ_v corresponds to the vibratory load of the roller. The experimental testing program is given in Table 2.

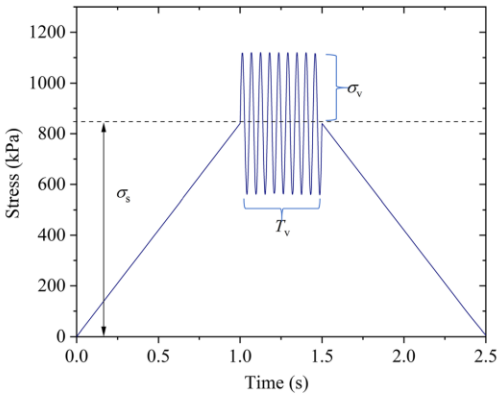

Fig. 4 First cycle loading profile applied to samples showing static stress (σ_s); vibratory stress (σ_v); duration of vibratory load (T_v)

Table 1 Geotechnical properties of material FS used in this study

Geotechnical property	Value	Standard
Specific gravity (G_S)	2.61	AS 1289.3.5.2 [56]
Median diameter (D_{50}) mm	0.35	AS 1289.3.6.1 [57]
MDD standard Mg/m^3	1.69	AS 1289.5.1.1 [58]
OMC standard (%)	11.74	AS 1289.5.1.1 [58]
Optimum degree of saturation (S_{ropt}) (%)	57	AS 1289.5.1.1 [58]
Coefficient of uniformity (C_u)	2.27	AS 1289.3.6.1 [57]
Coefficient of curvature (C_c)	0.97	AS 1289.3.6.1 [57]
Unified soil classification system (USCS) classification	SC	AS 1289.3.6.1 [57]

Table 2 Experimental program undertaken for this study with varying initial conditions and stress levels

Sample ID	w(%)	e_0	f(Hz)	σ_s(kPa)	σ_v(kPa)
FS_1	0	0.632	18	840	280
FS_2	5	0.789	18	840	280
FS_3	10	0.772	18	840	280
FS_4	5	0.780	18	840	280
FS_5	10	0.747	18	840	280
FS_6	7	0.904	18	840	280
FS_7	7	0.934	18	840	280
FS_8	0	0.645	18	1400	840
FS_9	15	0.871	18	840	280
FS_10	15	0.823	25	1400	840
FS_11	15	0.790	18	1400	840
FS_12	15	0.829	30	1400	840
FS_13	17	0.767	18	1400	840
FS_14	0	0.636	18	1400	840
FS_15	0	0.629	25	1400	840
FS_16	0	0.634	30	1400	840

4 Theoretical model development

The theoretical model used in this study is an extension of the semi-empirical plastic strain accumulation model proposed by Sawicki and Swidzinski [52], modified for 1-D zero lateral strain. These researchers developed the relationship for axial or volumetric plastic strain (ϵ^p) accumulation with N when the sample was subjected to maximum vertical stress ($\sigma_z = \sigma_s + \sigma_v$). Accordingly, for dry granular materials with different e_0 and σ_z,

$$\epsilon^p = C_1 \ln\left(1 + C_2(1 - K_0)^m N \sigma_z^m\right). \tag{4}$$

The stress-invariant (the stress tensor responsible for compaction) for Eq. (4) is considered to be $(\sigma_z - \sigma_x)^m$, which equals $(1 - K_0)^m \sigma_z^m$, where σ_x is the radial pressure and $(K_0 = \frac{\sigma_x}{\sigma_z})$ denotes the coefficient of lateral pressure, while C_1, C_2, and m are the material parameters. In the case of a 1-D oedometric test, since there are no lateral strains, the external work done on the sample by σ_x becomes zero, so the only work done is because of σ_z. Therefore, in the case of a 1-D condition, the σ_x term can be removed, and Eq. (4) can be approximated by Eq. (5). The stress term is normalised with $1kPa$:

$$\epsilon^p = C_1 \ln\left(1 + C_2 N \left(\frac{\sigma_z}{1\ \text{kPa}}\right)^m\right). \tag{5}$$

The evolution of ϵ^p is then written in terms of the evolution of the void ratio (e) with N,

$$e_N = e_0 - (1 + e_0) C_1 \ln\left(1 + C_2 N \left(\frac{\sigma_z}{1\ \text{kPa}}\right)^m\right), \tag{6}$$

where e_N is the void ratio at the Nth cycle, C_1, C_2 and m as functions of w, and other loading variables are presented later.

5 Experimental results

The stress–strain curve for sample ID FS_12 is shown in Fig. 5, showing that most of the compression occurs in the first cycle ($N = 1$) (in this sample 50% of total compression), and the compression rate then decreases with increasing N.

The relative change in the void ratio $(e_0 - e_{30})$ is an indicator of the maximum compression the sample undergoes during loading for N = 30, and is plotted against e_0 in Fig. 6. This shows that the degree of compaction, or in other words, the accumulation of ϵ^p, decreases with an increase in the packing density (decrease in e_0). In addition, the change in void ratio per cycle $\frac{de}{dN}$ decreases with N for all the samples; some examples are shown in Fig. 7. Figure 7 also shows the effect of stress level and the higher the stress level the faster the stabilisation of the void ratio.

5.1 Influence of frequency on compaction

Figure 8 shows the normalised relative change in the void ratio $\left(\frac{e_0 - e_{30}}{e_0}\right)$ plotted against the vibration frequency, illustrating that $\frac{e_0 - e_{30}}{e_0}$ displays a peak at what is referred to as the optimum compaction frequency (f_{opt}), which gives the maximum reduction in void ratio or increase in density (23 Hz for w = 15% and 25 Hz for w = 0%). A similar observation has been made for field compaction so, ideally, f_{opt} should be estimated before soil compaction for optimal

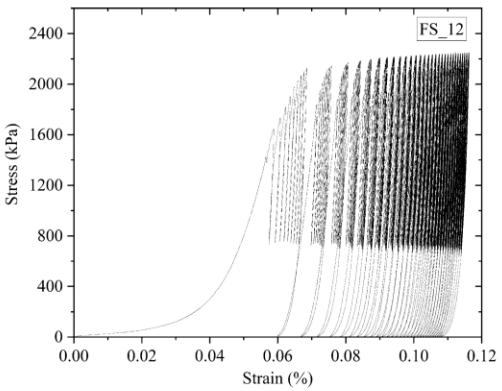

Fig. 5 Stress–strain curve for sample ID FS_12 subjected to vibratory loading

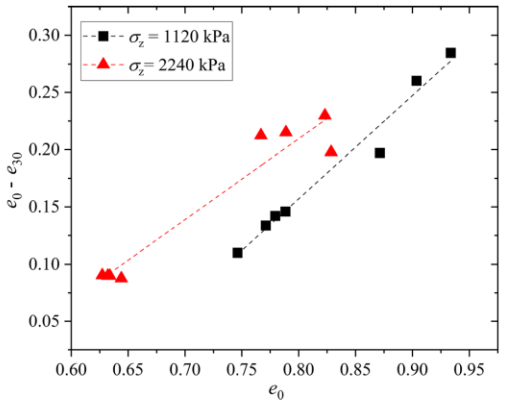

Fig. 6 Variation of $e_0 - e_{30}$ with e_0 for different stress levels (σ_z = 1120 kPa and σ_z = 2240 kPa)

operation of the rollers, thus saving energy costs and minimising potential damage to the rollers [67].

5.2 Effect of degree of saturation (S_r) on compaction

The effect of S_r is studied using Fig. 9, showing the variation of $\frac{e_0-e_{30}}{e_0}$ with S_r. Figure 9 shows that $\frac{e_0-e_{30}}{e_0}$ follows a similar trend to that of the compaction curve with the minima at around a S_r of 57%. This observation is consistent with that of past researchers, who reported that compaction curves with different compaction energies follow a similar trend (peak density or minimum e occurring at the same S_r as also seen in Fig. 1) irrespective of where those curves are developed, i.e., in the laboratory or field [24, 59–61].

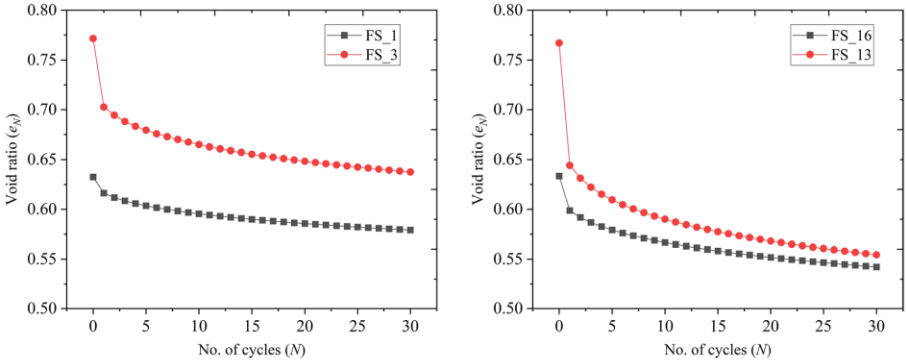

Fig. 7 Evolution of void ratio with number of cycles for different samples **a** at σ_z = 1120 kPa and **b** σ_z = 2240 kPa

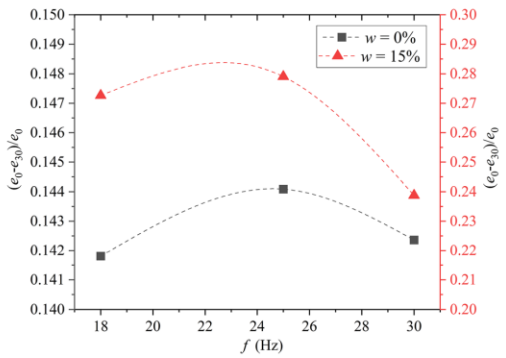

Fig. 8 $\frac{e_0-e_{30}}{e_0}$ is plotted against f for w = 0% (y-axis left) and 15% (y-axis right)

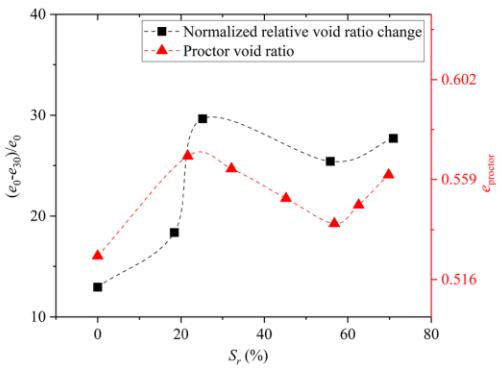

Fig. 9 Comparison with $\frac{e_0-e_{30}}{e_0}$ and Proctor void ratio (e_{proctor}) with S_r

5.3 Evaluation of C_1,C_2 and m

The model parameters (C_1, C_2, and m) were found using the least-squares fitting procedure. Exploratory analyses using Eq. (6) highlighted that this equation is over-parameterised, and removing C_2 helped reduce the standard error [3] in the estimation of m [72]. This was because the stress in this study was kept constant and the constant stress resulted in having a non-unique solution of C_2 and m. However, for study where the stress is not constant, C_2 would be required. The removal of C_2 reduced model complexity, this however, increased the model's bias, but decreased the model's variance, which is more advantageous for usage with the test data (not shown). In other words, Model A is changed to Model C (as discussed in Fig. 2). Hence, after removing C_2, Eq. (6) is reduced to

$$e_N = e_0 - (1+e_0)C_1 \ln\left(1 + N\left(\frac{\sigma_z}{1\,\text{kPa}}\right)^m\right). \quad (7)$$

The value of the exponent m increases with e_0, as shown in Fig. 10, with the rate of change differing for different stress conditions. This indicates that stress dependency increases with an increase in the e_0, implying that loose samples are more dependent on stress. However, the value of C_1 was found to be constant with values varying slightly within 0.014 ± 0.003.

6 Machine learning models

6.1 Hyperparameter tuning for ANNs

For this study, ANNs were used to model the dataset which comprised void ratios with the number of cycles from all the specimens with back-propagation algorithms. The void ratio at the N th cycle (e_N) was the target or output, whereas N, e_0, w, f, σ_z were the various input parameters considered with appropriate hyperparameters. The hyperparameters of any neural networks are the variables which govern the training process, speed, and accuracy of any ML model. There are two different types of hyperparameters: (a) model hyperparameters, which include the number and width of hidden layers; and (b) algorithm hyperparameters, which encompass the learning rate for optimisers such as stochastic gradient descent (SGD) or the Adam optimiser for training the model [14]. Since these variables remain constant over the training process and directly impact the ML program's performance, they should be selected before training any model. Usually, the hyperparameters are selected by trial-and-error for optimal performance, and the procedure is generally referred to as hyperparameter tuning or hyper-tuning. The hyperparameters of the ANN and the multi-output ANN for this study were selected/tuned using the Keras tuner and the optimum values obtained are listed in Table 3.

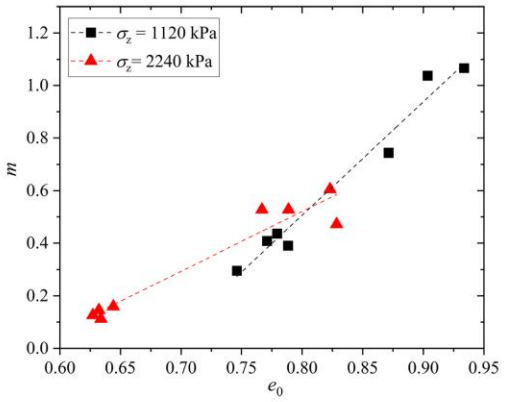

Fig. 10 Variation of model parameter m with e_0 for different stress levels ($\sigma_z = 1120$ kPa and $\sigma_z = 2240$ kPa)

6.2 Implementation of the ML models

All ML models were implemented in Python software and additional packages, including Keras, TensorFlow, Pandas, Numpy, and Seaborn [1, 8, 15, 36, 62, 64]. The Adam optimisation algorithm was used for performing back-propagation to evaluate the NNs model parameters with a maximum number of epochs equal to 10,000.

Various regularisation techniques were used to avoid over-fitting; first, by dividing the total dataset into training and test datasets randomly. For this study, 80% of the total dataset was used for training and 20% of the data for testing. An early stopping procedure was employed using a further 20% of the training data for validation to avoid overfitting. The value of patience for early stopping was kept equal to 500. L2 regularisation, also called Ridge regularisation, was also applied to force the weights to take small values, making weights more regular [14]. The complete dataset was normalised to zero mean and unity standard deviation to bring all parameters to the same scale. This normalisation was essential, because the model

Table 3 Hyperparameter details of the ANN used for this study

Hyperparameter	Value
No. of hidden layers (H)	1
No. of nodes in the hidden layer	4
Optimiser	Adam
Learning rate	0.1

inputs used different scales and ranges. Since these inputs are multiplied by the model weights, the scales of the outputs and gradients were affected by the inputs' scales. Although a model might converge without feature normalisation, this normalisation makes training much more stable.

The fully connected NN architecture comprised three layers: one input layer, one hidden layer and one output layer with 5, 4, and 1 nodes, respectively. The values of the hyper-parameters were kept the same in all models, demonstrating that no unique tuning of hyper-parameters was performed for a specific problem.

Figure 11 shows the effect of the different regularisation techniques used for this study (basic, callback and reguliser). The basic model had 10,000 epochs without any specific regularisation techniques. For the basic model, MAE fluctuated with epochs because of the constant learning rate; therefore, in the callback model, the learning rate was set to hyperbolically decrease with epochs for better convergence of MAE. The callback model also included the early stopping technique by monitoring the change in MAE; this also helped to save computational time in comparison with the basic model. The reguliser model included callback and L2 regularisation, and was better than the callback function in terms of time and cost, as shown in Fig. 11, where the model training stopped early at lower epochs. Henceforth, all the analysis was conducted based on the reguliser model's hyperparameters.

6.3 Extrapolation ability of TM and ML

The extrapolation ability of TM and ML was studied by splitting the experimental data into two parts: 1–20 cycles and 21–30 cycles. As shown in Fig. 12, both models were developed with data from 1 to 20 cycles, and their prediction accuracy was validated against the data from 21 to 30.

Figure 13 shows that TM and ML predicted unseen data and extrapolated well, as they have a low MAE and RMSE, although TM was slightly better than ML. As the model's prediction capability has been validated, in the subsequent sections of this article, the model is developed for the complete dataset (i.e. cycles 0–30), and the prediction is presented for cycles 31–50 beyond the measured data to demonstrate the model's extrapolation capability.

6.4 Uncertainty estimation of the ANN used in this study

For the present study, the data for sample FS_10 (randomly selected) were used to demonstrate the MC dropout. A different dropout ratio was considered to determine the effect of the dropout ratio on prediction accuracy and the 95% confidence band. The results of this analysis are shown in Fig. 14. The results indicate that the dropout ratios of 0.1 and 0.2 have lower MAE and a narrow confidence band. For the dropout ratios of 0.3 and 0.4, MAE increases together with the confidence band. Compared with no dropout (MAE = 2.7×10^{-3}), the dropout ratios of 0.1 and 0.2 perform better in terms of error, whereas 0.3 and 0.4 perform worse. Figure 14 also reveals that when predicting the void ratio for cycles 31–50, where training data were not available, the confidence band is broader than that for cycles 1–30, showing the model's higher uncertainty in extrapolation.

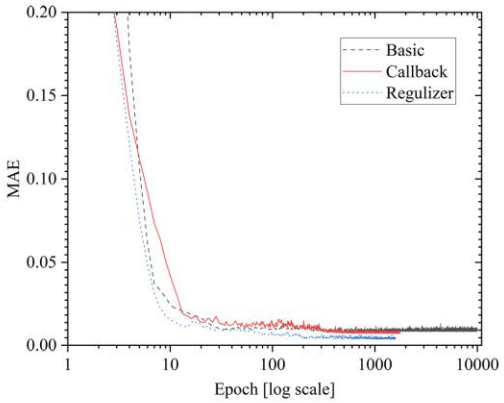

Fig. 11 MAE comparison of different regularisation models and variation with number of epochs (basic model, callback model and reguliser model)

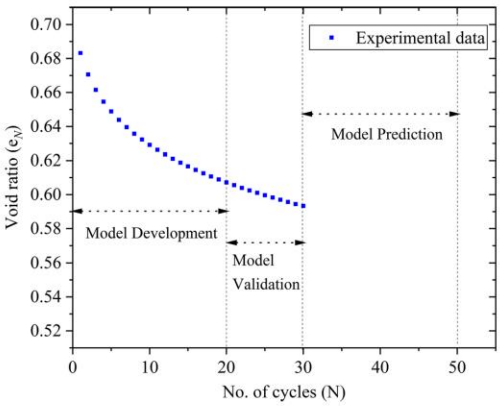

Fig. 12 Data splitting for model development, prediction validation, and model prediction

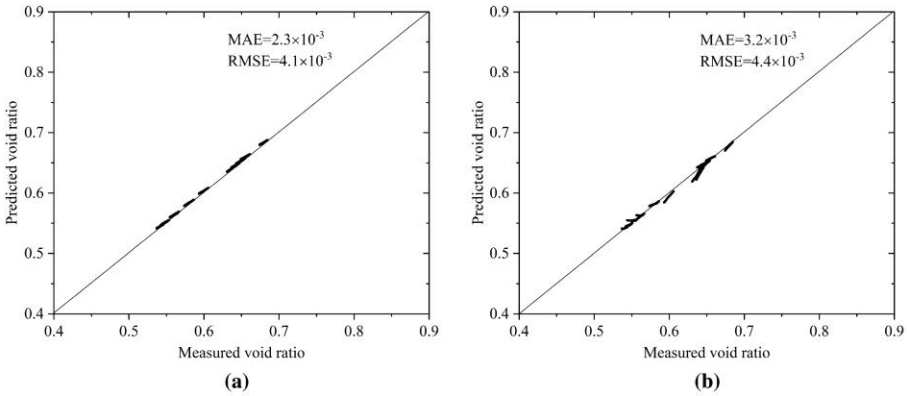

Fig. 13 Comparison of predicted and measured void ratio of **a** TM and **b** ML for the data of cycles 21–30

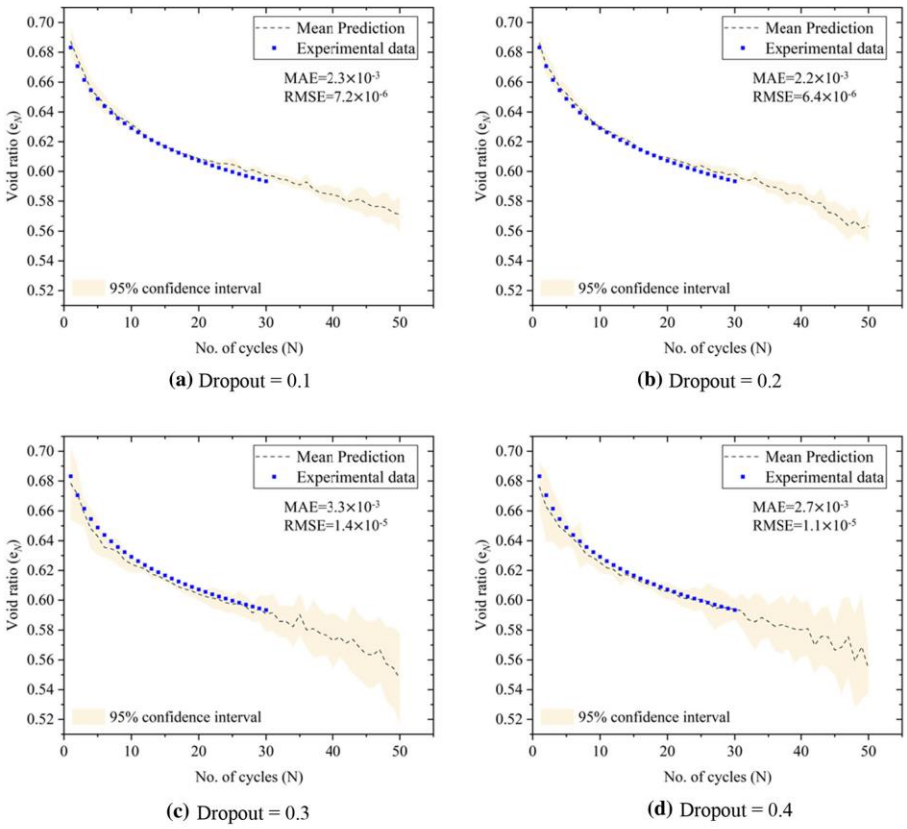

Fig. 14 Comparison of different dropout ratios **a** dropout ratio of 10%, **b** dropout ratio of 20%, **c** dropout ratio of 30%; and **d** dropout ratio of 40% on MAE, RMSE (for data up to 30 cycles), and confidence band

7 Theory-guided machine learning (TGML)

This section discusses the three techniques of TGML developed in this research to better predict the evolution of void ratio and eliminate the limitations associated with a theoretical model and machine learning-based models (in this study ANN). Schematic illustrations of the three TGML models are provided in Fig. 15, and their performance is measured and compared in subsequent sections.

7.1 Data augmentation (TGML1)

ML is a complex model which often attempts to learn the data used for training; it fits very well in the input domain and gives more substantial error when predicting outside the domain. Therefore, a complex ML model generally has a problem with extrapolation. This problem can be overcome by data augmentation from TM. Data augmentation is used to create or generate new observations to train an ML algorithm. Generally, prediction accuracy increases as the size of the input dataset increases. For example, in image classification problems, data scientists have managed to augment the data by adding a new image which is a rotated version of the original image [54]. Similarly, in the present research, the data augmentation technique using Eq. (7) was used to produce physics-based new data, as shown in Fig. 15c, with the model labelled TGML1. To use TM for data augmentation beyond the input's domain, the ability to extrapolate should be superior and was validated earlier in Fig. 13.

TGML1 saves time and resources in developing additional experimental data, preventing ML from overfitting, and improving prediction capability. To compare the efficiency of TGML1, first, ML was trained with experimental data of up to 30 cycles, as shown in Fig. 16a. Another network was trained with data of up to 50 cycles with observations from 31 to 50 cycles generated using Eq. (7), as shown in Fig. 16b. A comparison of the results reveals that the MAE calculated for cycles up to 30 of the TGML1 network was less than that of the network without augmentation, and the confidence band was narrow for the TGML1 network. In this case, because the model was trained with additional data, the accuracy of the prediction increased. It should be noted that model improvement using data augmentation depends on the extrapolation ability of TM, and in this case, the accuracy improved because the TM used in this study could extrapolate well.

7.2 Ingesting the output from TM as an additional input parameter to ML (TGML2)

In TGML2, the data were first pre-processed with the TM. The output of the TM was then used as an additional parameter for ML, as shown in Fig. 15d. In TM, the input was mapped to output $[X] \rightarrow [Y]$ by calibrating the model parameters using the experimental or observed data. Generally, in TM, assumptions are simplified, and simpler models are built; thus, TM predicts $[Y_{\mathrm{TM}}]$ as shown in Fig. 15a, which is not precisely equal to $[Y]$. Similarly, any ML model, when mapped from $[X] \rightarrow [Y]$ over a set of training data, predicts $[Y_{\mathrm{ML}}]$ and is not exactly equal to $[Y]$, as given in Fig. 15b. By adding the $[Y_{\mathrm{TM}}]$ to ML's input parameters, ML complements TM and captures the remaining complexity of the system. If the TM is highly accurate, then the TGML2 ensures $[Y_{\mathrm{TGML2}}] = [Y_{\mathrm{TM}}]$.

The prediction accuracy of TGML2 is compared in Fig. 17, indicating that the model which considers the output of the TM as an additional input (Fig. 17b) is an improvement over the model which does not consider the output of the TM as an additional input (Fig. 17a) in terms of MAE and RMSE.

7.3 Theory-guided regularisation (TGML3)

Theory-guided regularisation involves embedding the TM details in the loss function of ML. This way of embedding the TM in the loss function ensures that ML is constrained to comply with the theoretical model. The new architecture ensures that it penalises TM constraint violations by introducing additional regular loss function goals, as shown in Fig. 15e. The restriction is that with an increase in N, the e_N always decreases, which can be written as $e_N - e_{N+1} > 0$. The regular loss function was therefore modified by adding the TM-based loss function L_{TM}. The difference of the predicted void ratio as a pair was calculated as

$$\Delta_N = e_{N+1} - e_N. \tag{8}$$

A positive value of Δ_N can be viewed as a violation of physics. L_{TM} was therefore calculated as a non zero occurrence of $\mathrm{ReLU}(\Delta_N)$ summed over all the cycles, which is then multiplied by a suitable hyperparameter λ_{phy}. λ_{phy} is evaluated by trial-and-error like other hyperparameters in this study. The final equation for the L_{TM},

$$L_{\mathrm{TM}} = \lambda_{\mathrm{phy}} \sum_{N=1}^{N=30} \mathrm{ReLU}(\Delta_N). \tag{9}$$

The statistical evolution of TGML3 was done with a noisy dataset and is discussed in the next section.

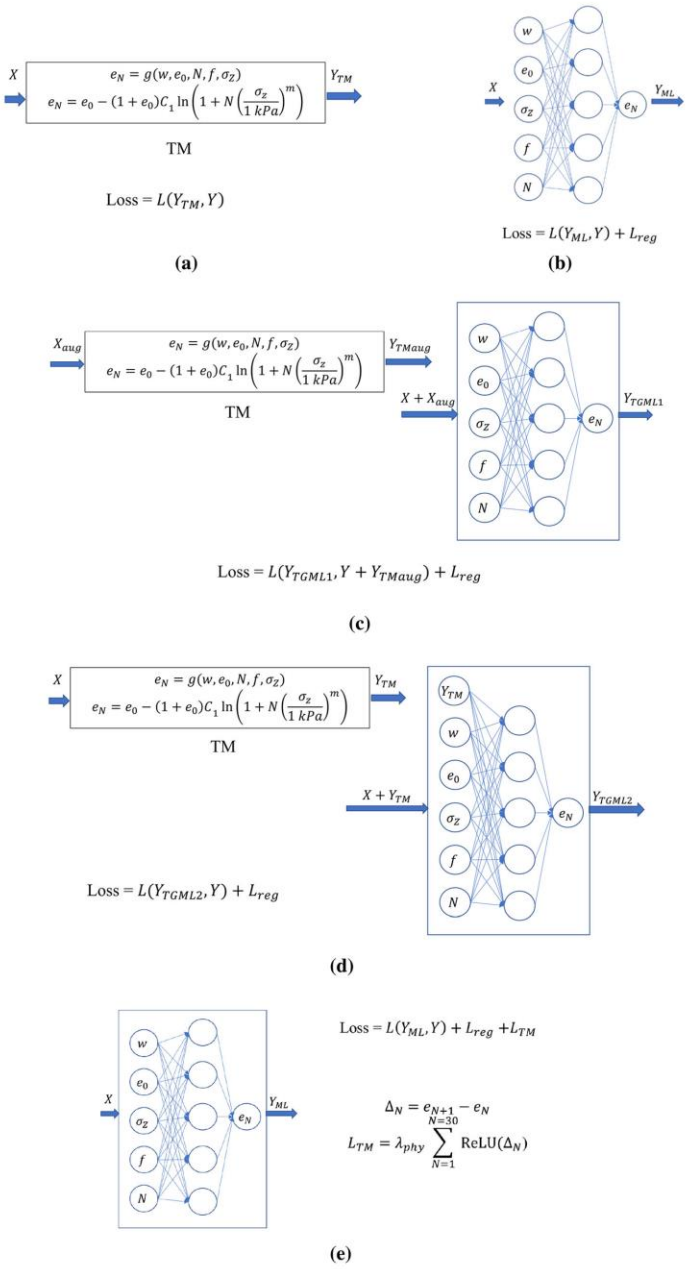

Fig. 15 Schematic illustrations of various techniques to estimate the evolution of void ratio with number of cycles **a** Model based on theory-based equation (TM). **b** Data-driven ML. **c** Data augmentation using TM (TGML1). **d** Ingesting the output from TM as an additional input parameter to ML (TGML2) and **e** Theory-guided regularisation (TGML3)

7.4 Robustness to noisy input data

In the real world, data are never perfect; they always contain some noise. Whether the data source is an electrical signal or collected from the laboratory or field environment, it is bound to be noisy because of uncertainties involved with testing, measurement, limitations of the equipment used, and human error. To evaluate the robustness of the model against noisy data, Gaussian noise $(\mathcal{N})$ was added to the experimental data. $\mathcal{N}$ is defined with the mean (μ) and variance (s^2) as $\mathcal{N} \sim (\mu, s^2)$. For this analysis, the μ of the noise was set to zero, whereas s^2 was set at 1% of μ of the data collected. A noisy observation $\left(Y_{\text{Noisy}}\right)$ is written as

$$Y_{\text{Noisy}} = Y + \mathcal{N} \sim \left(\mu, s^2\right). \tag{10}$$

Figure 18 compares the prediction of models with and without TGML 3. When calculating the MAE with prediction and noisy dataset, the MAE in the model with TGML3 shows a higher value. However, when the model's prediction is compared with the actual experimental dataset, the model with TGML3 provides MAE of 2.7×10^{-3} and RMSE of 1.5×10^{-5}, whereas the model without TGML3 provides MAE of 9.2×10^{-3} and RMSE of 1.1×10^{-4}. In addition, the model with TGML3 follows theoretical knowledge, and the void ratio decreases with the number of cycles. TGML3 performs better with noisy

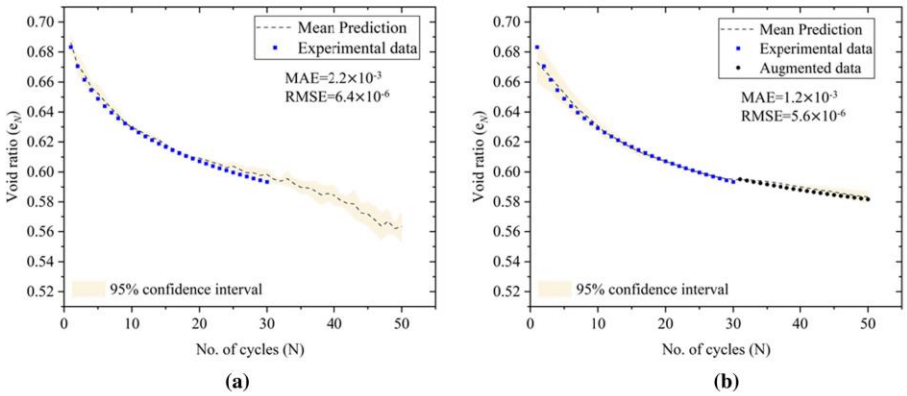

Fig. 16 Void ratio evolution with the number of cycles of dataset **a** without augmentation, **b** with augmentation and their prediction accuracy in terms of MAE and RMSE (for data up to 30 cycles)

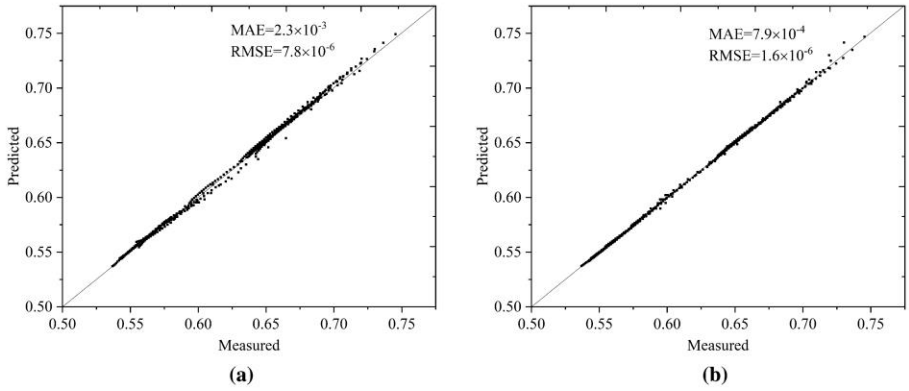

Fig. 17 Measured and predicted void ratio comparison of all samples **a** without considering TM output, **b** with considering TM output (TGML2) and their prediction accuracy in terms of MAE and RMSE (for data up to 30 cycles)

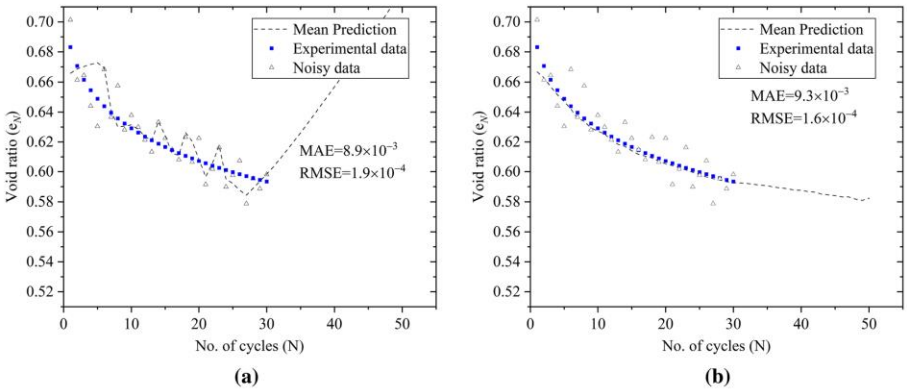

Fig. 18 Void ratio evolution of noisy dataset and prediction comparison of model **a** without TGML3, **b** with TGML3 and their prediction accuracy in terms of MAE and RMSE (for data up to 30 cycles)

data because combining TM and ML gives more complex models with high variance and low bias (Model A is changed to Model C as in Fig. 2). Therefore, when noise was added, the complex models tried to fit the noise and gave an error for the noise-free test data.

8 Termination criteria

The termination criteria, which are used to find the required number of cycles (N_{target}) to reach a target void ratio (e_{target}) or dry density for a given loading condition, can be measured using TGML in two different ways. First, the network needs to be trained again, but this time the output is N, where e_N is part of the input parameters. Retraining requires a substantial amount of time if the dataset is large. The second method of finding the N_{target} is by using the already trained model. This method is faster than the first method. The trained or learned TGML can be used to optimise the parameters for compaction using the back-propagation technique. The optimisation of one or more input parameters is the reverse of training a model. In training a model, the network parameters (weights and biases) are trained with fixed inputs, whereas optimising one or more input parameters is undertaken with fixed hyperparameters, which are known once the model is trained [70]. For the termination criteria, N_{target} to reach e_{target} is needed while the other input parameters and network parameters are fixed. This is a case of back-propagation optimisation where error is minimized to find the N_{target}. The differential equation solution to the optimisation problem is given by

$$N' = N_{\text{initial}} - \frac{\eta \partial E}{\partial N}, \tag{11}$$

where N_{initial} is the initial guess, E is the error (MAE) after the initial guess, η is the optimisation rate, and N' is the next prediction. The procedure continues until E is reduced to a minimum value. The optimisation algorithm was also executed in Python-based TensorFlow1. A simple illustration of this algorithm with parameters is shown in Table 4.

Using the data from Table 4 and TGML1 as the trained model, 41 cycles were required to reach the e_{target} of 0.62. The utilisation of TGML to calculate the termination criteria at the site has substantial practical applications. Currently, the required number of roller passes at the site to achieve the desired degree of compaction is obtained by doing some in situ density measurement, such as NDG testing, sampling, and other destructive testing methods. If the required number of passes can be estimated using TGML, the number of tests required can be substantially reduced, thus reducing the time and cost of the project. Moreover, as discussed earlier, it eliminates the disadvantages associated with over-compaction.

Table 4 Parameters and target values used for the study of termination criteria

Parameter	Value
e_0	0.823
$w(\%)$	15
f(Hz)	30
σ_z(kPa)	2240
e_{target}	0.62

9 Discussion

The compaction due to a roller in the field is not exactly 1-D compression. Figure 19a demonstrates the initial condition when the material is placed loosely, while Fig. 19b displays the instantaneous deformed shape of the material when a roller is in operation, and Fig. 19c illustrates the state of the material after compaction. While the deformation is not exactly 1-D, when the compaction is completed the overall deformation behaviour of the section can be approximated as 1-D. Wersäll et al. [66] and Wersäll and Larsson [65]concluded that the settlement behaviour from rotating mass oscillators, which are similar to vibratory rollers, is predominately vertical, and horizontal displacement is negligible. Recent results and the discussion illustrated in Fig. 19 support that deformation is predominately 1D; therefore, complex 3-D compaction can be approximated using 1-D equations.

A similar idea of approximating 3-D behaviour with 1-D equations has been proposed by Raissi and Karniadakis [46], who showed that any high fidelity data or model can be simulated using a low fidelity model with corrections. Likewise, data from field compaction (high fidelity data) can be well-represented by a low fidelity (1-D model) and corrections made using appropriate ML techniques. Therefore, it is believed that void ratio evolution data from the field can be modelled using a combination of the 1-D TM developed in the present study and a suitable ML model.

Laboratory test data on change in the void ratio of a fine sand during compaction were analysed and modelled using theoretical and ML approaches. Analysis of the experimental observations using TM showed that the model parameters and degree of compaction depend on different initial conditions, such as the initial void ratio (e_0), the degree of saturation (S_r), the load level (σ_z), and the frequency of vibration (f), as shown in Figs. 6, 7, 8, 9 and 10. The highlight of the analysis is shown in Fig. 9, which shows that the maximum relative compaction occurs when the sample is prepared close to the optimum degree of saturation (S_{ropt}) (S_{ropt} obtained from Proctor compaction testing). This phenomenological feature emphasises the importance of S_r during compaction, which has also been the focus of other recent studies [24, 59–61]. The importance of the vibration frequency for compaction is also highlighted in the analysis, i.e. there exists an optimum frequency at which the compaction is maximum. This observation is consistent with findings made during the field compaction of material, which also show an optimum frequency for maximum compaction [67, 68]. Ideally, this frequency should be evaluated before compaction starts for greater efficiency.

As discussed above, since model parameters depend on different initial conditions, TM cannot be generalised. Furthermore, with a large dataset, analysis using a TM would be challenging and computationally expensive. These issues were addressed with the use of 3-layer ANN models, which can generalise any loading condition. However, since ML models are prone to overfitting, different regularisation techniques, including callback and L2 regularisation, were used to reduce the error and decrease the computational time required to train the network.

It was also highlighted that greater accuracy could be achieved by combining data-driven ML models and TM encompassing essential physics, termed theory-guided machine learning (TGML). TGML increases the ability to interpolate and extrapolate, which is an essential aspect of the geotechnical engineering field [75]. TGML also reduces error and increases prediction confidence by reducing the 95% confidence band estimated using MC dropout. Noise in the dataset is unavoidable, especially measurements under field conditions. TGML provides much improved prediction in the case of noisy datasets compared with marginal improvement when dealing with clean laboratory datasets.

The termination criterion was discussed, which involves estimating the number of passes required to achieve a target density or void ratio. This analysis utilised the already-trained TGML1 model to predict the void ratio at any particular cycle, rather than re-training the model by interchanging the parameters, which could result in high computational cost.

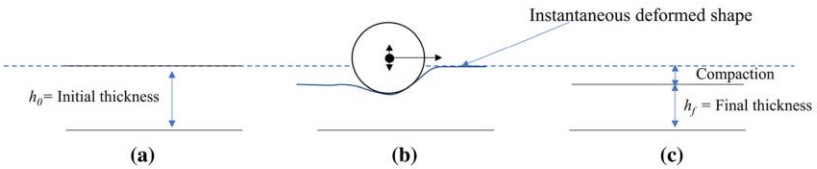

Fig. 19 Deformation pattern because of roller compaction; **a** initial loose soil, **b** instantaneous deformation pattern during compaction, **c** final deformed shape

10 Conclusions

A series of 1-D tests was conducted on uniformly graded fine sand with different initial densities and moisture contents. The loading condition simulated actual roller movement in terms of load level and frequency. The replication of roller loading conditions is challenging in the laboratory, as it involves applying loads as high as 2 MPa at a vibration frequency of 30 Hz, and there is an obvious lack of such data in the literature.

These data were analysed using a theoretical model based on the literature and an ANN model; both were found to be equally efficient in predicting the behaviour observed in the laboratory testing. Since the TM model parameters were dependent on initial conditions, TM could not be generalised. However, ML is more general, as it can consider all the parameters as an input, but its prediction lacked physical significance as it also tried to fit the noise of the data.

The fusion of TM and ML algorithms, termed TGML in this paper, addresses the disadvantages of TM and ML alone. The following conclusions on TGML were drawn:

1. TGML1, a data augmentation technique to improve ability to extrapolate, is an advantageous technique which addresses issues with the conduct of complex and expensive experiments. This technique involves the conduct of limited experiments for TM and using the developed TM to create new observations for any ML model. However, the extrapolation ability of TM should be
2. TGML2 considers the prediction of the TM as an additional input to the ML model. This method ensures that TM and ML complement each other. ML increases the complexity of a simpler 1-D TM, whereas TM restricts the prediction of ML to follow the physics involved in the compaction process.
3. TGML3 involves modification of the loss function of the ML model to include an additional loss function based on physical knowledge of the system. This involves rewriting the training steps to accommodate the additional loss term, but is very important, as shown in this paper. For this work, the constraint on void ratio was applied. This idea can be extended to other applications using different controls. For example, if the behaviour of material changes after S_{ropt}, the constraint could be provided in the model itself, rather than relying on the model to deduce it, which may not always be possible.
4. The highlight of this paper is the modelling of a noisy dataset. The paper shows that when modelling a clean dataset obtained from laboratory testing, TGML is marginally better than ML and TM; however, when dealing with noisy datasets, the prediction of TGML is far superior to that of ML.

The TGML techniques discussed above could also be combined if an individual TGML model cannot capture a complex behaviour. For example, if the dataset is noisy and the model's ability to extrapolate needs to be improved, TGML1 and TGML3 can be combined. In this paper, the application of the TGML is shown for ANNs only; however, the same concept can be used for other ML algorithms such as support vector regression (SVR) and random forest (RF). The ML and TM should be carefully selected for developing the TGML. Accordingly, the ML should be relatively simple and flexible for merging with the TM, which should be reasonably accurate. It should be noted that a very poor-quality TM can cause the hybrid model to have unsatisfactory performance compared to the ML model alone.

Acknowledgements The first author received a Monash University Graduate Scholarship (MGS) to undertake this research project. This research work is also part of a research project (Project No IH18.03.3) sponsored by the Smart Pavements Australia Research Collaboration (SPARC) Hub (https://sparchub.org.au) at the Department of Civil Engineering, Monash University, funded by the Australian Research Council (ARC) Industrial Transformation Research Hub (ITRH) Scheme (Project ID: IH180100010). The authors gratefully acknowledge the financial and in-kind support of Monash University, SPARC Hub, Construction, Infrastructure, Mining and Concessions (CIMIC), and Engineering, Innovation and Capability (EIC) activities.

Funding This study was supported by the Australian Research Council (ARC) Industrial Transformation Research Hub (ITRH) Scheme (Grant No. IH180100010).

Declaration

Conflict of interest The authors declare that they have no conflict of interest.

References

1. Abadi M, Barham P, Chen J, et al (2016) Tensorflow: a system for large-scale machine learning. In: 12th USENIX symposium on operating systems design and implementation (OSDI 16), pp 265–283
2. Allen JJ, Thompson MR (1974) Resilient response of granular materials subjected to time dependent lateral stresses. Transp Res Rec 1–13
3. Alper JS, Gelb RI (1990) Standard errors and confidence intervals in nonlinear regression: comparison of Monte Carlo and parametric statistics. J Phys Chem 94:4747–4751. https://doi.org/10.1021/j100374a068
4. Anderegg R, Kaufmann K (2004) Intelligent compaction with vibratory rollers: feedback control systems in automatic compaction and compaction control. Transp Res Rec J Transp Res Board 1868:124–134. https://doi.org/10.3141/1868-13

5. Braspenning PJ, Thuijsman F, Weijters AJMM (1995) Artificial neural networks: an introduction to ANN theory and practice. Springer, Berlin
6. Brown SF, Hyde AFL (1975) Significance of cyclic confining stress in repeated-load triaxial testing of granular material. Transp Res Rec. https://doi.org/10.1016/0148-9062(76)90013-9
7. Cao L, Zhou J, Li T et al (2021) Influence of roller-related factors on compaction meter value and its prediction utilizing artificial neural network. Constr Build Mater 268:121078. https://doi.org/10.1016/j.conbuildmat.2020.121078
8. Chollet F, others (2015) Keras
9. Chong SH, Santamarina JC (2016) Sands subjected to repetitive vertical loading under zero lateral strain: accumulation models, terminal densities, and settlement. Can Geotech J 53:2039–2046. https://doi.org/10.1139/cgj-2016-0032
10. Commuri S, Mai AT, Zaman M (2011) Neural network-based intelligent compaction analyzer for estimating compaction quality of hot asphalt mixes. J Constr Eng Manag 137:634–644. https://doi.org/10.1061/(ASCE)CO.1943-7862.0000343
11. Depina I, Jain S, Mar Valsson S, Gotovac H (2021) Application of physics-informed neural networks to inverse problems in unsaturated groundwater flow. Georisk Assess Manag Risk Eng Syst Geohazards. https://doi.org/10.1080/17499518.2021.1971251
12. Gal Y, Ghahramani Z (2016) Dropout as a Bayesian approximation: representing model uncertainty in deep learning. In: The 33rd international conference on machine learning ICML 2016, vol 3, pp 1651–1660
13. Ghahramani Z (2015) Probabilistic machine learning and artificial intelligence. Nature 521:452–459. https://doi.org/10.1038/nature14541
14. Géron A (2017) Hands-on machine learning with Scikit-Learn and TensorFlow: concepts, tools, and techniques to build intelligent systems. O'Reilly Media, Newton
15. Harris CR, Millman KJ, van der Walt SJ et al (2020) Array programming with NumPy. Nature 585:357–362. https://doi.org/10.1038/s41586-020-2649-2
16. He X, Xu H, Sabetamal H, Sheng D (2020) Machine learning aided stochastic reliability analysis of spatially variable slopes. Comput Geotech 126:103711. https://doi.org/10.1016/j.compgeo.2020.103711
17. Imran SA, Barman M, Commuri S et al (2018) Artificial neural network-based intelligent compaction analyzer for real-time estimation of subgrade quality. Int J Geomech 18:1–14. https://doi.org/10.1061/(ASCE)GM.1943-5622.0001089
18. Jia X, Karpatne A, Willard J et al (2018) Physics guided recurrent neural networks for modeling dynamical systems: application to monitoring water temperature and quality in lakes. In: 8th international workshop on climate informatics
19. Kang J, Zhaofeng C, Zhaoyu L, Wang SY (2021) Characterization of particle orientation of kaolinite samples using the deep learning-based technique. Acta Geotech. https://doi.org/10.1007/s11440-021-01266-x
20. Karpatne A, Atluri G, Faghmous JH et al (2017) Theory-guided data science: a new paradigm for scientific discovery from data. IEEE Trans Knowl Data Eng 29:2318–2331. https://doi.org/10.1109/TKDE.2017.2720168
21. Karpatne A, Watkins W, Read J, Kumar V (2017) Physics-guided neural networks (PGNN): an application in lake temperature modeling. arXiv:1710.11431
22. Khalaj S, BahooToroody F, Mahdi Abaei M et al (2020) A methodology for uncertainty analysis of landslides triggered by an earthquake. Comput Geotech 117:103262. https://doi.org/10.1016/j.compgeo.2019.103262
23. Kodikara J (2012) New framework for volumetric constitutive behaviour of compacted unsaturated soils. Can Geotech J 49:1227–1243. https://doi.org/10.1139/t2012-084
24. Kodikara J, Islam T, Sounthararajah A (2018) Review of soil compaction: history and recent developments. Transp Geotech 17:24–34. https://doi.org/10.1016/j.trgeo.2018.09.006
25. Kodikara J, Jayasundara C, Zhou AN (2020) A generalised constitutive model for unsaturated compacted soils considering wetting/drying cycles and environmentally-stabilised line. Comput Geotech 118:103332. https://doi.org/10.1016/j.compgeo.2019.103332
26. Kolarik T, Rudorfer G (1994) Time series forecasting using neural networks. ACM Sigapl Apl Quote Quad 25:86–94
27. Kumar D, Wong A, Taylor GW (2017) Explaining the unexplained: a class-enhanced attentive response (CLEAR). Arxiv 36–44
28. Lakshminarayanan B, Pritzel A, Blundell C (2017) Simple and scalable predictive uncertainty estimation using deep ensembles. Adv Neural Inf Process Syst 30:6403–6414
29. Lee J, Lacey D, Look B (2017) P60: Best practice in compaction QA for pavement and subgrade materials (year 1–2016/2017). www.nacoe.com.au. Accessed 25 May 2021
30. Lekarp F, Dawson A (1998) Modelling permanent deformation behaviour of unbound granular materials. Constr Build Mater. https://doi.org/10.1016/S0950-0618(97)00078-0
31. Li N, Wang X, Qiao R et al (2020) A prediction model of permanent strain of unbound gravel materials based on performance of single-size gravels under repeated loads. Constr Build Mater 246:118492. https://doi.org/10.1016/j.conbuildmat.2020.118492
32. Liu Z, Shao J, Xu W, Wu Q (2015) Indirect estimation of unconfined compressive strength of carbonate rocks using extreme learning machine. Acta Geotech 10:651–663. https://doi.org/10.1007/s11440-014-0316-1
33. Liu D, Wang Y, Chen J, Zhang Y (2019) Intelligent compaction practice and development: a bibliometric analysis. Eng Constr Archit Manag 27:1213–1232. https://doi.org/10.1108/ECAM-05-2019-0252
34. Look BG (2020) Overcoming the current density testing impediment to alternative quality testing in earthworks. Aust Geomech J 55:55–74
35. Makasis N, Narsilio GA, Bidarmaghz A (2018) A machine learning approach to energy pile design. Comput Geotech 97:189–203. https://doi.org/10.1016/j.compgeo.2018.01.011
36. McKinney W et al (2010) Data structures for statistical computing in python. In: Proceedings of the 9th python in science conference, pp 51–56
37. Modoni G, Koseki J, Anh Dan LQ (2011) Cyclic stress-strain response of compacted gravel. Geotechnique 61:473–485. https://doi.org/10.1680/geot.7.00150
38. Monismith CL, Ogawa N, Freeme CR (1975) Permanent deformation characteristics of subgrade soils due to repeated loading. Transp Res Rec, vol 537
39. Mooney MA, Rinehart RV (2007) Field monitoring of roller vibration during compaction of subgrade soil. J Geotech Geoenviron Eng 133:257–265. https://doi.org/10.1061/(asce)1090-0241(2007)133:3(257)
40. Park SB, Lee JW, Kim SK (2004) Content-based image classification using a neural network. Pattern Recognit Lett 25:287–300
41. Park J, Santamarina JC (2019) Sand response to a large number of loading cycles under zero-lateral-strain conditions: evolution of void ratio and small-strain stiffness. Geotechnique 69:501–513. https://doi.org/10.1680/jgeot.17.P.124
42. Pasten C, Shin H, Carlos Santamarina J (2014) Long-term foundation response to repetitive loading. J Geotech Geoenviron

Eng 140:1–11. https://doi.org/10.1061/(ASCE)GT.1943-5606.0001052
43. Pestana JM, Whittle AJ, Salvati LA (2002) Evaluation of a constitutive model for clays and sands: part I—sand behaviour. Int J Numer Anal Methods Geomech 26:1097–1121. https://doi.org/10.1002/nag.237
44. Pooya Nejad F, Jaksa MB (2017) Load-settlement behavior modeling of single piles using artificial neural networks and CPT data. Comput Geotech 89:9–21. https://doi.org/10.1016/j.compgeo.2017.04.003
45. Rai R, Sahu CK (2020) Driven by data or derived through physics? A review of hybrid physics guided machine learning techniques with cyber-physical system (CPS) focus. IEEE Access 8:71050–71073. https://doi.org/10.1109/ACCESS.2020.2987324
46. Raissi M, Karniadakis GE (2018) Hidden physics models: machine learning of nonlinear partial differential equations. J Comput Phys 357:125–141. https://doi.org/10.1016/j.jcp.2017.11.039
47. Raissi M, Perdikaris P, Karniadakis GE (2017) Machine learning of linear differential equations using Gaussian processes. J Comput Phys 348:683–693. https://doi.org/10.1016/j.jcp.2017.07.050
48. Raissi M, Perdikaris P, Karniadakis GE (2017) Inferring solutions of differential equations using noisy multi-fidelity data. J Comput Phys 335:736–746. https://doi.org/10.1016/j.jcp.2017.01.060
49. Rezaie-Balf M, Kisi O (2018) New formulation for forecasting streamflow: evolutionary polynomial regression vs. extreme learning machine. Hydrol Res 49:939–953. https://doi.org/10.2166/nh.2017.283
50. Rinehart RV, Mooney MA (2009) Measurement of roller compactor induced triaxial soil stresses and strains. Geotech Test J 32:347–357. https://doi.org/10.1520/gtj101889
51. Roelofs R, Fridovich-Keil S, Miller J et al (2019) A meta-analysis of overfitting in machine learning. Adv Neural Inf Process Syst 32:9179–9189
52. Sawicki A, Swidzinski W (1995) Cyclic compaction of soils, grains and powders. Powder Technol 85:97–104. https://doi.org/10.1016/0032-5910(95)03013-Y
53. Seoh R (2020) Qualitative analysis of Monte Carlo dropout. arXiv 1–13
54. Shorten C, Khoshgoftaar TM (2019) A survey on image data augmentation for deep learning. J Big Data. https://doi.org/10.1186/s40537-019-0197-0
55. Srivastava N, Hinton G, Krizhevsky A et al (2014) Dropout: a simple way to prevent neural networks from overfitting. J Mach Learn Res 15:1929–1958
56. Standards Australia (2002) Soil classification tests—determination of the soil particle density of combined soil fractions—vacuum pycnometer method. In: AS 1289.3.5.2
57. Standards Australia (2009) Soil classification tests—determination of the particle size distribution of a soil—standard method of analysis by sieving. In: AS 1289.3.6.1
58. Standards Australia (2017) Soil compaction and density tests—determination of the dry density/moisture content relation of a soil using standard compactive effort. In: AS 1298.5.1.1
59. Tatsuoka F (2015) Compaction characteristics and physical properties of compacted soil controlled by the degree of saturation. Geotech Synergy Buenos Aires 2015:40–78
60. Tatsuoka F, Gomes Correia A (2018) Importance of controlling the degree of saturation in soil compaction linked to soil structure design. Transp Geotech 17:3–23. https://doi.org/10.1016/j.trgeo.2018.06.004
61. Tatsuoka F, Correia AG (2016) Importance of controlling the degree of saturation in soil compaction. In: Procedia Engineering
62. Van Rossum G, Drake Jr FL (1995) Python reference manual. Centrum voor Wiskunde en Informatica Amsterdam
63. Wang Y, Salehi S (2015) Application of real-time field data to optimize drilling hydraulics using neural network approach. J Energy Resour Technol. https://doi.org/10.1115/1.4030847
64. Waskom ML (2021) Seaborn: statistical data visualization. J Open Source Softw 6:3021. https://doi.org/10.21105/joss.03021
65. Wersäll C, Larsson S (2013) Small-scale testing of frequency-dependent compaction of sand using a vertically vibrating plate. Geotech Test J 36:394–403. https://doi.org/10.1520/GTJ20120183
66. Wersäll C, Larsson S, Rydén N, Nordfelt I (2015) Frequency variable surface compaction of sand using rotating mass oscillators. Geotech Test J 38:198–207. https://doi.org/10.1520/GTJ20130193
67. Wersäll C, Nordfelt I, Larsson S (2017) Soil compaction by vibratory roller with variable frequency. Geotechnique 67:272–278. https://doi.org/10.1680/jgeot.16.P.051
68. Wersäll C, Nordfelt I, Larsson S (2018) Resonant roller compaction of gravel in full-scale tests. Transp Geotech 14:93–97. https://doi.org/10.1016/j.trgeo.2017.11.004
69. Wichtmann T (2005) Explicit accumulation model for non-cohesive soils under cyclic loading. PhD. Thesis, Inst für Grundbau und Bodenmechanik Phd:274
70. Wu G, Say B, Sanner S (2017) Scalable planning with tensorflow for hybrid nonlinear domains. arXiv 1–11
71. Xu G, Chang GK (2020) Continuous compaction control—mathematical models and parameter identification. In: Springer series in geomechanics and geoengineering, pp 563–584
72. Yu J, Liu L, Collins RL et al (2014) Analytical problems and suggestions in the analysis of behavioral economic demand curves. Multivariate Behav Res 49:178–192. https://doi.org/10.1080/00273171.2013.862491
73. Zhang P, Jin ZYY (2021) Modelling the mechanical behaviour of soils using machine learning algorithms with explicit formulations. Acta Geotech. https://doi.org/10.1007/s11440-021-01170-4
74. Zhang Y, Wang R, Zhang J-M, Zhang J (2020) A constrained neural network model for soil liquefaction assessment with global applicability. Front Struct Civ Eng 14:1066–1082. https://doi.org/10.1007/s11709-020-0651-2
75. Zhang P, Yin Z-Y, Jin Y-F (2021) State-of-the-art review of machine learning applications in constitutive modeling of soils. Arch Comput Methods Eng. https://doi.org/10.1007/s11831-020-09524-z

Publisher's Note Springer Nature remains neutral with regard to jurisdictional claims in published maps and institutional affiliations.

4.2 Errata and Addenda for the published paper (Tophel et al. 2022)

4.2.1 Errata

Erratum 1: In Table 1, Unified soil classification system (USCS) classification value is reported as SC.

Correction: Unified soil classification system (USCS) classification value should be SP.

Erratum 2: In section 6.2 it is written as: "Various regularisation techniques were used to avoid over-fitting; first by dividing the total dataset into training and test datasets randomly. For this study, 80% of the total dataset was used for training and 20% of the data for testing. An early stopping procedure was employed using a further 20% of the training data for validation to avoid overfitting."

Correction: This should be modified to: "Various regularisation techniques were used to avoid over-fitting; first by dividing the total dataset into training and test datasets randomly. For this study, 80% of the total dataset was used for training and 20% of the data for testing. An early stopping procedure was employed using a 20% of the training data for validation to avoid overfitting."

Erratum 3: At the start of section 7, it is written as: "This section discusses the three techniques of TGML developed in this research to better predict the evolution of void ratio and eliminate the limitations associated with a theoretical model and machine learning-based models (in this study ANN)."

Correction: The text should be modified to: "This section discusses the three techniques of TGML developed in this research to better predict the evolution of void ratio. These techniques aim to address the limitations associated with a theoretical model and machine learning-based models, particularly the ANN model used in this study."

4.2.2 Addenda

Addendum 1: The grain size distribution of the material used in this study is shown in Figure 4-1.

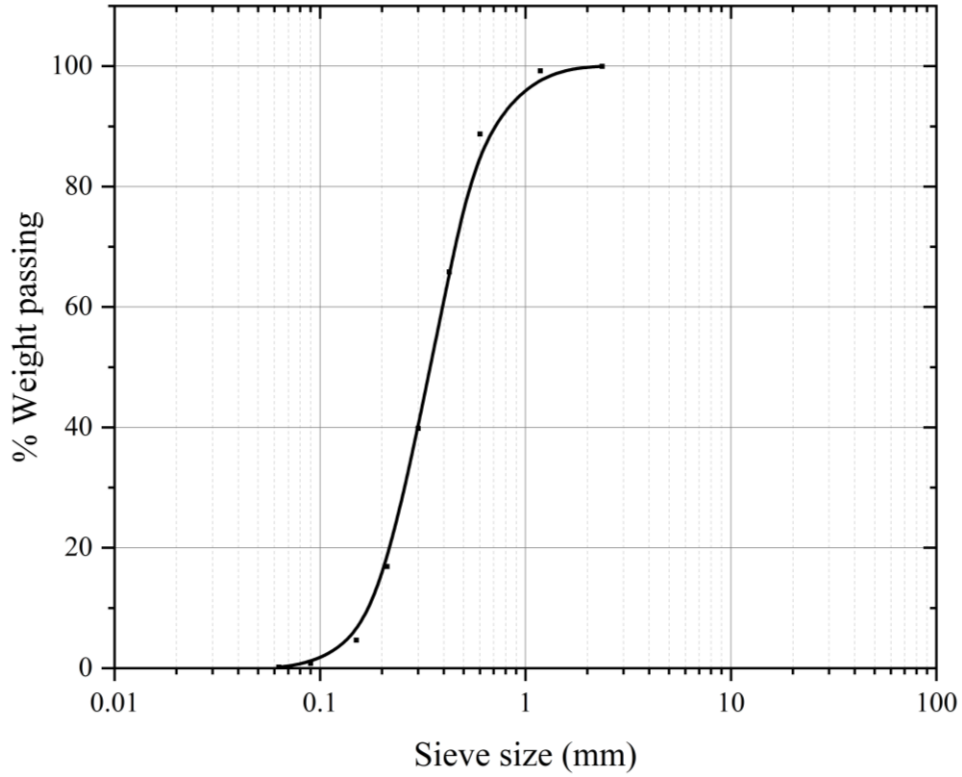

Figure 4-1. Grain size distribution of the material used in (Tophel et al. 2022).

Addendum 2:

For FS_10, the parameters were evaluated using Eq. (6) which resulted the value of parameters as provided in Table 4-1. It can be seen that the error in evaluating C_2 and m is very high.

Table 4-1. Model parameters obtained for sample FS_10 with equation including C_2.

Parameter	Value	Error
e_0	0.82306	0.00242
C_1	0.01543	0.00060
C_2	0.27481	415.629
m	0.84874	214.834

However, when the model complexity was reduced by eliminating C_2, following were the values and errors obtained.

Table 4-2. Model parameters obtained for sample FS_10 with equation without including C_2.

Parameter	Value	Error
e_0	0.82306	0.00238
C_1	0.01543	0.00028
m	0.66478	0.02278

It can be seen that the error in obtaining parameter m reduced when the model complexity was reduced.

Addendum 3: In section 7.1, coefficients calibrated for Equation 7 and the ML study to 30 cycles were carried out independently.

Addendum 4: In section 7.4, a variance of 1% of mean was chosen as an appropriate amount of noise based on (Raissi et al. 2017b).

Addendum 5: A detailed discussion on 1D approximation of roller compaction can be found in Chapter 7.

Addendum 6: In practice, a section of trial compaction will be needed to calibrate TM or ML. A detailed discussion on this can be found in Chapter 7 of the thesis.

4.3 Summary

The development of a hybrid model called TGML has been presented, combining the strengths of theoretical models (TM) and machine learning (ML) algorithms to overcome their individual limitations in predicting noisy datasets. Three different techniques were used to combine TM and ML, named TGML1, TGML2, and TGML3. TGML1 involves augmenting the dataset for ML with the limited data from TM, TGML2 uses the prediction of TM as an additional input to the ML model, and TGML3 modifies the loss function of ML to include physical constraints. The superiority of TGML over TM and ML in predicting noisy datasets was highlighted. Importantly, the framework can be extended to other ML algorithms, such as support vector regression (SVR) and random forest (RF), although the quality of the TM is crucial for the performance of the hybrid model.

The framework was tested on fine sand compacted at varying moisture contents, stress levels, and loading frequencies. The three techniques that were used to improve the framework's performance were discussed, with the third technique being particularly useful for handling noisy field datasets. The developed TGML framework was also used to demonstrate a termination criterion for achieving the desired degree of compaction, and a simplified TM and ML model were proposed to estimate field compaction behaviour during roller movement. The TGML framework showed less error and lower model uncertainty than traditional machine learning methods. In Chapter 7, TGML3 is used to remove the uncertainty associated with measuring the deformation data.

Chapter 5 Constitutive model for a constant load test

This is the second chapter of Part 3: Theoretical Model Development. Chapter 4 discussed the use of a simplified model to study the material behaviour based on constant stress 1D tests for practical purposes. However, roller compaction involves variable stress due to the gradual reduction of contact area between the drum and geomaterial, making it difficult to predict the density using a constant stress test-based model. This study extends the model developed in Chapter 5 and proposes a simplified constitutive model that uses the geometric relationship between contact width and incremental plastic deformation to approximate the complex compaction process with very high accuracy. The simplified model eliminates the need for a complex model, making it suitable for real-time application.

To simulate roller compaction in the field, this study used a novel laboratory-scale steel foot compactor to compact four unbound granular materials (UGM) at varying moisture content. Experimental data were used to develop the model for estimating variable stress conditions during compaction. This model was then used to predict dynamic properties such as modulus, stiffness and density during compaction. In Chapter 7, the model was utilized to guess the initial void ratio of the material with the deformation measurement.

The first part of the chapter is based on the published research paper:

- **Tophel A**, Walker JP, Dutta TT, Bodin D, Kodikara J (2023) Model development to predict dynamic interactions of roller and geomaterial using simulated roller compaction. *Transportation Geotechnics* 39:100946. https://doi.org/10.1016/j.trgeo.2023.100946.

The chapter then provides errata for the published paper and then details the use of the model developed and other studies to examine the influence of initial state on modulus and density. The chapter then concludes with a section summarizing the findings.

5.1 Model development to predict dynamic interactions of roller and geomaterial using simulated roller compaction

Transportation Geotechnics 39 (2023) 100946

Contents lists available at ScienceDirect

Transportation Geotechnics

journal homepage: www.elsevier.com/locate/trgeo

Model development to Predict Dynamic Interactions of Roller and Geomaterial using Simulated Roller Compaction

Amir Tophel [a], Jeffrey P. Walker [b], Troyee Tanu Dutta [a], Didier Bodin [c], Jayantha Kodikara [a,*]

[a] ARC Industrial Transformation Research Hub (ITRH) – SPARC Hub, Dept. of Civil Engineering, Monash University, Clayton Campus, VIC 3800, Australia
[b] Dept. of Civil Engineering, Monash University, Clayton Campus, VIC 3800, Australia
[c] Australian Road Research Board (ARRB), Port Melbourne, VIC 3207, Australia

ARTICLE INFO

Keywords:
Contact Stress
Wheel Tracker
Plastic Deformation
Roller Compaction
Modulus
Density

ABSTRACT

Crushed rock or unbound granular materials constitute the top layer of geomaterial compacted in a pavement. These materials are required to be compacted using compactors or rollers at a designated target density or modulus for satisfactory performance. Studying the interaction between compactors and geomaterial is important for optimising these geomaterial layers' construction. As field compaction is time-consuming and cumbersome, the study of material behaviour at a smaller scale is necessary. This study utilises a novel setup simulating the field compaction better to study the material's behaviour and dynamic interaction between the material and the compactor during compaction. A constitutive model was developed utilizing the geometric relationship between the contact width to plastic deformation during compaction, which can be easily measured. Using Hertzian theory, the estimation of contact width allows the estimation of contact stress. The developed model shows that it can model the experimental observation with very high accuracy ($R^2 > 0.98$). The model is then used to predict other geomaterial properties during compaction, showing their dependence on the material state.

Introduction

Construction of roads, dam embankments and bridges are the major activities in the civil engineering domain. These activities are very important to cope with the ever-increasing population. All of these construction activities require an assessment of the suitability of the ground condition of a construction location, including the geomaterial layers on which a structure is built. For instance, if the geomaterial is weakly compacted, a structure built over it will not operate well, and in the case of a road, the service life of the road is lowered, leading to premature failure. The construction of geomaterial layers to specified dry density (ρ_d) or void ratio (e) and other geomaterial properties (e.g., stiffness (K), modulus (E)) are typically required for the quality assurance (QA) of engineered compaction.

On top of that, it is also crucial to minimise material variability within geomaterial layers to prevent structural failures resulting from excessive differential deformations. The compaction of geomaterial to a specified property is commonly undertaken using rollers/compactors. Geomaterial compaction is therefore the process of increasing ρ_d and thus reducing e by removing air voids by applying loads. When geomaterials are compacted, the geometry of the particles' arrangement is altered, resulting in a better packing arrangement and an increase in ρ_d. The compaction process is very complex to explain scientifically in detail. Hence, there are many issues with the current approaches.

First, capturing the cyclic loading and unloading process during compaction is an ongoing challenge because the material is unsaturated constituting the three-phase media. Numerous researchers have attempted to model the behaviour of unsaturated materials under complicated cyclic loads at the laboratory scale using complex analytical and finite element models [1–6]. These models capture some of the complicated behaviour well, but the determination of model parameters requires complex time-consuming experiments, especially for unsaturated geomaterials. A simplified constitutive model was proposed by Sawicki et al. [7], which was recently modified by the authors of this paper [8], who showed that for practical purposes a simplified model could be used to capture the essential physics of the compaction process. This model requires fewer material parameters and is advantageous, especially when aiming at future real-time applications. Unfortunately, similar to other constitutive models, the model needs applied parameters such as stress as an input, which is variable during compaction.

* Corresponding author.
E-mail addresses: amir.tophel@monash.edu (A. Tophel), jeff.walker@monash.edu (J.P. Walker), troyee.dutta@monash.edu (T.T. Dutta), didier.bodin@arrb.com.au (D. Bodin), jayantha.kodikara@monash.edu (J. Kodikara).

https://doi.org/10.1016/j.trgeo.2023.100946
Received 25 October 2022; Received in revised form 22 January 2023; Accepted 24 January 2023
Available online 28 January 2023
2214-3912/© 2023 Elsevier Ltd. All rights reserved.

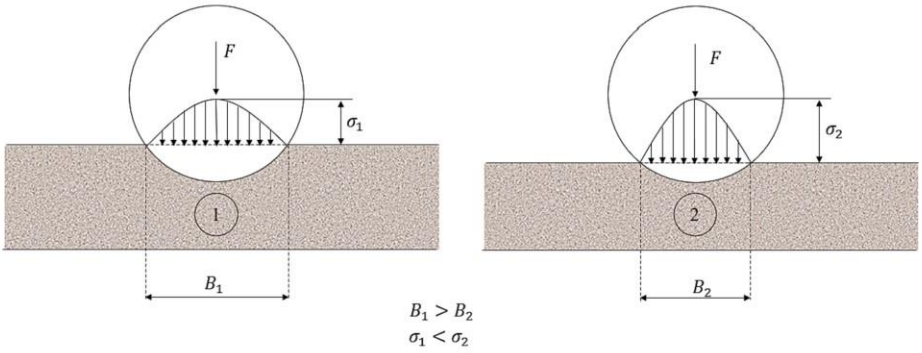

Fig. 1. Interaction between cylindrical roller compactor and material with different states: (a) loose state (state 1); (b) dense state (state 2).

The compaction process modelling using rollers is challenging due to the change in the geomaterial properties (stiffness, ρ_d, modulus) and geomaterial-compactor interactions (contact width, contact stress) during compaction [9,10]. For example, Ghorbani et al. [11] used the advanced mortar-type contact algorithm to model a cylinder and geomaterial contact evolution and found that the contact width reduces with an increase in ρ_d. Because of this reduction in roller/material contact area during compaction, the contact stress increases as compaction progresses even though the load applied due to the compactor remains pretty much the same. The stresses applied by a cylindrical compactor can be evaluated approximately using Hertz's theory [12], which has been verified using field measurements [13,14]. However, calculating the stresses using the Hertzian approach requires knowledge of either Young's modulus or the contact width of the compacted material, both of which change during compaction. As these two parameters are difficult to measure or estimate during the compaction process, most detailed numerical modelling approaches assume the parameters are constant during the simulation, which limits the models' capability. For example, both [15] and [11] considered the modulus of the geomaterial to be constant during compaction. However, it has been demonstrated that the modulus depends on the ρ_d and increases as the ρ_d increases during compaction [16]. This study exploits a geometrical relationship between the plastic deformation during compaction and the associated contact width, and, thereby, presents a nonlinear relationship between the contact stress and the plastic deformation during compaction. The plastic deformation was selected as the independent variable as this can be measured relatively easily compared to contact width. For instance, it can be measured by using either contact or non-contact displacement sensors in the laboratory or in the field using scanning measurement systems and or advanced instrumentation [17–19]. This hypothesis allows the estimation of stresses needed for a constitutive (i.e., stress–strain) relationship using only the load applied, which is easier to determine during compaction.

The third issue related to compaction is the variation of initial density (ρ_{d0}) or initial void ratio (e_0). Because different techniques are used to place and spread the geomaterial, the initial placement ρ_{d0} or e_0 can vary, even for the same material with a particular moisture content. Due to the use of different machinery, the initially applied energy can be different, leading to different e_0. Hence, the void ratio evolution (change in void ratio during compaction) can be different even for the same applied load during roller compaction. This study also explores the effect of e_0 on void ratio evolution during simulated roller compaction.

Experimental evidence was used in this paper to develop a model to study stiffness, modulus, contact area, contact stresses and their evolution during compaction. The typical variation of these properties is reported, and their relationships with factors such as void ratio, number of cycles, and initial state are presented. Such information can be used in constitutive modelling instead of considering them to be constant during compaction.

On the basis of experiments undertaken on unbound granular materials (UGM), the model was validated and the issues noted above are addressed. The compaction was performed using a novel steel foot compactor simulating drum compaction in the field. The effects of the initial density, moisture and plasticity of fines on the compaction characteristics and model parameters were also studied.

Model development

Hertzian contact theory and geometrical relationship between contact width and plastic deformation

When a stationary cylindrical drum is in contact with geomaterial in loose condition, the contact width/area is higher than when the same roller is applied to a denser material as the indentation of the roller at the material's surface decreases with the increasing density [12]. Fig. 1 (a) and 1(b) illustrate the difference in the interaction between the roller and the material when the material is in the loose and dense states, respectively.

When the material is in a loose state, the contact width (B) is higher, and hence, under the same vertical load F, the stress is lower. The contact width keeps reducing with an increase in the number of cycles (or the number of rollers passes), and the contact stress increases during compaction even when the load (F) is constant. Constitutive relationships to model the compaction process require knowledge of the stresses. However, variable contact width and stresses during compaction make the modelling of the roller compaction process challenging.

For a cylinder contacting the elastic half media, the contact stress can be evaluated using Hertzian contact theory [12] as

$$\frac{1}{E^*} = \frac{1-\nu_1^2}{E_1} + \frac{1-\nu_2^2}{E_2} \tag{1}$$

$$\sigma^2 = \frac{E^* F}{\pi L R} \tag{2}$$

where, E^* is the equivalent modulus of the system, (E_1, ν_1) and (E_2, ν_2) are the Young's modulus and the Poisson's ratio of the geomaterial and the cylindrical compactor respectively. F is the load applied by the cylindrical compactor, whereas L is the length of the compactor, R is the radius of the compactor, and σ is the maximum contact stress. For this study, ν_1, E_2 and ν_2 were considered as a constant during compaction with the values of 0.35, 200 GPa and 0.2 respectively.

Using Equations (1) and (2), the contact stress can be estimated but

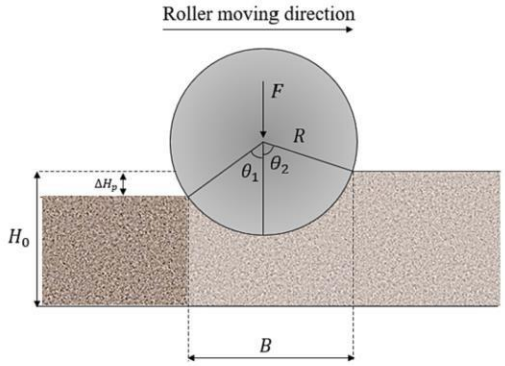

Fig. 2. Interaction between cylindrical compactor and geomaterial during compaction.

the knowledge of the modulus of the geomaterial is needed. Similar to the stresses and contact width, the modulus of the geomaterial also changes during compaction. Accordingly, the contact width (B) can be determined according to Hertzian theory [12] as

$$B = \sqrt{\left(\frac{16RF}{\pi E^* L}\right)} \tag{3}$$

From Equations (2) and (3), the peak contact stress can be written in terms of the contact width and the load applied such that

$$\sigma = \frac{4F}{\pi LB} \tag{4}$$

Fig. 1 depicts an idealised form of interaction between cylinder and geomaterial when the cylinder is stationary and the load is vertical. But in reality, the cylinder moves in a horizontal direction while applying the load vertically (Fig. 2). This study utilises the geometrical relationship between plastic deformation or compaction which is the difference between the front and back of the compactor (ΔH_p) and contact width (B) as shown.

From the above figure, the contact width can be written in terms of R and the internal angles (θ_1, θ_2) that it makes with the contact area with such that

$$B = R\big(sin(\theta_2) + sin(\theta_1)\big) \tag{5}$$

and the plastic deformation (ΔH_p) as

$$\Delta H_p = R\big(cos(\theta_1) - cos(\theta_2)\big) \tag{6}$$

Comparing the two variables using the trigonometric identities, contact width takes the form

$$B = 2Rsin\left(\frac{\theta_1 + \theta_2}{2}\right)cos\left(\frac{\theta_1 - \theta_2}{2}\right) \tag{7}$$

and the equation for plastic deformation (Equation (6)) is reduced to

$$\Delta H_p = 2Rsin\left(\frac{\theta_1 + \theta_2}{2}\right)sin\left(\frac{\theta_2 - \theta_1}{2}\right) \tag{8}$$

Equations (7) and (8) show that B and ΔH_p are related during a compaction cycle, i.e. $B \propto \Delta H_p$. Based on the experimental evidence of this study (shown later), it can be assumed that these two variables are related using a power function such that

$$B = \alpha \Delta H_p^{\beta} \tag{9}$$

where α and β are two additional constitutive parameters that depend on the geometric properties of the compactor.

Using Hertzian contact theory, the maximum stress due to a cylinder can be recast based on Equations (4) and (9) such that

$$\sigma = \frac{4F}{\pi L \alpha \Delta H_p^{\beta}} \tag{10}$$

It should be noted that when ΔH_p becomes zero the situation corresponds to the point loading problem. Because of the point load, the contact stress becomes infinite and a similar observation can be made when using the Boussinesq's equation to estimate the stresses due to point load. In the field, when compaction process becomes stationary at the end of the compaction, ΔH_p tends to go to zero at and in turn the contact stress becomes very high.

Modification of stress-based model to a load-based model

Sawicki et al. [7] developed a constitutive model in 1D compression, which was later progressed by Tophel et al. [8]. In this work, the cumulative plastic strain (ϵ_p) was considered to evolve logarithmically with the cycle number (N) subjected to a vertical stress (σ_z) such that

$$\epsilon_p = C_1 ln\left(1 + N\left(\frac{\sigma_z}{\sigma_{ref}}\right)^m\right), \tag{11}$$

where C_1 and m are model parameters and $\sigma_{ref} = 1$ kPa.

The above equation can then be differentiated to provide incremental plastic strain, i.e. ($\frac{d\epsilon_p}{dN}$ or $\Delta\epsilon_p$) yielding

$$\Delta\epsilon_p = C_1\left(\frac{\sigma_z}{\sigma_{ref}}\right)^m exp(-\frac{\epsilon_p}{C_1}) \tag{12}$$

Equation (12) is represented in terms of incremental plastic deformation (ΔH_p) and initial height (H_0) and cumulative plastic deformation (H_p) such that

$$\Delta H_p = H_0 C_1\left(\frac{\sigma_z}{\sigma_{ref}}\right)^m exp(-\frac{H_p}{H_0 C_1}) \tag{13}$$

As stated earlier, the load is commonly known during compaction, but not the stress. Therefore, Equation (13) is modified by adding the two constitutive parameters introduced in Equation (9) such that

$$\Delta H_p = H_0 C_1\left(\frac{4F}{\pi L \alpha \Delta H_p^{\beta}}\right)^m exp(-\frac{H_p}{H_0 C_1}) \tag{14}$$

The stress term is then replaced by the maximum stress applied by the cylindrical compactor during compaction. The maximum stress is taken as the shear failure responsible for the plastic deformation is due to the maximum stress. By rearranging,

$$\left(\Delta H_p\right)^{1+\beta m} = H_0 C_1\left(\frac{4F}{\pi L \alpha}\right)^m exp(-\frac{H_p}{H_0 C_1}) \tag{15}$$

Equation (15) can be integrated for either a constant or variable load condition.

If the applied load is not constant, integration of Equation (15) yields

$$H_p = H_0 C_1 (1 + \beta m) ln\left(1 + \frac{1}{1 + \beta m}\left(\frac{4}{\pi L \alpha}\right)^m \int_0^N F^m dN\right). \tag{16}$$

For a constant load, Equation (16) can be integrated to determine the cumulated material surface deformation

$$H_p = H_0 C_1 (1 + \beta m) ln\left(1 + \frac{1}{1 + \beta m}\left(\frac{4F}{\pi L \alpha}\right)^m N\right). \tag{17}$$

Assuming the material properties constant with depth in the compacted layer, the void ratio e_N at cycle, N can be calculated form the initial void ratio and height e_0 and H_0 respectively using the following equation approximately:

Table 1
Evolution of all the parameters (with N and e_N) during compaction.

Parameters		General Equation
Contact width (B)	N	$B = \alpha(H_0C_1)^{\frac{\beta}{1+\beta m}}\left(1+\frac{1}{1+\beta m}\left(\frac{4}{\pi L\alpha}\right)^m\int_0^N F^m dN\right)^{-\beta}$
	e_N	$B = \alpha(H_0C_1)^{\frac{\beta}{1+\beta m}}exp\left(-\frac{\beta}{C_1(1+\beta m)}\times\frac{(e_0-e_N)}{1+e_0}\right)$
Contact Stress (σ)	N	$\sigma = (H_0C_1)^{\frac{-\beta}{1+\beta m}}\left(1+\frac{1}{1+\beta m}\left(\frac{4}{\pi L\alpha}\right)^m\int_0^N F^m dN\right)^{\beta}$
	e_N	$\sigma = (H_0C_1)^{\frac{-\beta}{1+\beta m}}exp\left(\frac{\beta}{C_1(1+\beta m)}\times\frac{(e_0-e_N)}{1+e_0}\right)$
Modulus (E_1)	N	$E_1 = \frac{(H_0C_1)^{\frac{-2\beta}{1+\beta m}}\left(1+\frac{1}{1+\beta m}\left(\frac{4}{\pi L\alpha}\right)^m\int_0^N F^m dN\right)^{2\beta}\times\left(\frac{\pi LR}{F}\right)E_2(1-\nu_1^2)}{E_2-(H_0C_1)^{\frac{-2\beta}{1+\beta m}}\left(1+\frac{1}{1+\beta m}\left(\frac{4}{\pi L\alpha}\right)^m\int_0^N F^m dN\right)^{2\beta}\times\left(\frac{\pi LR}{F}\right)E_2(1-\nu_2^2)}$
	e_N	$E_1 = \frac{(H_0C_1)^{\frac{-2\beta}{1+\beta m}}exp\left(\frac{2\beta}{C_1(1+\beta m)}\times\frac{(e_0-e_N)}{1+e_0}\right)\times\left(\frac{\pi LR}{F}\right)E_2(1-\nu_1^2)}{E_2-(H_0C_1)^{\frac{-2\beta}{1+\beta m}}exp\left(\frac{2\beta}{C_1(1+\beta m)}\times\frac{(e_0-e_N)}{1+e_0}\right)\times\left(\frac{\pi LR}{F}\right)E_2(1-\nu_2^2)}$
Stiffness (K)	N	$K = (H_0C_1)^{\frac{-1}{1+\beta m}}\left(1+\frac{1}{1+\beta m}\left(\frac{4}{\pi L\alpha}\right)^m\int_0^N F^m dN\right)$
	e_N	$K = (H_0C_1)^{\frac{-1}{1+\beta m}}exp\left(\frac{\beta}{C_1(1+\beta m)}\times\frac{(e_0-e_N)}{1+e_0}\right)$

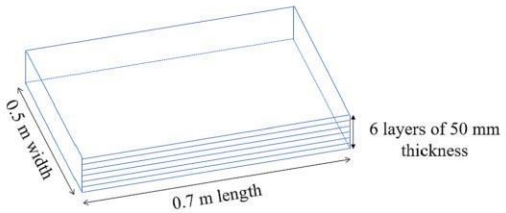

Fig. 3. Dimensions of the compaction mould.

$$\frac{e_0-e_N}{1+e_0}=\frac{H_p}{H_0} \tag{18}$$

Recalling the inverse relation between void ratio (e) and dry density (ρ_d) can be calculated as

$$\rho_d=\frac{G_s\gamma_w}{1+e} \tag{19}$$

where G_s is the specific gravity and γ_w is the unit weight of water.

The plastic stiffness (K) expresses the relationship between the vertical force (F) and the plastic deformation increment (ΔH_p) and is calculated as follows:

$$K=\frac{F}{\Delta H_p} \tag{20}$$

Similar to the plastic stiffness (K), modulus of the geomaterial represented by E_1, represents the plastic modulus of the geomaterial. Equation (16) can be used to derive all the material properties during compaction and is presented in Table 1.

Materials and Testing method

The experimental data comes from the laboratory compaction of slabs where multiple thin layers are compacted to gradually construct a 300 mm high full depth specimen [20] using the extra-large compactor

Fig. 4. Photo of the segmented roller and specimen during compaction.

and wheel tracker develop by ARRB for Austroads [21]. The materials used in this study were unbound granular materials (UGM) as they constitute the base layer of a flexible pavement and carries most of the load coming from the traffic.

Each sample was compacted in a mould of dimensions (length = 700 mm, width = 500 mm, and height = 300 mm) in six layers (Fig. 3). Each sample (300 mm thick) is compacted in 50 mm layers of 6 layers aiming at producing a uniform specimen with minimum density gradient with depth. In the field, density gradient will be observed with the spread of the compaction load with depth. The compaction in sublayers was developed to allow reducing density gradient even when compacting material below optimum compaction moisture in order to avoid generation of high compaction effort and prevent potential particle breakage during the compaction process when testing weak or marginal fit-for-purpose materials.The material was first homogenised using a rotary splitter and dried at a low temperature (80 °C). Before compaction,

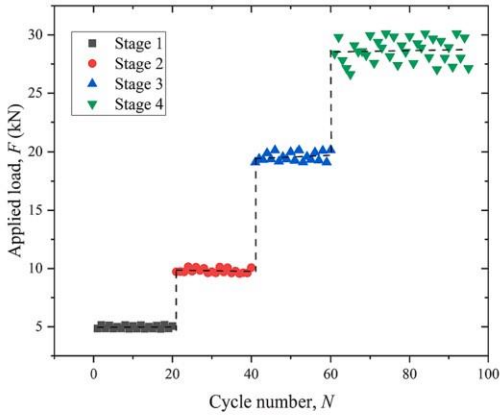

Fig. 5. Loading cycle details for one of the samples.

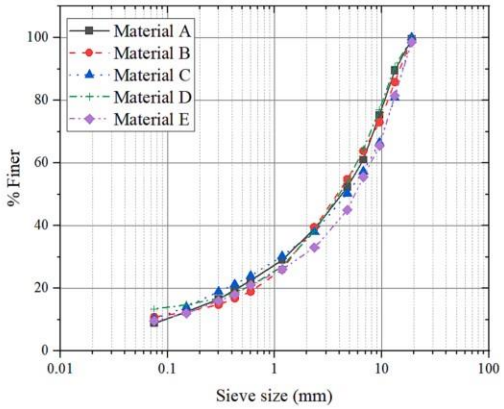

Fig. 6. Grain size distribution (GSD) of all the materials used in this study.

water was added to the dry aggregates to achieve the desired moisture content. Mixing with the appropriate mass of water was performed using an 80-litre concrete mixer. The material was then stored and sealed before compaction.

Based on the targeted density (void ratio) and moisture content, the wet mass required was calculated and the material was spread in the mould. Special care was taken to avoid segregation while spreading. The material was first spread and compacted using a hand-held tamping device to ensure even distribution. The material was then pre-compacted with a load of about 1 kN. The compaction effort or load applied on the steel compaction foot (Fig. 4) was loaded at 5 kN and gradually increased with the measured height for density estimation at the centre of the specimen recorded. by a Linear Variable Differential Transformer (LVDT) displacement sensor. The LVDT is attached between the machine frame and the bottom of the mould. The compaction effort is applied on the specimen mould from underneath pushing the specimen and the material to be compacted towards the compaction foot. Change in displacement results from the thickness reduction of the material in the mould. This interpretation assumes that the deflection of the machine frame and compaction foot is negligible compared to the height variation when compacting the granular material due to significant modulus difference between the steel and the soil. During the compaction of the layer i it is assumed that no further compaction is experienced in the underlying layer i-1 and below, which are already compacted at the target density. The change of relative position of the bottom of the mould / compaction foot radius is interpreted as the change in height of layer i. The single measurement of the height in the middle of the slab was used as a measurement of the density. As during the development of the test method the uniformity of the density achieved in the compacted resulting from the compaction procedure (AGPT/T054) was assessed and demonstrated (except edge effects inherent to compaction of granular materials) as described in ([21]). An example of one loading scenario is shown in Fig. 5. The loading was started at 5 kN (stage 1) until a maximum of 20 cycles and increased to 10 kN (stage 2) for a maximum of 20 cycles if the desired height was not achieved. The loading is further increased to 20 kN (stage 3) and then 30 kN (stage 4) for a maximum of 20 cycles each until the compaction is achieved. Core samples at the end were obtained to verify the density calculated using the height measurement.

Testing Program

The test matrix included 14 samples comprising five different materials and was given different ARRB sample register numbers 2510, 2511, 2512, 2513 and 3850, referred to here simply as materials A, B, C, D, and E, respectively. The details of the materials are given in Table 2 with the grain size distributions shown in Fig. 6.

Materials A and B were sourced from a quarry in Lysterfield, Victoria, Australia and a quarry in Tynong, Victoria, Australia, respectively. Materials C, D, and E were prepared in the lab to study the effect of plasticity. Material C had 6% Claypro (a clay additive) added to material A while material D had 30% Class 4 subbase material (VicRoads classification [22]) added. Material E was planned to be prepared similar to material C, but because of the incorporation of scalping materials to improve the grading, the material became more plastic due to the

Table 2
Results of the basic characterisation tests on each material.

Material	Granite standard plasticity	Hornfels standard plasticity	Granite increased plasticity	Hornfels increased plasticity	Granite increased plasticity+	Test Standard
Material Number	**2510 (A)**	**2511 (B)**	**2512 (C)**	**2513 (D)**	**3850 (E)**	
%fines (less than 0.075 mm)	8.8	10.8	10.3	13.4	9.6	[23]
%sand (4.75 mm −0.075 mm)	43.5	44	40	40.6	35.4	[23]
%gravel (>4.75 mm)	47.7	45.2	49.7	46	55	[23]
Plastic Limit (PL) (%)	26	23	23	28	28	[24]
Liquid Limit (LL) (%)	19	19	14	20	14	[25]
Plasticity Index (PI) (%)	7	4	9	9	14	[26]
Specific Gravity (G_s)	2.66	2.74	2.79	2.74	2.66	[27]
Optimum Moisture Content (OMC), modified Proctor (%)	6.6	5.6	5.5	6.6	5.9	[28]
Maximum Dry Density (MDD), modified Proctor (kg/m^3)	2200	2300	2290	2230	2270	[28]

Table 3
Test matrix used for this study.

Sample ID	Mat. No.	MC (%)
1	A	3.61
2	A	4.32
3	A	4.93
4	A	4.13
5	B	4.02
6	B	4.05
7	B	4.9
8	C	4.07
9	C	4.82
10	C	5.11
11	D	3.94
12	D	5.67
13	E	4.13
14	E	4.9

inclusion of plastic fines.

Different samples of each material were prepared and tested to study the effect of moisture content. Table 3 shows the test matrix of all the samples with the moisture content (MC) used for preparation.

As previously stated, each sample was compacted in six layers, with the manual tamping during sample preparation creating different e_0 for each layer before the actual compaction began. However, these layers were compacted to approximately the same final void ratio (e_{final}). Fig. 7 shows that because of the different e_0, each sample experienced a different number of cycles (N) to reach e_{final}. The initial void ratio and the final/target void ratio matrix for all the samples is shown in Table 4.

Results and discussions:

Prediction ability of the developed model

The prediction model skill was assessed using two metrics, coefficient of correlation (R^2) and mean absolute error (MAE) defined as.

$$\mathrm{MAE} = \frac{1}{len(Y)}\sum_{i=1}^{len(Y)} \left|Y - Y_{pred}\right| \tag{21}$$

$$R^2 = 1 - \frac{\sum_{i=1}^{len(Y)} \left(Y - Y_{pred}\right)^2}{\sum_{i=1}^{len(Y)} \left(Y - \overline{Y}\right)^2} \tag{22}$$

where Y is the experimental observation, Y_{pred} is the predicted output from the model, $\overline{Y}$ is the mean value of all the values of Y, and $len(Y)$

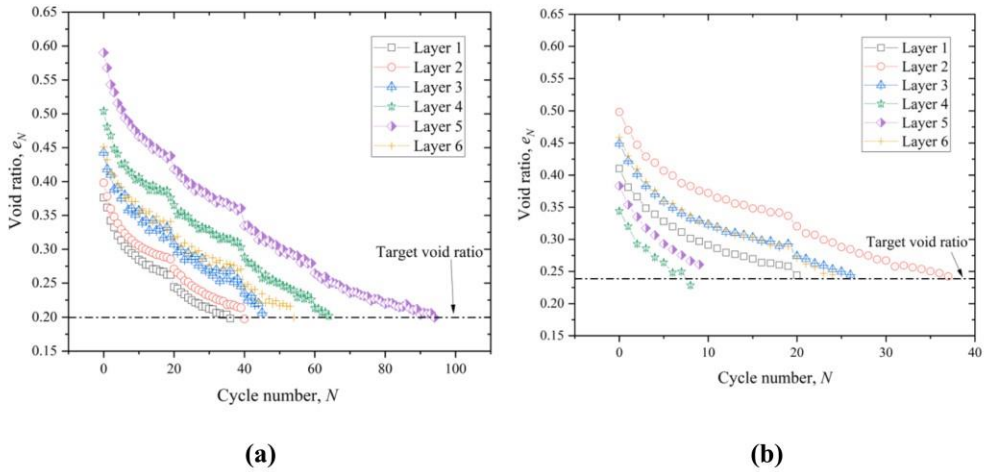

Fig. 7. Void ratio evolution during compaction for each layer for: (a) sample 4, (b) sample 13.

Table 4
The e_0 matrix and e_{final} for all the samples tested.

Sample ID	Initial Void ratio (e_0)						Final void ratio (e_{final})
	Layer 1	Layer 2	Layer 3	Layer 4	Layer 5	Layer 6	
1	0.314	0.516	0.462	0.436	0.490	0.461	0.227 ± 0.007
2	0.394	0.457	0.446	0.471	0.471	0.474	0.227 ± 0.006
3	0.389	0.504	0.418	0.484	0.460	0.505	0.228 ± 0.005
4	0.376	0.398	0.443	0.504	0.590	0.451	0.201 ± 0.003
5	0.399	0.464	0.426	0.439	0.444	0.481	0.227 ± 0.003
6	0.416	0.440	0.434	0.498	0.417	0.605	0.226 ± 0.005
7	0.335	0.434	0.422	0.415	0.457	0.373	0.223 ± 0.007
8	0.452	0.537	0.451	0.457	0.500	0.519	0.225 ± 0.006
9	0.424	0.448	0.473	0.472	0.446	0.540	0.226 ± 0.012
10	0.395	0.443	0.499	0.484	0.463	0.447	0.228 ± 0.002
11	0.427	0.412	0.503	0.543	0.529	0.476	0.240 ± 0.009
12	0.409	0.441	0.441	0.429	0.495	0.485	0.242 ± 0.009
13	0.410	0.498	0.449	0.344	0.383	0.459	0.244 ± 0.010
14	0.370	0.443	0.375	0.400	0.379	0.419	0.228 ± 0.004

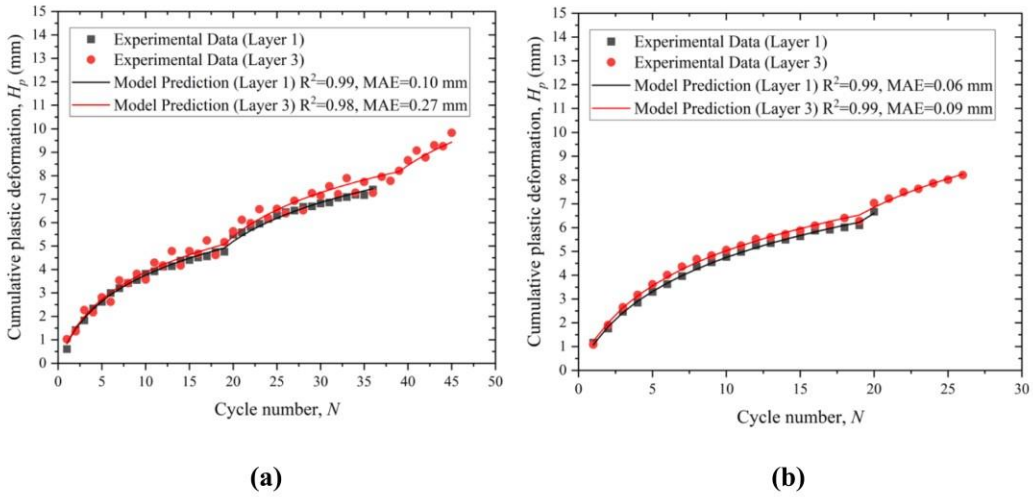

Fig. 8. Prediction ability of the developed model for two layers each for (a) sample 4 and (b) sample 13.

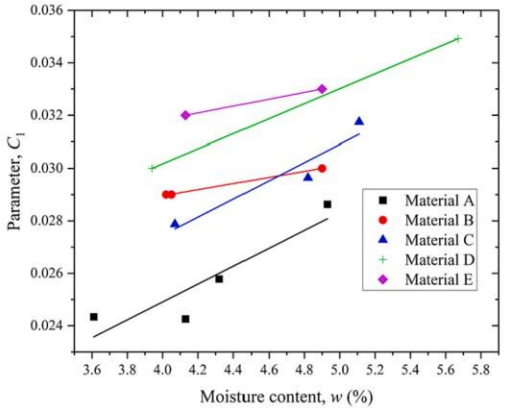

Fig. 9. Variation of model parameter C_1 with moisture content (w).

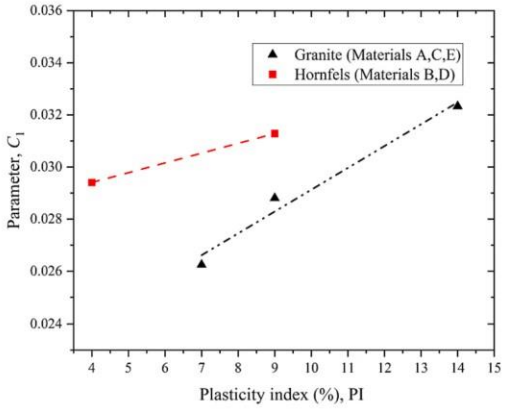

Fig. 10. Effect of plasticity on model parameter C_1 at moisture content 4.4%.

represents the number of values of Y.

Fig. 8 shows the model prediction ability for two examples (Sample 4 and Sample 13) for two layers (layer 1 and layer 3). Both figures illustrate that the model was an excellent predictor for the observed data even when the load increment was required (cycle number 20 and cycle number 40 for sample 4 and cycle 20 for sample 13). Only four examples are shown for clarity, but the proposed model showed excellent prediction skill for the entire dataset with R^2 >0.98 and MAE of less than 0.3 mm.

Constitutive Parameter estimation

The two new constitutive parameters α and β were estimated as 15 mm and 0.25 respectively for all the materials, for the given compactor evaluated using the least square method. Parameters C_1 and m were also evaluated using the least square method. The parameter C_1 was found to be the same for a given material, independent of the initial density of the sample. However, C_1 was a function of sample moisture content (Fig. 9) which was also reported in the authors' previous work for constant stress 1D compaction tests [8].

According to Equation (15), the value of C_1 is directly proportional to the strain accumulated for a given stress. Fig. 9 indicates that the value increases with an increase in moisture content. This is in line with the Proctor compaction theory, stating that the compaction (i.e. height reduction) is easier when the moisture is higher (note that all the compaction moisture content were lower than OMC obtained from the modified Proctor test) [29,30]. As all the tests were performed dry of optimum and, therefore, conclusions regarding wet of optimum are not made in this article. The authors however believe that conclusions made in previous studies (e.g., ([29,31])) that the compaction is difficult with an increase in the water content when compacted wetter than the optimum is valid for this study as well.

Fig. 9 also highlights that the for the materials used, higher the plasticity index, the better the compaction for the materials used as

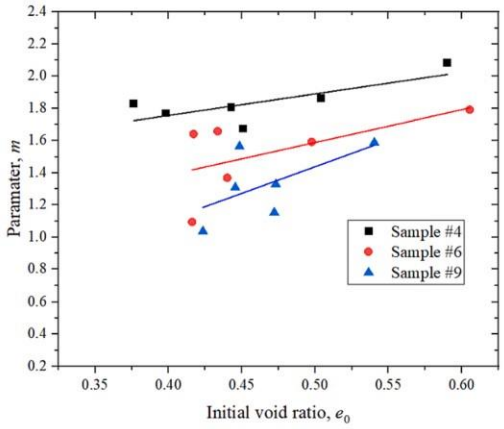

Fig. 11. Variation of model parameter m with initial void ratio (e_0).

reflected by the corresponding values of C_1. For a better illustration, Fig. 10 is plotted which shows the variation of model parameter C_1 for different materials at one moisture content (4.4%). The variation confirms that as the plasticity index increase value of model parameter C_1 increases.

The model parameter m was found to be linearly dependent on initial density (e_0), as observed in Fig. 11 for the three example samples. The values of m on the entire dataset are in Table 5. The linear dependency between m and e_0 was also reported in the authors' previous work [8], where samples tested under 1D compaction had the model parameter strongly related to the initial density. The relationship between parameter m and e_0 was also evaluated when m was considered independent of e_0 as shown in the last column of Table 5. When m was considered independent of e_0 the prediction error of the model increased, but this needs to be balanced with the need for parameter reduction, especially for real-time applications of the developed model.

Evolution of contact width, stress and stiffness parameters during compaction

In order to demonstrate the parameter evolution with cyclic compaction, contact width (B), contact stress (σ), modulus (E_1), and stiffness (K) due to the dynamic loading, interactions between the roller and geomaterial were calculated and plotted for sample 4, layers 1 and 5 below. These particular sample and layers were chosen to contrast the material properties as they needed 36 and 94 cycles to reach the final void ratio (e_{final}). Only two stages were applied for layer 1 while all stages of loading were applied for the layer 5, facilitating a better illustration of the parameter evolution. The two independent parameters e_N and the cycle number N were chosen because it is easier to track or measure them in the lab and field. Fig. 12 shows the geomaterial property variation with e_N in the multi-stage loading. The x-axis in all subfigures is plotted in the reverse order as it decreases during compaction for easy visualisation. The parameters σ, E_1, and K increased during compaction as the material gets stiffer, therefore, having an inverse relationship with the e_N, which reduces with compaction.

Conversely, the contact width (B) reduced during compaction giving rise to an increase in the contact stress (σ) and therefore had a positive relationship with e_N. It can be observed that on each occasion the applied load was increased (as the loading stage is changed), the parameters E_1, B, and σ increased and K reduced.

Fig. 13 shows the variation of parameters with the numbers of cycles of compaction. Since e_N and N are inversely related, the variations of all parameters with e_N and N are opposite.

Due to the difference in the loading history, the modulus at the final void ratio is different and is higher for the sample that had a higher initial void ratio. The observation could be attributed to the difference in the load (10 kN for layer 1 and 30 kN for layer 5) at the final loading stage. At the final compaction cycle, the contact width was around 7 mm for layer 5, which was lower when compared to layer 1 where the contact width was 8.2 mm. The other material properties (modulus, stress and stiffness) were higher for layer 5 compared to layer 1. This could be because the final load applied was higher for layer 5. The other possible reason could be the complex non-linear mulit-dimensional interaction of contact mechanics between the compactor and the material, which needs further investigation.

Table 6 presents simplified relationships for all the parameters including when the applied load (F) is constant with e_N and N. C_0 to C_{10} in the table are model parameters. For example, all the parameters can be expressed as an exponential function of e_N. Conversely, variation of all parameters can be expressed as a power function of N except for K, which can be expressed as a linear function of N. These equations can be used directly to calibrate the model parameters if a similar test setup involving a roller is used, either in the field or in the lab. And also can be used for finite element modelling etc., and their variation/evolution with e_N and N can be used instead of considering them constant during compaction.

Total energy imparted to the sample to achieve the target density

The cumulative energy required to achieve the target density is an important parameter for the optimal construction of pavement layers. It dictates the number of passes required to achieve the desired

Table 5
Value of parameter m obtained for all 14 samples having six layers.

Sample ID	Layer 1	Layer 2	Layer 3	Layer 4	Layer 5	Layer 6	Void ratio independent*
1	2.09	1.96	2.07	1.91	2.02	1.78	1.92
2	1.72	1.69	1.80	1.66	1.76	1.56	1.67
3	0.93	1.82	1.65	1.77	1.58	1.50	1.65
4	1.83	1.77	1.81	1.86	2.08	1.67	1.98
5	0.97	1.29	2.07	1.35	1.39	1.30	1.34
6	1.09	1.37	1.66	1.59	1.64	1.79	1.70
7	0.44	2.23	1.94	2.25	1.86	1.39	1.94
8	1.75	1.60	1.40	1.37	1.59	1.50	1.55
9	1.04	1.56	1.33	1.15	1.31	1.59	1.37
10	1.26	1.61	1.41	1.24	1.95	2.22	1.46
11	0.82	0.97	1.18	1.24	1.01	0.71	1.10
12	1.25	1.80	1.56	1.46	1.98	1.41	1.63
13	1.85	1.74	1.81	2.12	1.81	2.35	1.81
14	0.62	2.06	2.05	1.63	1.18	1.74	1.90

* Considering the entire dataset for a sample.

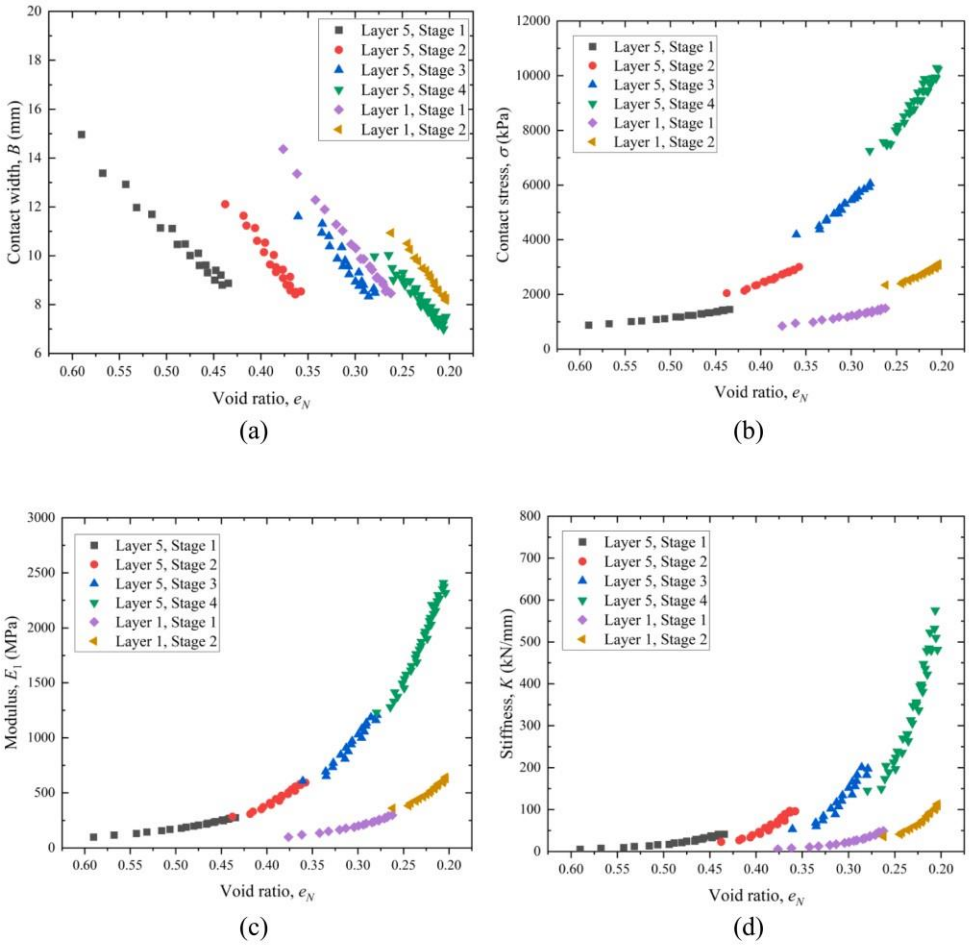

Fig. 12. Variation of parameters: (a) B, (b) σ, (c) E_1, (d) K with e_N during compaction.

specifications of the geomaterials. The optimal use of energy is also important for sustainable construction where energy utilization is optimised. In addition, compacting the material more than required can cause over-compaction, allowing the material to heave, with multiple shear planes and chaotic motions of the roller leading to breakdown and wear and tear of the rollers [32,33]. Over-compaction can also lead to excessive plastic deformation or rutting during the traffic loading in its service life [34–36].

The total energy applied per unit volume (ξ_{app}) to reach the final density or void ratio was calculated using the following equation as:

$$\xi_{app} = \frac{\sum_0^N F \times \Delta H_p}{H_0 \times B \times L} \tag{23}$$

The energy applied, ξ_{app}, to reach the target density (MDD for this study) was compared to the energy applied in the standard and modified Proctor tests. It was found that all samples needed less energy than the modified Proctor (2703 kJ/m^3 [36]). This was because the material was provided energy during manual tamping and spreading and therefore did not start from its loosest state. The manual tamping and spreading may to some extent replicate the paver spreading in the field; therefore, careful consideration of the number of delivered passes by the compactor should be considered. Fig. 14 illustrates the variation of ξ_{app} with e_0 for six samples (three samples for each of material B and material C). Two observations can be made; first, ξ_{app} is directly proportional to e_0; second, ξ_{app} is lower for higher moisture contents (increasing order of moisture content is sample 8, sample 9 and sample 10) at the same e_0, confirming the observation made in Fig. 9. The graph cannot be directly used for field compaction control using bigger rollers as the energy transfer mechanism, and energy losses are different in the two settings. To use the developed graph for field compaction control, a similar graph should be developed in the field for a particular compaction machine by measuring the thickness change using external devices such as a total station scanner and laser scanners.

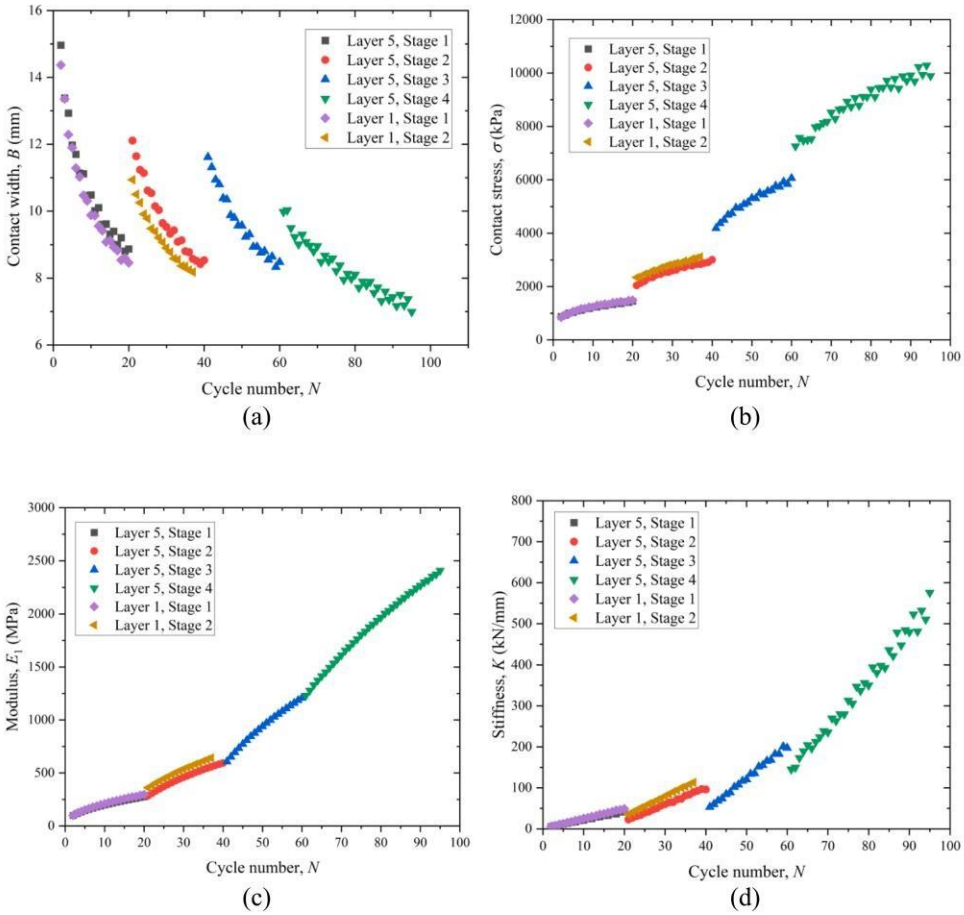

Fig. 13. Variation of parameters: (a) B, (b) σ, (c) E_1, (d) K with N during compaction.

Conclusions and implications of this study

Construction of any civil engineering structure requires earthwork activities, including embankment construction for dams and bridges. The geomaterials used are compacted using rollers to attain the properties required. To understand and optimise the compaction process, it is very important to understand the compaction process through modelling, and small-scale experiments in the lab, as repeating field-scale experiments requires a big investment. This study addressed the following major issues related to understanding the compaction process by testing UGMs in a simulated wheel tracking apparatus at different initial conditions (plasticity, moisture content (w) and initial void ratio (e_0)). They are as follows:

(a) Roller compaction modelling has been a challenge throughout. One reason is that the stress acting on the material properties are not constant during compaction. As the material gets stiffer during compaction, the contact area or width (B) between the drum and the geomaterial gradually reduces. Generally, the applied load (F) during compaction is constant; and the contact stress (σ) increases due to reduction of B. This is entirely different from tests usually carried out in a laboratory, where the stress is kept constant. Hence, the model developed from the constant stress test cannot be used to model the variable stress compaction process. This study extended a constant stress model to a constant load model using the geometrical relationship between B and incremental plastic deformation (ΔH_p). The excellent predictability of the simplified model shows that the complex compaction can be reasonably approximated using a simple 1D equation. The proposed model eliminates the requirement of a complex model, which hinders a real-time application as the computational time is high.

(b) Equations are presented where the dynamic parameters vary with the void ratio and the number of cycles. Simplified equations are also presented, which can be used by Finite element research instead of considering the stress or contact width as a constant.

(c) The effect of moisture content and plasticity was highlighted in various parts of this article, showing that moisture aids in

Table 6
Simplified equations for all the parameters for special case.

Parameter	Constant Load	Simplified equation with cycle No.	Simplified equation with void ratio
Contact width (B)	$B = \alpha(H_0C_1)^{\frac{\beta}{1+\beta m}}\left(1+\frac{1}{1+\beta m}\left(\frac{4F}{\pi L\alpha}\right)^m N\right)^{-\beta}$	$B = C_2{C_0}^{C_3}(1+C_4F^mN)^{-C_{10}}$	$B = C_2{C_0}^{C_3}exp(C_5\times(C_6-e_N))$
Contact Stress (σ)	$\sigma = (H_0C_1)^{\frac{-\beta}{1+\beta m}}\left(1+\frac{1}{1+\beta m}\left(\frac{4F}{\pi L\alpha}\right)^m N\right)^{\beta}$	$\sigma = {C_0}^{-C_3}(1+C_4F^mN)^{C_{10}}$	$\sigma = {C_0}^{-C_3}exp(-C_5\times(C_6-e_N))$
Modulus (E_1)	$E_1 = \frac{(H_0C_1)^{\frac{-2\beta}{1+\beta m}}\left(1+\frac{1}{1+\beta m}\left(\frac{4F}{\pi L\alpha}\right)^m N\right)^{2\beta}\times\left(\frac{\pi LR}{F}\right)E_2(1-\nu_1^2)}{E_2-(H_0C_1)^{\frac{-2\beta}{1+\beta m}}\left(1+\frac{1}{1+\beta m}\left(\frac{4F}{\pi L\alpha}\right)^m N\right)^{2\beta}\times\left(\frac{\pi LR}{F}\right)E_2(1-\nu_2^2)}$	$E_1 = \frac{C_8{C_0}^{-2C_3}(1+C_4F^mN)^{2C_{10}}}{FE_2-C_7{C_0}^{-2C_3}(1+C_4F^mN)^{2C_{10}}}$	$E_1 = \frac{C_8{C_0}^{-2C_3}exp(-2C_5\times(C_6-e_N))}{FE_2-C_7{C_0}^{-2C_3}exp(-2C_5\times(C_6-e_N))}$
Stiffness (K)	$K = (H_0C_1)^{\frac{-1}{1+\beta m}}\left(1+\frac{1}{1+\beta m}\left(\frac{4F}{\pi L\alpha}\right)^m N\right)$	$K = {C_0}^{C_9}(1+C_4F^mN)$	$K = {C_0}^{C_9}exp(-C_5\times(C_6-e_N))$

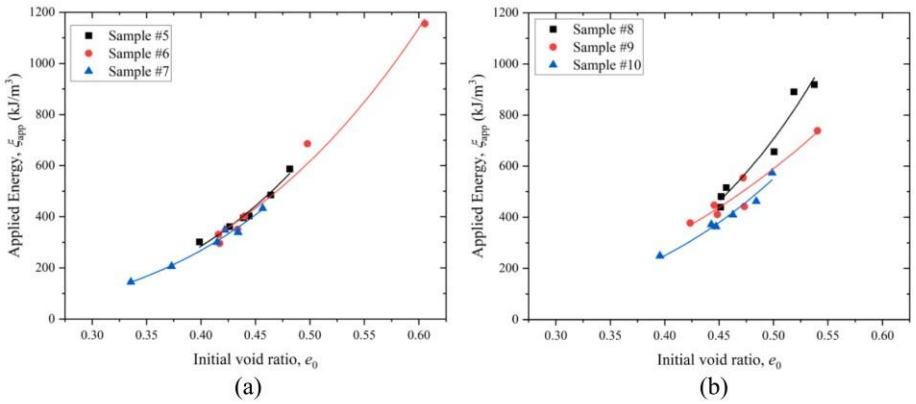

Fig. 14. Variation of total energy applied with e_N for: (a) material B, (b) material C.

compaction. This is in line with the Proctor compaction theory, as the moisture content used was less than optimal. Model parameter C_1 was higher for sample with higher moisture content and higher plasticity of fines.

(d) This study also highlights the effect of the initial void ratio on the parameters of the geomaterial during compaction. The different initial void ratios in the field can arise because of different spreading or paving techniques. The study of model parameters and their dependence on the initial void ratio is highlighted. The initial void ratio dependency is also important as it allows to study of the energy required to achieve a certain degree of compaction. This would ensure the sustainable use of compaction energy.

(e) Although the model was developed for static load using a drum compactor, the authors hypothesize that the concepts developed can be extended for vibratory drum compaction possibly by scaling the static load with the dynamic load applied by vibratory rollers. The information about vibratory compactors' eccentric mass is known, allowing the vibratory load estimation. The load term in the original model's equation representing the static load can be replaced with the combined dynamic load (static and vibratory load).

Funding.

This study was supported by the Australian Research Council (ARC) Industrial Transformation Research Hub (ITRH) Scheme (Grant No IH180100010). This project was also funded by Austroads through project TT1611 and TT1819.

Availability of data and material: Not applicable.

Code availability: Not applicable.

CRediT authorship contribution statement

Amir Tophel: Conceptualization, Methodology, Software, Formal analysis, Writing – original draft, Visualization. **Jeffrey P. Walker:** Resources, Writing – review & editing, Supervision, Project administration. **Troyee Tanu Dutta:** Writing – review & editing, Visualization, Supervision. **Didier Bodin:** Methodology, Investigation, Resources, Data curation, Writing – review & editing, Supervision, Project administration. **Jayantha Kodikara:** Conceptualization, Methodology, Resources, Writing – review & editing, Supervision, Project administration, Funding acquisition.

Declaration of Competing Interest

The authors declare that they have no known competing financial interests or personal relationships that could have appeared to influence the work reported in this paper.

Data availability

Data will be made available on request.

Acknowledgments

The first author received a Monash University Graduate Scholarship (MGS) to undertake this research project. This research work was also part of a research project (Project No IH18.03.3) sponsored by the SPARC Hub (https://sparchub.org.au) at the Department of Civil Engineering, Monash University, funded by the Australian Research Council (ARC) Industrial Transformation Research Hub (ITRH) Scheme (Project ID: IH180100010). The authors would like to acknowledge the Australian Road Research Board (ARRB) for providing the experimental data, and technical as well as in-kind support. The authors would also like to acknowledge Austroads for funding project TT1611 and TT1819. The authors gratefully acknowledge the financial and in-kind support of Monash University, SPARC Hub, CIMIC, and EIC activities.

References

[1] Chong SH, Santamarina JC. Sands subjected to repetitive vertical loading under zero lateral strain: accumulation models, terminal densities, and settlement. Can Geotech J 2016;53:2039–46. https://doi.org/10.1139/cgj-2016-0032.
[2] Park J, Santamarina JC. Sand response to a large number of loading cycles under zero-lateral-strain conditions: evolution of void ratio and small-strain stiffness. Geotechnique 2019;69:501–13. https://doi.org/10.1680/jgeot.17.P.124.
[3] Pasten C, Shin H, Santamarina JC. Long-term foundation response to repetitive loading. J Geotech Geoenviron Eng 2014;140:1–11. https://doi.org/10.1061/(ASCE)GT.1943-5606.0001052.
[4] Wichtmann T. Explicit accumulation model for non-cohesive soils under cyclic loading. Inst für Grundbau und Bodenmechanik Phd:274; 2005. PhD Thesis.
[5] Modoni G, Koseki J, Anh Dan LQ. Cyclic stress-strain response of compacted gravel. Geotechnique 2011;61:473–85. https://doi.org/10.1680/geot.7.00150.
[6] Pestana JM, Whittle AJ, Salvati LA. Evaluation of a constitutive model for clays and sands: Part I - sand behaviour. Int J Numer Anal Methods Geomech 2002;26:1097–121. https://doi.org/10.1002/nag.237.
[7] Sawicki A, Swidzinski W. Cyclic compaction of soils, grains and powders. Powder Technol 1995;85:97–104. https://doi.org/10.1016/0032-5910(95)03013-Y.
[8] Tophel A, Walker JP, Dutta TT, Kodikara J. Theory-guided machine learning to predict density evolution of sand dynamically compacted under Ko condition. Acta Geotech 2022. https://doi.org/10.1007/s11440-021-01431-2.
[9] Hager M, Pistrol J, Kopf F, Adam D. Verdichtung mit Vibrationswalzen. Bauingenieur: Semi-analytische Modellierung des Interaktionssystems Bandage-Boden mit Berücksichtigung der veränderlichen Bandagenaufstandsbreite; 2021. p. 96.
[10] G, Kargl Modellversuche zur Ermittlung des Last-Deformationsverhaltens geschichteter Modellböden unter ebenen und zylindrisch gekrümmten Belastungsflächen und vergleichende Computerberechnungen. TU Wien 1995.
[11] Ghorbani J, Nazem M, Kodikara J, Wriggers P. Finite element solution for static and dynamic interactions of cylindrical rigid objects and unsaturated granular soils. Comput Methods Appl Mech Eng 2021;384:113974. https://doi.org/10.1016/j.cma.2021.113974.
[12] Hertz H. Über die Berührung fester elasticscher Körper (On the contact of elastic body). Leipzig: Gesammelte Werke; 1895.
[13] B, Caicedo Geotechnics of Roads: Fundamentals. CRC Press, Taylor & Francis Group 2019.
[14] Rinehart RV, Mooney MA. Measurement of roller compactor induced triaxial soil stresses and strains. Geotech Test J 2009;32:347–57. https://doi.org/10.1520/gtj101889.
[15] Kenneally B, Musimbi OM, Wang J, Mooney MA. Finite element analysis of vibratory roller response on layered soil systems. Comput Geotech 2015;67:73–82. https://doi.org/10.1016/j.compgeo.2015.02.015.
[16] Tatsuoka F, Hashimoto T, Tateyama K. Soil stiffness as a function of dry density and the degree of saturation for compaction control. Soils Found 2021;61:989–1002. https://doi.org/10.1016/j.sandf.2021.06.007.
[17] Tophel A, Kodikara J, Walker JP. Systems and methods for measuring/estimating geomaterial layer properties due to compaction. Patent Cooperation Treaty (PCT) 2021. AU2021/051505.
[18] Tophel A, Walker J, Lu Y, Kodikara J. Proximal sensing of density during soil compaction by instrumented roller. Aust Geomech J 2022;57:161–9. https://doi.org/10.56295/AGJ5739.
[19] A, Tophel, JP, Walker, TT, Dutta, J, Kodikara Using a Novel Instrumented Roller to Estimate Soil Dry Density During Compaction. In: Gomes Correia A, Azenha M, Cruz PJS, et al (eds) Trends on Construction in the Digital Era. ISIC 2022. Lecture Notes in Civil Engineering, vol 306. Springer, Cham 2023, pp 538–546.
[20] Bodin D. Improved laboratory characterisation of the deformation properties of granular materials. Austroads Publ AP-T324-17 2017.
[21] D, Bodin, M, Moffatt, G, Jameson Development of a Wheel-tracking Test for Rut Resistance Characterisation of Unbound Granular Materials. Austroads Publ AP-T240-13 2013.
[22] VicRoads (2016) Crushed Rock for Pavement Base and Subbase. http://webapps.vicroads.vic.gov.au/VRNE/csdspeci.nsf/webscdocs/A633FC705037997BCA257FEF0003DBF6?OpenDocument. Accessed 2 Jul 2022.
[23] Standards Australia (2009) Soil classification tests- Determination of the particle size distribution of a soil—Standard method of analysis by sieving. AS 1289361.
[24] Standards Australia (2009) Soil classification tests - Determination of the plastic limit of a soil - Standard method. AS 1289321.
[25] Standards Australia (2009) Soil classification tests - Determination of the liquid limit of a soil - One point Casagrande method (subsidiary method). AS 1289312.
[26] Standards Australia (2009) Soil classification tests - Calculation of the plasticity index of a soil. AS 1289331.
[27] Standards Australia (2002) Soil classification tests— Determination of the soil particle density of combined soil fractions—Vacuum pycnometer method. AS 1289352.
[28] Australia S. Soil compaction and density tests — Determination of the dry density / moisture content relation of a soil using modified compactive effort. AS 2003;1289521:1–13.
[29] Kodikara J. New framework for volumetric constitutive behaviour of compacted unsaturated soils. Can Geotech J 2012;49:1227–43. https://doi.org/10.1139/t2012-084.
[30] Kodikara J, Islam T, Sounthararajah A. Review of soil compaction: History and recent developments. Transp Geotech 2018;17:24–34. https://doi.org/10.1016/j.trgeo.2018.09.006.
[31] Tatsuoka F, Gomes Correia A. Importance of controlling the degree of saturation in soil compaction linked to soil structure design. Transp Geotech 2018;17:3–23. https://doi.org/10.1016/j.trgeo.2018.06.004.
[32] Liu D, Wang Y, Chen J, Zhang Y. Intelligent compaction practice and development: a bibliometric analysis. Eng Constr Archit Manag 2019;27:1213–32. https://doi.org/10.1108/ECAM-05-2019-0252.
[33] Anderegg R, Kaufmann K. Intelligent compaction with vibratory rollers: feedback control systems in automatic compaction and compaction control. Transp Res Rec J Transp Res Board 2004;1868:124–34. https://doi.org/10.3141/1868-13.
[34] Monismith CL, Ogawa N, Freeme CR. Permanent deformation characteristics of subgrade soils due to repeated loading. Transp Res Rec 1975;537.
[35] Brown SF, Hyde AFL. Significance of cyclic confining stress in repeated-load triaxial testing of granular material. Transp Res Rec 1975;537. https://doi.org/10.1016/0148-9062(76)90013-9.
[36] Lekarp F, Dawson A. Modelling permanent deformation behaviour of unbound granular materials. Constr Build Mater 1998. https://doi.org/10.1016/S0950-0618(97)00078-0.

The developed model in this chapter also sheds light into the effect of initial state on other QA measurement (modulus) and density relationship of geomaterials which is discussed in the next section.

5.2 Errata and Addenda for the published paper (Tophel et al. 2023)

5.2.1 Errata

Erratum 1: In Table 2, the liquid limit and plastic limit are placed back to front.

Correction: In Table 2, the liquid limit and plastic limit should be interchanged.

Erratum 2: Figure 14, caption of the figure e_N is inconsistent with the use of x-axis title e_0.

Correction: The caption of the figure should be corrected to: variation of total energy applied with e_0 for (a) material B, (b) material C.

Erratum 3: In page 4 of the paper, E_1 is mentioned as plastic modulus. The original sentence was: "Similar to plastic stiffness (K), modulus of the geomaterial represented by E_1, represents the plastic modulus of the geomaterial."

Correction: E_1 should be elastic modulus. The sentence should be changed to "The plastic stiffness is represented by K, whereas, the Youngs' or elastic modulus of the geomaterial is represented by E_1."

5.3 Influence of initial state on modulus-density relationship

Pavement construction and compaction quality control commonly rely on density measurements. However, modulus measurement methods are gaining popularity due to their convenience and ease of use compared to density measurement techniques. Modulus-based methods can provide the material modulus needed for a pavement layers' mechanistic-empirical (ME) design. However, these methods have not been widely accepted as a replacement for density measurement in current quality control practices because a single modulus measurement does not correspond to a specific density measurement (Meehan et al. 2012; Lee et al. 2017; Wang et al. 2022). The modulus of geomaterials is typically considered independent of its stress history, depending primarily on moisture content, density, or void ratio. This section of the chapter examines the non-unique relationship between modulus and density in the field, even at constant moisture content, using three test setups to study

geomaterial behaviour under cyclic loading. Accurately estimating the modulus requires knowledge of the geomaterial's initial and current states regardless of the measured modulus or test type. Variations in initial density, resulting from different paving or spreading methods, can lead to different residual lateral stress development and affect the modulus. Therefore, when establishing a correlation between density and modulus, it is important to consider the different initial densities observed in the field.

This section of the chapter found that even at a constant moisture content, there exists a non-unique relationship between modulus and density ($\rho_{d,N}$) or void ratio (e_N) because of different initial void ratios (e_0). This observation is based on a series of experiments performed using three experimental setups: extra-large wheel tracker test, constant peak stress 1-D test, and constant radial stiffness triaxial test, testing four different geomaterials under cyclic loads. The three test setups allow for measuring different modulus types, mimicking the diverse moduli representative of the field conditions. For instance, the constant peak stress cyclic 1-D test measures the plastic modulus of the geomaterial, while extra-large wheel tracker test and constant radial stiffness triaxial test are performed to evaluate the elastic or unloading modulus, as applicable to traffic loads in pavements.

5.3.1 Materials and Test Methods

Material behaviour subjected to repeated loading was studied in three different experimental setups. Each scenario provided a different perspective on the material behaviour and allowed the study of material properties during repeated loading.

5.3.2 Extra-large wheel tracker test

A prototype of the roller compactor (extra-large wheel tracker test) was first employed to investigate the material properties (as shown in Figure 5-1(a)) under a constant load. The material under investigation was an unbound granular material (UGM), also known as a crushed rock with moderate fines, which makes up the base layer of a pavement (referred to as Material 1 in this chapter). Further details of the test and setup can be found in Bodin et al. (Bodin et al. 2013).

During the constant load test, the geomaterials were compacted using a compaction foot and subjected to a load of 5 kN. The deformation during compaction was recorded using linear variable differential transformers (LVDTs) attached to the bottom of the mould. In a previous

study, the authors established a constitutive equation that can calculate the Youngs' modulus of the geomaterial (E_G) based on the compactor's applied load and other known parameters (Tophel et al. 2023) using

$$E_G = \frac{(H_0 C_1)^{\frac{-2\beta}{1+\beta m}} exp\left(\frac{2\beta}{C_1(1+\beta m)} \times \frac{(e_0 - e_N)}{1+e_0}\right) \times \left(\frac{\pi LR}{F}\right) E_s(1-\nu_1^2)}{E_s - (H_0 C_1)^{\frac{-2\beta}{1+\beta m}} exp\left(\frac{2\beta}{C_1(1+\beta m)} \times \frac{(e_0 - e_N)}{1+e_0}\right) \times \left(\frac{\pi LR}{F}\right) E_s(1-\nu_2^2)}, \quad (5)$$

where ν_1 and ν_2 are the Poisson's ratio of the geomaterial and the cylindrical compactor, respectively, E_s is Young's modulus of the steel compactor, F is the load applied by the compactor, whereas L is the length of the compactor, R is the radius of the compactor; C_1, m, α and β are material model parameters. The void ratio e_N at cycle, N is calculated from the initial void ratio and height i.e., e_0 and H_0, respectively, using the deformation measured during compaction.

5.3.3 Constant peak stress cyclic 1-D test

The constant peak stress cyclic vibratory tests under 1-D conditions were conducted using a modified Proctor mould with dimensions of 150 mm in diameter and 150 mm in height, as shown in Figure 5-1(b). The setup allowed the study of the materials' properties at stresses equivalent to those of a roller compactor and a frequency equivalent to vibratory rollers (Tophel et al. 2022). In this test, the applied peak vertical stress was 1120 kPa, and the vibration frequency was 18 Hz. The test was performed on a sandy material (named Material 2 in this chapter) at a different moisture content, which forms part of the subgrade layer in the pavement cross-section. The modulus calculated in this test was the plastic modulus (E_p) which is defined as the ratio of the vertical stress to the incremental plastic strain during the constant peak stress cyclic 1-D test compaction.

5.3.4 Constant radial stiffness triaxial test

A Constant Radial Stiffness Triaxial (CRST) test (Figure 5-1(c)) was then carried out on silty sand, a commonly used material for a pavement subbase and subgrade layer (named Material 3 in this chapter). To further validate the observations made for Material 3, a class 2 crushed rock, commonly used for the base layer of a pavement (named Material 4 in this chapter) was tested. In contrast to the traditional repeated load triaxial (RLT), the CRST concept provides radial stiffness against which radial deformation could occur, thereby increasing the radial stress based on the radial stiffness provided. This boundary condition is considered superior

to the constant radial stress condition in RLT, better simulating the pavement material behaviour under traffic loads and facilitating residual radial stress development, which is commonly responsible for achieving shakedown (Yu 2007). In this instance, a modified version of the Precision Unbound Material Analyser (PUMA), developed by The University of Nottingham and Cooper Research Technology, is used (Li et al. 2017; Dutta and Kodikara 2022). The constant radial/lateral stiffness boundary condition was achieved using rubber bands that offered variable lateral stress conditions in the field. A stainless-steel band equipped with strain gauges was placed outside the rubber band to measure the lateral strain in the band while the sample was loaded vertically. The circumferential strain in the band was used to compute the lateral strain and lateral stress on the soil sample using equations provided by Dutta and Kodikara (2022). The applied vertical stress for tests on Material 3 was 360 kPa with a loading time of 0.1 sec and a rest time of 0.9 sec. The initial lateral stress (σ_{lat}) and stiffness (K_{lat}) used in these tests were approximately 10 kPa and 7 MPa respectively. In the case of Material 4 testing, the applied vertical stress was 500 kPa, while the other parameters were same as for Material 3.

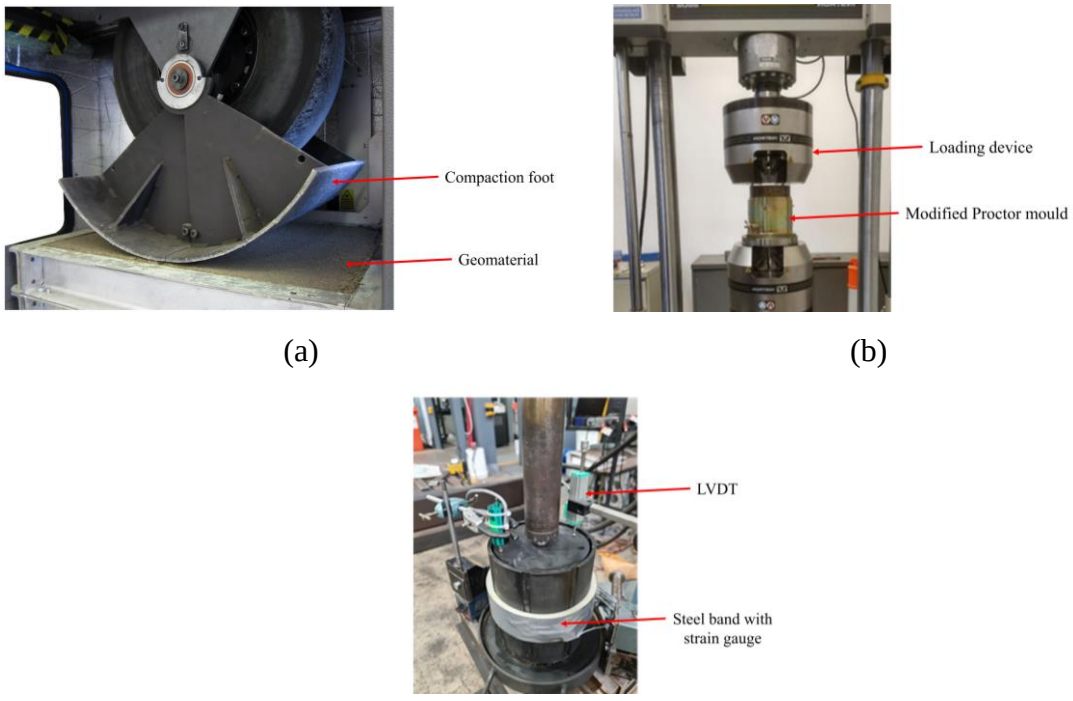

(a) (b)

(c)

Figure 5-1. Experimental setup pictures: (a) extra-large wheel tracker apparatus; (b) constant peak stress cyclic 1-D test; and (c) constant radial stiffness triaxial test.

Using the information of vertical and lateral stresses and strains, the resilient modulus of geomaterial (M_r) can be calculated as

$$M_r = \frac{(\sigma_{1,resilient})^2 + (\sigma_{1,resilient})(\sigma_{lat,resilient}) - 2(\sigma_{lat,resilient})^2}{(\sigma_{1,resilient})(\Delta\epsilon_{1,resilient}) + (\sigma_{lat,resilient})(\Delta\epsilon_{1,resilient}) - 2(\sigma_{lat,resilient})(\Delta\epsilon_{lat,resilient})}, \quad (6)$$

where $\sigma_{1,resilient}, \sigma_{lat,resilient}$ are the resilient stresses in the vertical and lateral directions due to the applied vertical stress, and $\Delta\epsilon_{1,resilient}, \Delta\epsilon_{lat,resilient}$ are the resilient strains in the axial/vertical and lateral directions, respectively. The equation is similar to the one developed in European standard EN 13286-7 (EN 2004).

5.3.5 Materials characterization

The grain size distribution of the four materials used in this chapter is shown in Figure 5-2 with Table 5-1 listing their geotechnical properties.

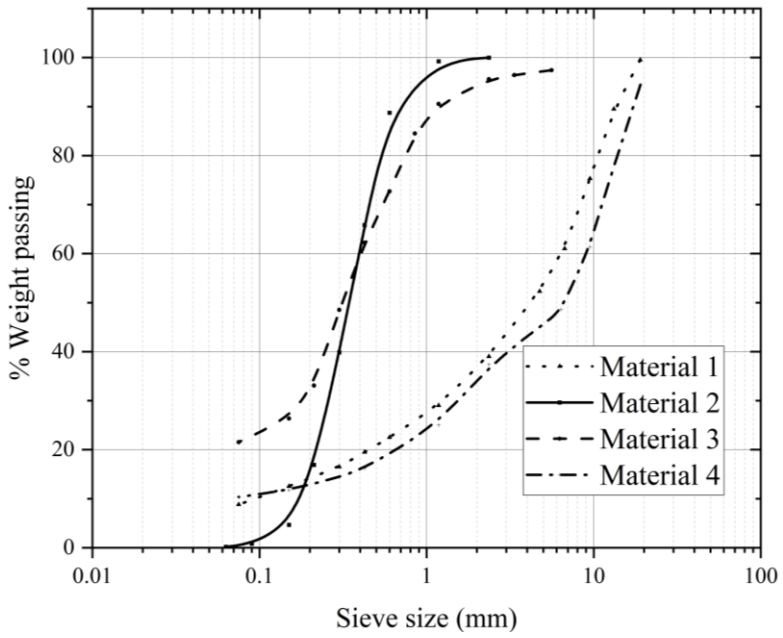

Figure 5-2. Grain size distribution of the four materials used in this section.

5.4 Results and discussion

5.4.1 Influence of stress history and initial void ratio for constant load test

The incremental plastic deformation (ΔH_p) and incremental (average) plastic strain ($\Delta \epsilon_p$) variations of samples of Material 1 at a constant 4.13% gravimetric moisture content are plotted against void ratio at cycle number N (e_N), as shown in Figure 5-3(a) and (b), respectively. It can be observed that both parameters depend not only on the current void ratio (e_N), but also on the initial void ratio (e_0) of the sample. At a particular e_N, both parameters are lower for a higher initial void ratio. The small difference in the values of ΔH_p and $\Delta \epsilon_p$ corresponds to the difference in initial height of the samples.

Table 5-1. Geotechnical properties of each material.

Material	Material 1	Material 2	Material 3	Material 4	Test Standard
Specific Gravity (G_s)	2.66	2.61	2.70	2.78	(Standards Australia 2002)
Optimum Moisture Content (OMC), modified Proctor (%)	6.6	9.3	8.0	5.8	(Standards Australia 2003)
Maximum Dry Density (MDD), modified Proctor (t/m^3)	2.2	1.85	2.08	2.35	(Standards Australia 2003)
Mean Particle Diameter (D_{50}) (mm)	4.5	0.45	0.32	6.5	(Standards Australia 2009)
Percentage passing the No. 200 sieve (%)	8.8	0.2	21	10	(Standards Australia 2009)

The non-unique relationships between ΔH_p and $\Delta \epsilon_p$ with e_N were also observed for geomaterial's Young's modulus (E_G), as shown in Figure 5-4, where the variation of E_G is plotted against void ratio. Although all the samples had the same moisture content (w), E_G was found to be dependent on e_0 of the sample and not unique for the same e_N or $\rho_{d,N}$. It should be noted that past research (Li and Selig 1994; Tatsuoka et al. 2021) also reported a non-unique relationship between density and modulus; however, the reason for this discrepancy is due to the difference in S_r. Referring to Figure 5-4, at a constant void ratio (which implies that the S_r is constant as w is constant), the E_G values were higher for samples compacted from a looser initial state or higher initial void ratio.

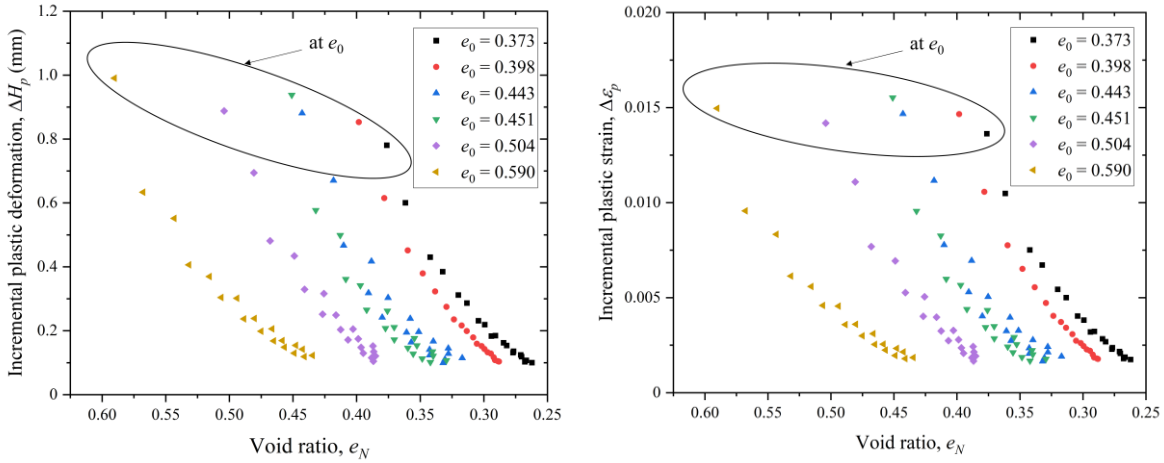

(a) (b)

Figure 5-3. Variation of geomaterial properties with e_N: (a) ΔH_p, (b) $\Delta\epsilon_p$ at 4.13% moisture content for Material 1 in Extra-large wheel tracker test (constant load test).

5.4.2 Influence of stress history and initial void ratio for a constant peak stress cyclic test under K_0 condition

The constant stress test also showed a similar pattern observed in Figure 5-4. The modulus, plotted against the void ratio for samples of Material 2 at different moisture contents, indicated that a sample with a higher initial void ratio was stiffer than a sample with a lower initial void ratio. The tests conducted on different moisture contents revealed the dependence of material properties on moisture content, void ratio, and initial void ratio, as shown in Figure 5-5.

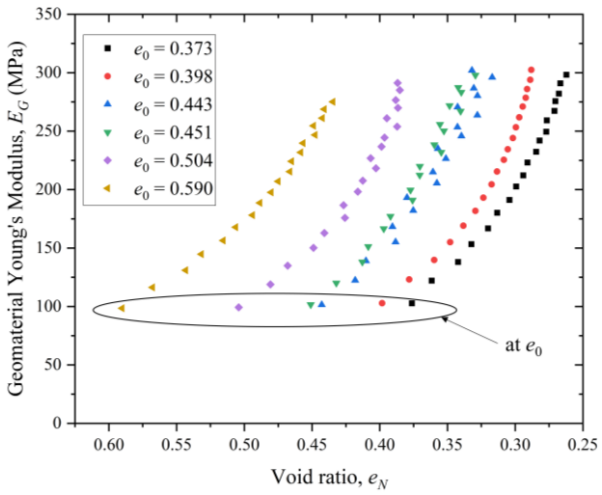

Figure 5-4. Variation of geomaterial's Young's modulus E_G with e_N for all six samples at 4.13% moisture content for Material 1 in Extra-large wheel tracker test (constant load test).

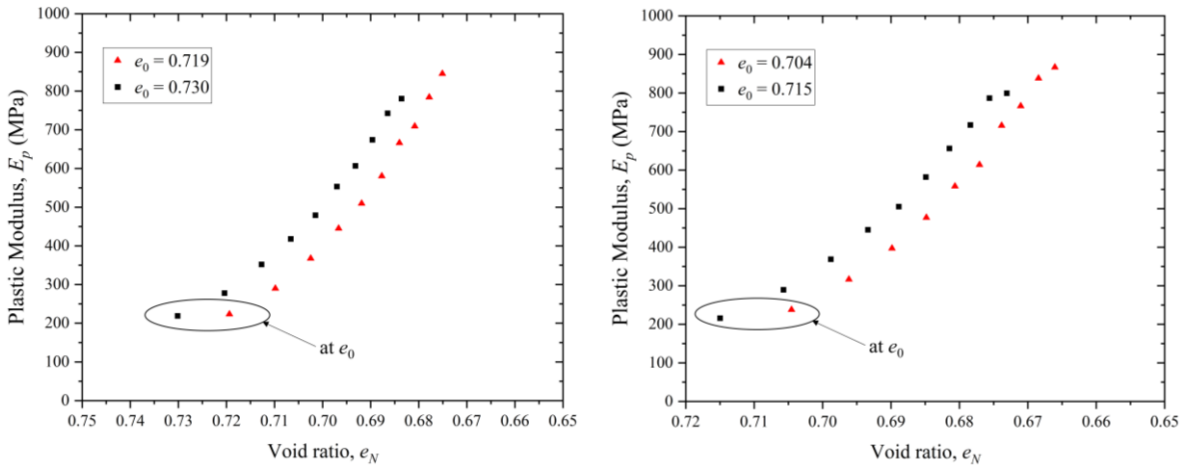

(a) (b)

Figure 5-5. Variation of plastic modulus with the void ratio for (a) moisture content of 5% and (b) moisture content 7% for Material 2 in constant peak stress cyclic 1-D test.

5.4.3 Influence of stress history and initial void ratio for CRST test

The CRST test showed similar behaviour for resilient modulus to the other two test setups (Figure 5-6(a)) for moisture content of 8% for Material 3. As stated before, the test setup allowed measurement of the lateral stress development during repeated cyclic loading which is shown in Figure 5-6(b).

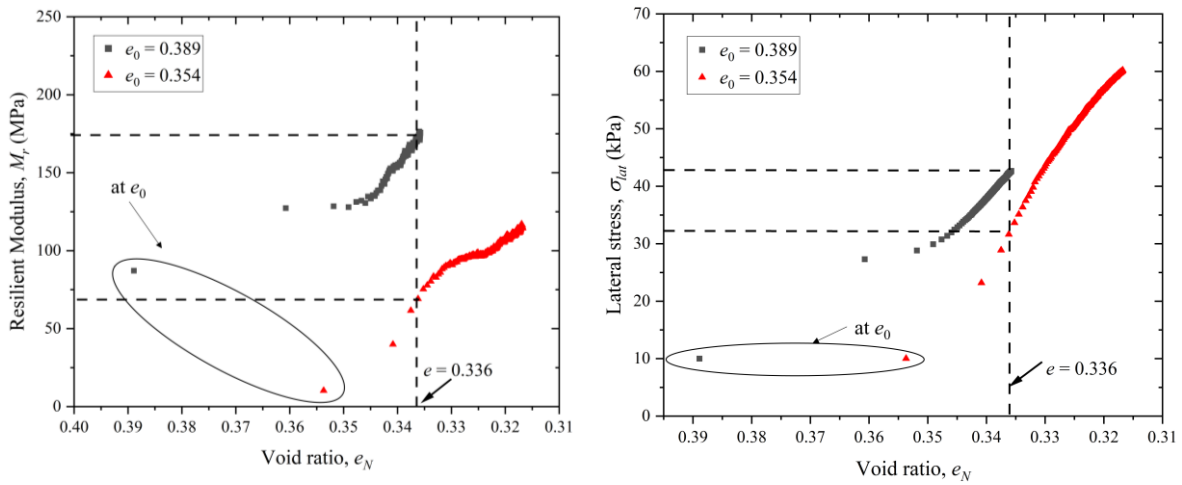

(a) (b)

Figure 5-6. Variation of (a) resilient modulus with void ratio and (b) lateral stress with void ratio at 8% moisture content for Material 3 in constant radial stiffness triaxial test.

Considering the same void ratio ($e = 0.336$), it can be seen that the values of lateral stresses are 42 kPa and 32 kPa for $e_0 = 0.389$ and $e_0 = 0.354$, respectively (from Figure 5-6(b)). This indicates that the sample with a higher initial void ratio undergo greater cumulative plastic deformation and therefore requires more cycles to reach a particular void ratio. This results in higher residual lateral stress development, which increases mean stress for specimens with higher e_0. This contributes to the higher resilient modulus value of 175 MPa compared to 70 MPa at the same void ratio/density of 0.336.

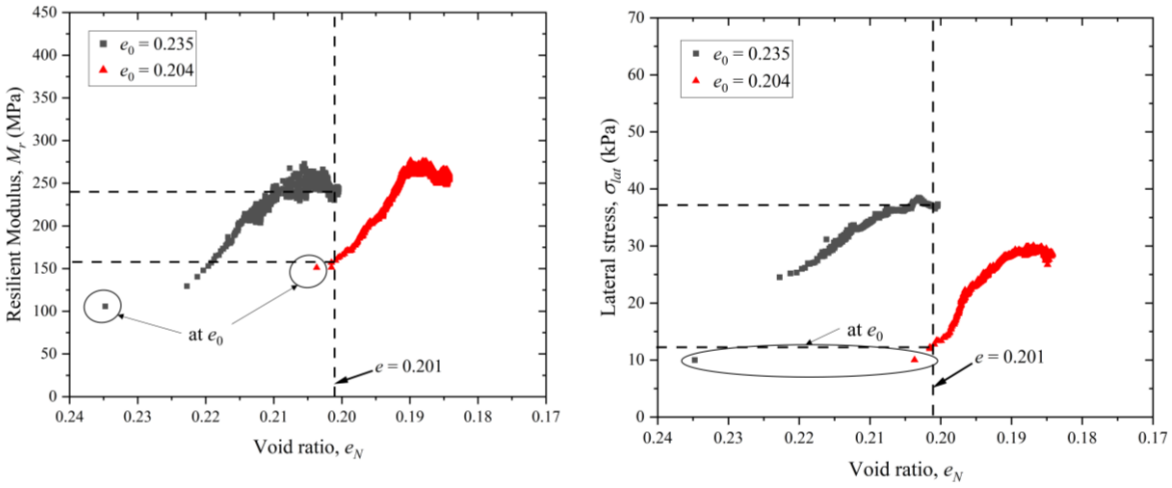

(a) (b)

Figure 5-7. Variation of (a) resilient modulus with void ratio and (b) lateral stress with void ratio at 4.9% moisture content for Material 4 in constant radial stiffness triaxial test.

For Material 4, tested at a moisture content of 4.9%, modulus and lateral stress behaviour are shown in Figure 5-7. Similar to Material 3, the lateral stresses are higher for a sample having a higher initial void ratio giving rise to a higher resilient modulus at one particular void ratio. Considering void ratio, $e = 0.201$, the values of lateral stresses are 37 kPa and 13 kPa for $e_0 = 0.235$ and $e_0 = 0.204$, respectively (from Figure 5-7(b)). The resilient modulus values are 240 MPa compared to 160 MPa for $e_0 = 0.235$ and $e_0 = 0.204$, respectively (from Figure 5-7(a)).

These observations can also be explained based on the theoretical model proposed by J. M. Pestana and Whittle (1995), where the elastic bulk modulus (K) is a function of void ratio (e) and mean effective stress (p') and as shown below:

$$K = K_0 p_a \left(\frac{1+e}{e}\right)\left(\frac{p'}{p_a}\right)^c, \quad (7)$$

$$p' = p + \chi s, \quad (8)$$

where K_0, c are fitting parameters, p_a is atmospheric pressure, p is mean net stress, s is suction, and χ is the Bishop's parameter (Bishop 1959) and which is considered equal to the degree of saturation (S_r) (Schrefler 1984; Houlsby 1997; Borja 2006; Kuczmann and Iványi 2008; Coussy 2011; Manzanal et al. 2011).

For a particular material having constant moisture and void ratio, the increase in p' is due to the increase in lateral stress in the sample as S_r is the same. This increase in p' results in an increase in bulk modulus (K).

5.5 Conclusions

Different plastic deformation and strain at the same void ratio lead to differing material properties due to their differing initial states. This was demonstrated in this short communication through three experiments testing four materials with different loading and boundary conditions. The results showed that the initial state affected the material's modulus and other properties due to different residual lateral stress built up during deformation. This residual lateral stress changes the mean stress, affecting the material's modulus. In the field, various spreading techniques result in different initial void ratio conditions. The modulus's dependence on the material's initial state may contribute to the lack of accuracy in the relationship between Intelligent Compaction (IC) variables and compaction density. This highlights the need to consider the initial state of the material when establishing any relationship between material parameters and a material's current state.

5.6 Summary

The importance of understanding the compaction process for civil engineering structures and the challenges associated with modelling roller compaction, which is complicated by the variable stress that affects material properties, has been highlighted. To address this issue, the constant stress model developed in Chapter 4 was extended to a constant load model by utilizing the geometrical relationship between the contact area and incremental plastic

deformation. The effect of moisture content, plasticity, and initial void ratio on compaction process and proposed simplified equations for dynamic parameters that vary with void ratio and the number of cycles was also investigated. The developed model not only provides an understanding of the material subjected to stresses equivalent to field compaction but also can be used to determine unknown parameters, such as initial density during compaction, which is discussed in Chapter 7 of the thesis. The model's use in predicting initial density would also allow to develop a better correlation with modulus and density.

Part 4: Instrumentation and Field Study

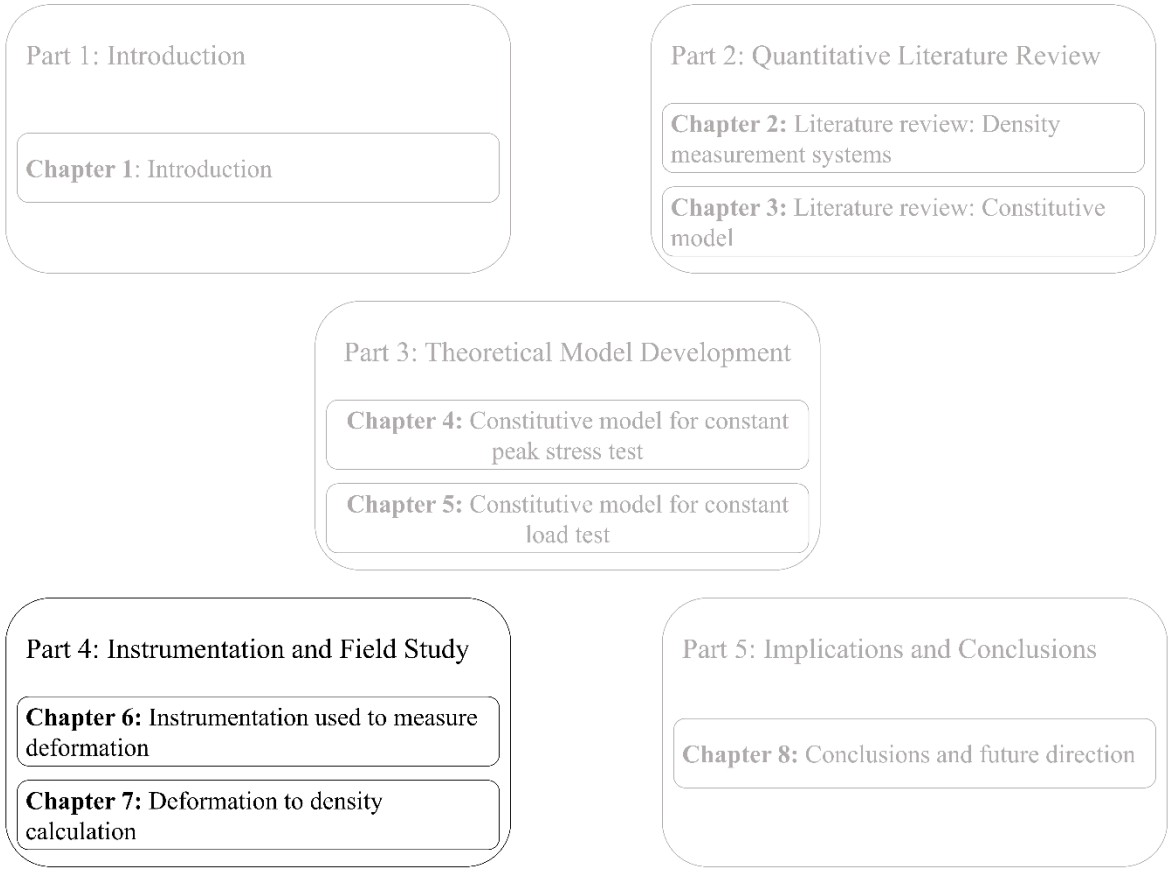

Chapter 6 Instrumentation used to measure deformation

This is the first chapter of Part 4: Instrumentation and Field Study. The chapter focuses on developing the methodology to measure deformation during compaction, which is divided into several sections. The first section introduces the concept of measuring deformation during compaction, followed by a discussion of factors that could impact the accuracy of those measurements. The following section explains the steps taken to minimize measurement errors. The instrumentation and methodology used in two experiments are then demonstrated, with Experiment 1 being indoors and Experiment 2 being outdoors. The differences in instrumentation between the two experiments are also discussed.

6.1 Conceptualization of deformation measurement technique during compaction

This study hypothesizes that deformation can be used to estimate density during compaction. Measuring deformation in the field requires combining highly precise equipment and advanced data analysis to reduce measurement errors (filtering the noise from the measured data) as the field environment could be very dynamic. To measure deformation, two displacement laser sensors are attached to the roller, one in front and one behind the front drum. The area behind the drum has already been compacted, while the area in front has not yet been compacted (Figure 6-1).

In an ideal case (see Figure 6-2), deformation can be calculated as representing the difference between the first range D_a (displacement ahead of the roller), the second range D_b (displacement behind the roller), and the initial distance of the sensor from the ground D_R, as follows:

a. plastic deformation or deformation $(\Delta_N) = D_b - D_a$;

b. total deformation $(\Delta_{N,total}) = D_R - D_a$; and

c. elastic deformation $(\Delta_{N,elastic}) = D_R - D_b$.

The total deformation $(\Delta_{N,total})$ is a measure of sinkage of the roller into ground due to the application of load, plastic deformation (Δ_N) is the difference between the surface elevation difference after and before roller load. Elastic deformation $(\Delta_{N,elastic})$ can be estimated by subtracting Δ_N from $\Delta_{N,total}$ which is the measure of how much soil has rebounded after the roller has passed over it. For the purpose of calculating the density only plastic deformation (Δ_N) is used here.

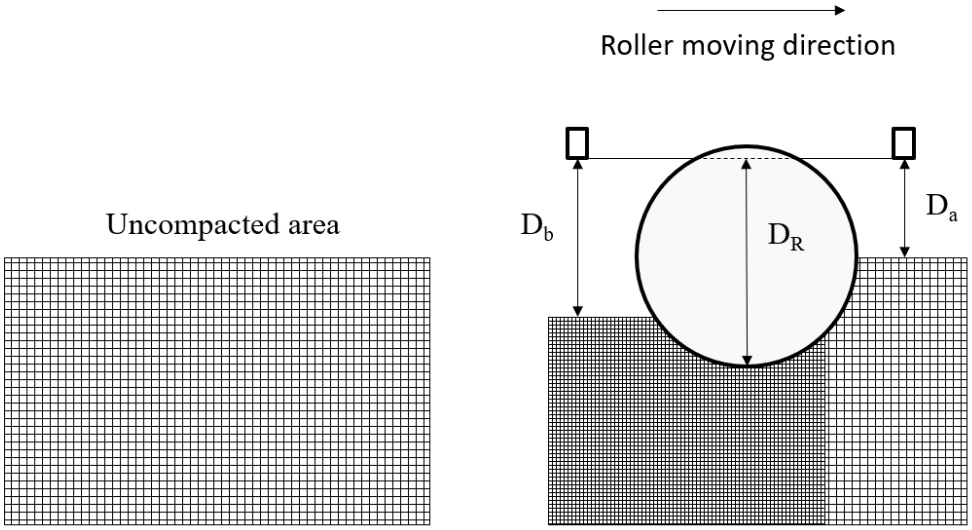

Figure 6-1. Schematic illustrating deformation pattern of geomaterial when a compactor passes over loose soil.

In order to account for roller deviations from horizontal, caused by an incline/decline in the surface and/or by bumps resulting in a horizontal rotation of the platform on which the distance sensor system is mounted, a correction to the measured plastic deformation is necessary. This correction involves measuring the inclination of the distance sensor system relative to the geomaterial being measured (denoted as pitch; α) using an orientation unit (inertial measurement unit (IMU) in this study). The measured pitch is then used to adjust the measured deformation by using a trigonometric function that considers the mutual distance (L_R) between the first and second distance sensors, as shown in Figure 6-2, such that

$$\Delta_{\mathrm{N}} = (D_b - D_a)\cos(\alpha) + L_R \sin(\alpha). \quad (9)$$

The error in deformation measurement could be very large; for example, if the L_R is 1 metre an inclination (α) of 1 degree changes the deformation measurement by around 17 mm.

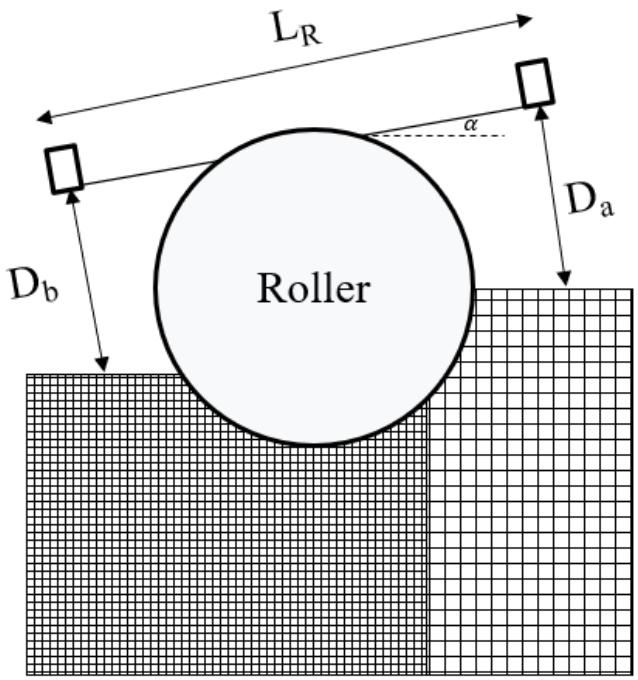

Figure 6-2. Deformation pattern of geomaterial when a compactor is passing over lose soil while it is inclined at an angle α because of unlevel ground surface.

Due to the potential for the compactor to also experience a rocking motion and rotation around an axis parallel to the movement direction of the platform, a roll correction is necessary to accurately measure the deformation. The roll angle, denoted as β, can be measured using the same orientation unit that measures pitch (α). The roll correction involves applying a trigonometric function to the measured roll angle (β) and adjusting the measured deformation accordingly. The corrected deformation is determined by combining the inclination correction and the roll correction such that

$$\Delta_{\mathrm{N}} = (D_b - D_a)\cos(\alpha)\cos(\beta) + L_R \sin(\alpha). \tag{10}$$

The measured signal from all the sensors are pre-processed to remove electrical noise for improving the measurement accuracy. This includes pre-processing the measured signals to mitigate electrical noise from the distance sensor system and orientation sensor system:

a. singularity removal (including sudden shifts or abrupt changes in the signal) by identifying points where the mean value is changing abruptly or above a selected threshold, and replacing it with the mean of a plurality of selected

neighbourhood points;

b. detrending to only show differences in values from the trend; and

c. frequency filtering (including band-pass filtering) by removing very low and very high frequency noise from the signal.

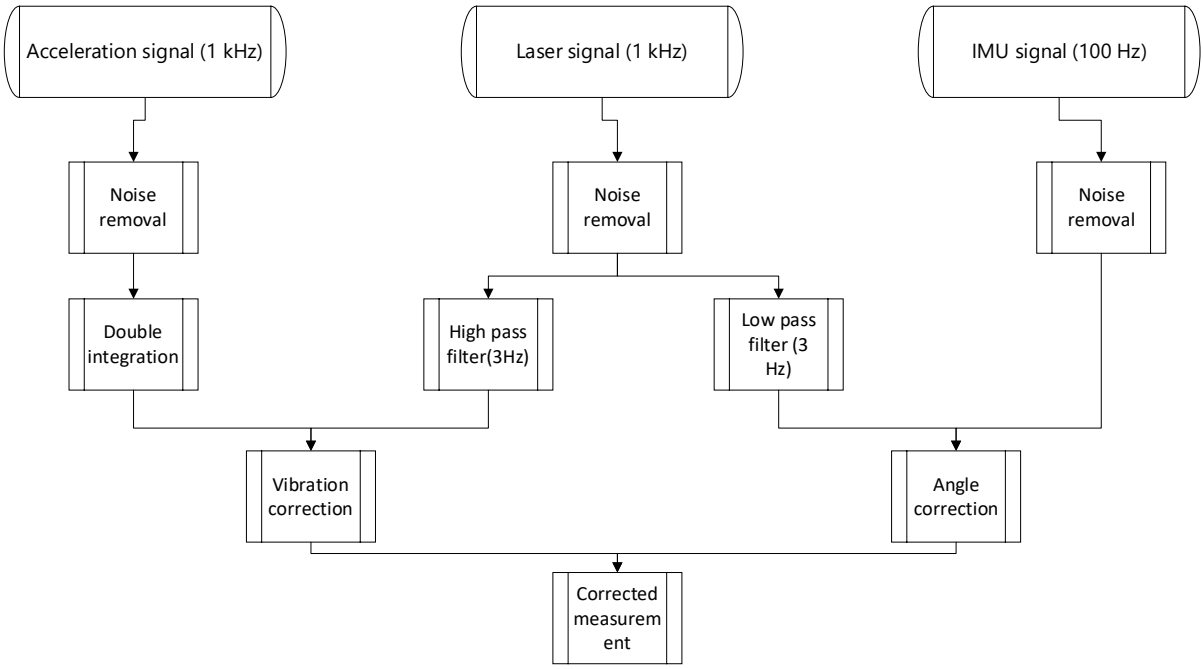

Figure 6-3. Flowchart of the deformation correction using accelerometer and IMU.

In the field, the vibration of the vibratory compactor may introduce noise into the distance data, affecting the accuracy of the deformation measurements. To address this issue, the sensor data from the distance sensor system are pre-processed to correct for the vibrations/movement. The displacement noise is calculated from an acceleration signal by double integrating the acceleration noise, and the system is configured to remove the displacement noise from the distance measurements. The correction chart is depicted in Figure 6-3. The displacement sensor system (e.g., the laser systems) is unable to measure signals with frequency less than a certain lower frequency value (dependent on the geomaterial type, for this study 0.1 Hz), and the error due to the inclination was around a determined frequency (depending on the geomaterial type, for this study it was found to be 3 Hz). These two frequencies (lower frequency and the determined frequency) were determined experimentally for the geomaterial type. Therefore, the system included a plurality of frequency filters (including bandwidth filters) to separate the signals from the distance sensor system for undertaking a separate correction of the motion (vibrations) and the orientation (inclination).

The instrumentation and methodology were developed in stages. The first trial of the instrumentation was conducted in an indoor setting (referred to as Experiment 1 hereafter). Based on the results of this testing, improvements were made, and then an outdoor field experiment was performed (referred to as Experiment 2 hereafter). As a result, the instrumentation details differed for both experiments. The details of the instrumentation are provided in the following sections.

6.2 Roller instrumentation

An overview of the roller instrumentation used for Experiment 1 is illustrated in Figure 6-4. The complete instrumentation of the roller included two triangulation laser sensors, one attached in front of the front drum (as the front drum was the vibrating one) and the other attached to the rear of the front drum. To measure the inclination/rotation of the laser sensors, an IMU was attached on the top of the front laser. Moreover, the drum and frame vibration and the overall movement of the roller were monitored in three dimensions using two accelerometers, attached to each of the drums. The geolocation of the roller was recorded using a Universal Total Station (UTS).

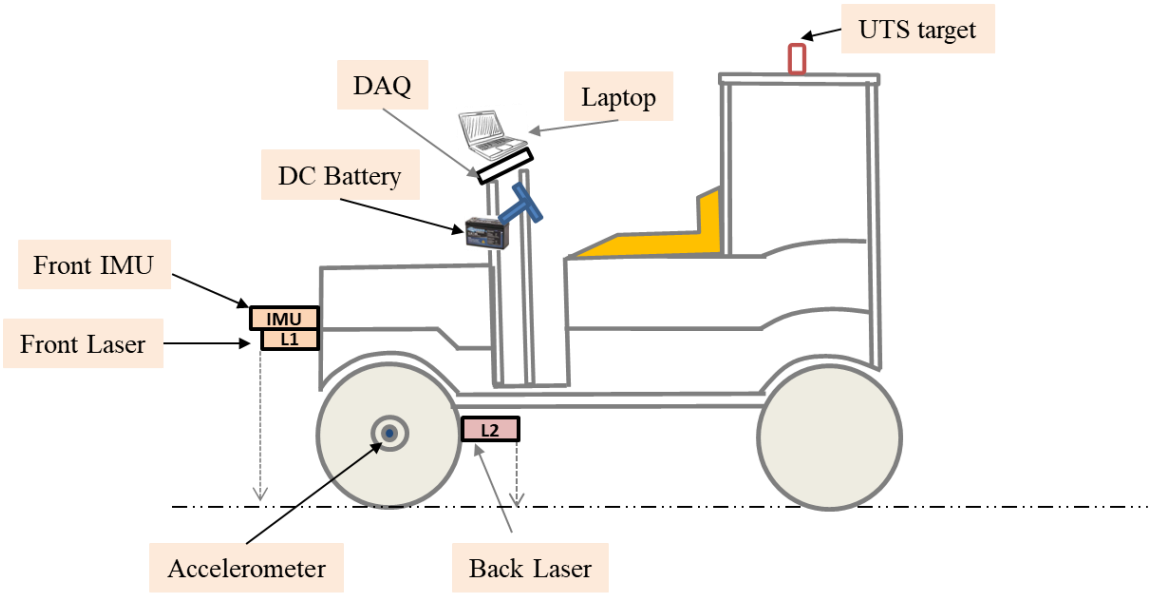

Figure 6-4. Schematic of the instrumented roller for Experiment 1.

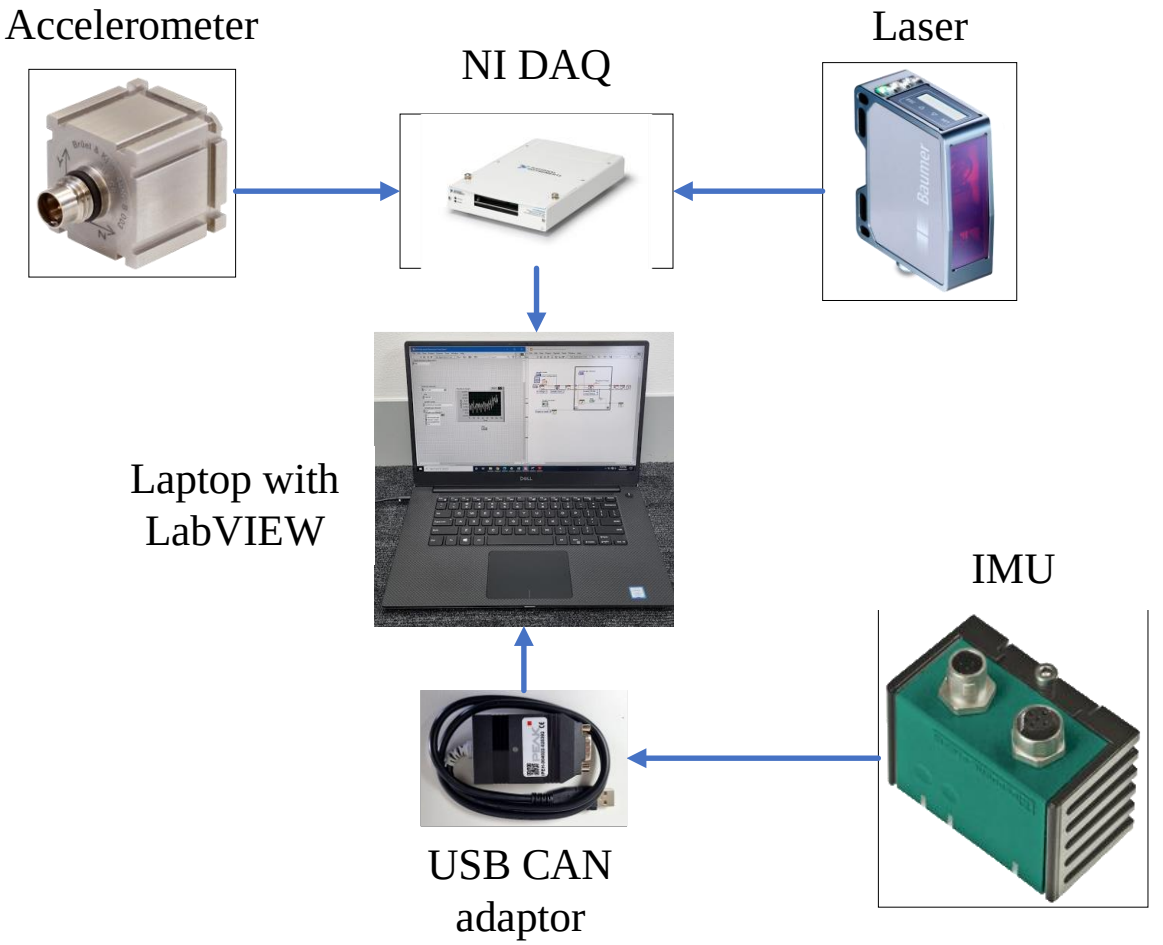

Figure 6-5. Schematic diagram showing the instrumentation and data flow in Experiment 1.

The accelerometers provided valuable information for detecting and monitoring the rigid body motion of the roller. The data from all of the sensors were acquired via a 16-bit, 250-kHz data acquisition (DAQ) system manufactured by National Instruments (NI) connected to a Windows-based Dell Precision 5530 laptop PC. The PC was equipped with National Instruments' Laboratory Virtual Instrument Engineering Workbench (LabVIEW), a visual programming language environment. LabVIEW was used to acquire all the signals and conduct real-time signal analysis. A schematic diagram of the instrumentation and data flow for Experiment 1 is shown in Figure 6-5.

For Experiment 2, lasers sensors were installed such that there were three in front and three behind the rear drum (as the rear drum was the vibrating one), evenly distributed along the width of the roller; instead of one in the front and one at the back as in Experiment 1. This helped reduce the deformation measurement error caused by the variability in material surface

topography along the width of the roller. The laser sensors used in Experiment 2 were also more precise than those used in Experiment 1 and utilized ethernet for data transmission. Therefore, a switch was used instead of the DAQ in Experiment 1. The data collection platform used for Experiment 2 was Python. It was also discovered that the vibration noise could be removed equally well by taking the average of the signal over a period of time, rather than using the accelerometer data. This decision was favoured by the fact that the accelerometer data collection compromised the data collection from six laser sensors, as the PC had limitations on its bit per second (bps) capacity. The IMU used in Experiment 2 also allowed for inclination measurement with higher accuracy. The instruments utilized in this study were pre-calibrated by the manufacturer. The outputs from these instruments, based on this pre-calibration, were directly used in the study without any further calibration procedures. Details of all instruments are provided in subsequent sections.

6.3 Laser systems details

In Experiment 1, two triangulation displacement laser line sensors were used. In the triangulation principle, a beam of light is transmitted by the sensor to the object being measured, with the reflected light striking the receiver line in the detector at a unique angle. The distance to the object is calculated based on the angle of incidence. The laser used is a pulsed red laser diode with a wavelength of 600 nm. Table 6-1 lists its precision and accuracy when measuring in a vibrating environment, making it a suitable choice for this purpose. The laser beam is classified as class 2, which ensures its safety. The beam characteristic of the laser is illustrated in Figure 6-6.

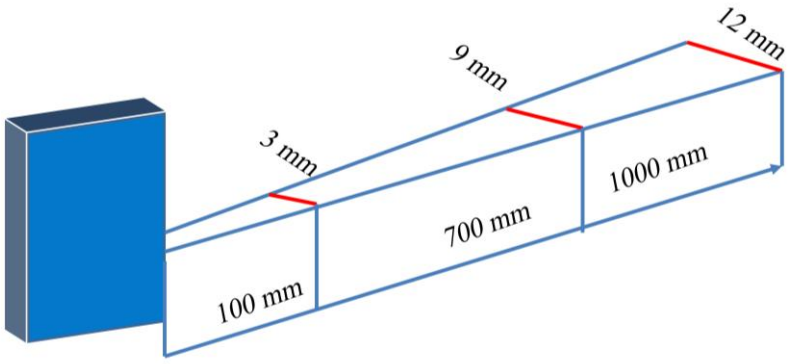

Figure 6-6. Typical beam characteristics of the laser used for Experiment 1 (not drawn to scale).

Table 6-1 shows the two different types of laser sensors used for Experiment 1 and Experiment 2 and their descriptions. The major difference between the two systems is that the sensors in Experiment 2 have a smaller measuring range (500 mm) than in Experiment 1 (900 mm). The resolution and repeat accuracy of the sensors in Experiment 2 were better than in Experiment 1.

Table 6-1. Description of the laser sensors used for Experiments 1 and 2.

Laser	Experiment 1	Experiment 2
Manufacturer	OMRON Corporation	OMRON Corporation
Model	OM70-L1000.HV0700.VI	OM70-L0600.HV0350.EK
Sampling Frequency (Maximum)	2.5 kHz	2.0 kHz
Measuring Distance (Sd)	100-1000 mm	100-600 mm
Measuring Range (Mr)	900 mm	500 mm
Resolution	3-63 µm	3-24 µm
Repeat Accuracy	1-32 µm	1-9 µm
Linearity error	±0.19 % Mr	±0.12 % Mr
Output circuit	Analog and RS 485	Ethernet
Voltage supply range (VDC)	+15 to +28	+15 to +28
Output signal	+4 to +20 mA / 0 to +10 VDC	+4 to +20 mA / 0 to +10 VDC
Operating temperature	-10 to 50 ℃	-10 to 50 ℃
Temperature error	0.065 % Sd/K	0.065 % Sd/K
Light source	Pulsed red laser diode	Pulsed red laser diode
Wavelength	660 nm	660 nm
Laser class	2	2
Protection class	IP 67	IP 67
Dimensions	26×55×74 (mm)	26×55×74 (mm)

6.4 Inertial Measurement Unit (IMU)

The IMU utilized in this study has six degrees of freedom, combining a triaxial acceleration sensor and a triaxial gyroscope to provide acceleration, inclination, and rotation rate measurements. The built-in fusion algorithm is specifically designed for inclination measurement, and provides adequate compensation for external acceleration disturbances. The ability of this device to provide reliable measurements, even in noisy environments, made it suitable for use in this project. The IMU outputs eight elements: acceleration, angular rate, rotational acceleration, gravity vector, linear acceleration, rotation angles, quaternion, and temperature. Although the primary purpose of the IMU in this study was to use the rotation angle data to correct the laser measurement, all other data elements were also recorded.

Data transfer from the IMU was via the integrated controller area network (CAN) SAE J1939 interface, as opposed to the analog interfaces used by the laser and accelerometer. Therefore, a suitable CAN to USB adapter (PCAN-USB FD from PEAK-System) was used to send the data to a Windows-based PC. The CAN interface allowed for recording of data from all elements, including multiple sensors, using just two wires, which is not possible with analog interfaces. The dynamic inclination measurement technology offers the capability to simultaneously measure inclination, acceleration, and rotation rate in all three axes, even in external acceleration. This feature made it suitable for applications that experience external disturbances, such as vibrations, shocks, and movements. The adjustable ranges compensate for external accelerations, while the adjustable thresholds enable the detection of measured value overruns. This provides users with greater flexibility and control over the accuracy and precision of the measurements

Table 6-2 shows the different IMUs used for Experiments 1 and 2 and their descriptions. The major difference between the two systems is that the sensors in Experiment 2 had a higher acceleration measuring range that provided better stability of inclination measurement during the high vibration of the compactor.

Table 6-2. Description of the IMUs used for Experiment 1 and Experiment 2.

IMU	Experiment 1	Experiment 2
Manufacturer	PEPPERL+FUCHS	PEPPERL+FUCHS
Model	IMU360D-F99-B20-V15	IMUF99PL-SC3600-0KB20V1501
Sampling Frequency (Maximum)	800 Hz (100 Hz per element)	800 Hz (100 Hz per element)
Rated capacity/ Measuring range	acceleration: ± 2 g inclination: 0 – 360 ° rotation rate: ± 250 °/s	acceleration: ± 4 g inclination: 0 – 360 ° rotation rate: ± 250 °/s
Resolution	acceleration: 0.001 g inclination: 0.01 ° rotation rate: 0.01 °/s	acceleration: 0.001 g inclination: 0.01 ° rotation rate: 0.01 °/s
Output circuit	CAN bus with SAE J1939 protocol	CAN bus with SAE J1939 protocol
Voltage supply range (VDC)	5 to +30	5 to +30
Output signal (VDC)	Not Applicable	Not Applicable
Operating temperature	+15 to +85 °C	+15 to +85 °C
Temperature error	max. ± 1.5°	max. ± 1.5° at +15 to +85 °C
Protection class	IP 68/ IP 69K	IP 68/ IP 69
Dimensions	37.5×45×65 (mm)	37.5×45×65 (mm)

6.5 Accelerometer

In addition to the lasers and IMU, the two most essential sensors used for this study, was an accelerometer installed to track the rigid body movement and measure the vibration transmitted from the drum to the sensors. During the trial, typical maximum drum acceleration amplitudes observed during testing were ± 8 g (gravitational force). The critical accelerometer specifications and the measurement range included high sensitivity, high sampling frequency, and low-temperature error. The Brüel & Kjær type 4506-B-003 Miniature Triaxial Piezoelectric Constant Current Line Drive (CCLD) Accelerometer with transducer electronic data sheet (TEDS) was ideal (Table 6-3). To mount the accelerometers, thin polycarbonate mounting clips were used. The accelerometers were connected to the DAQ with AO-0526 BNC (male) connectors, which are super low-noise cables and conditioned with a signal conditioner PCB designed in-house and the circuit diagram is shown in Figure 6-7.

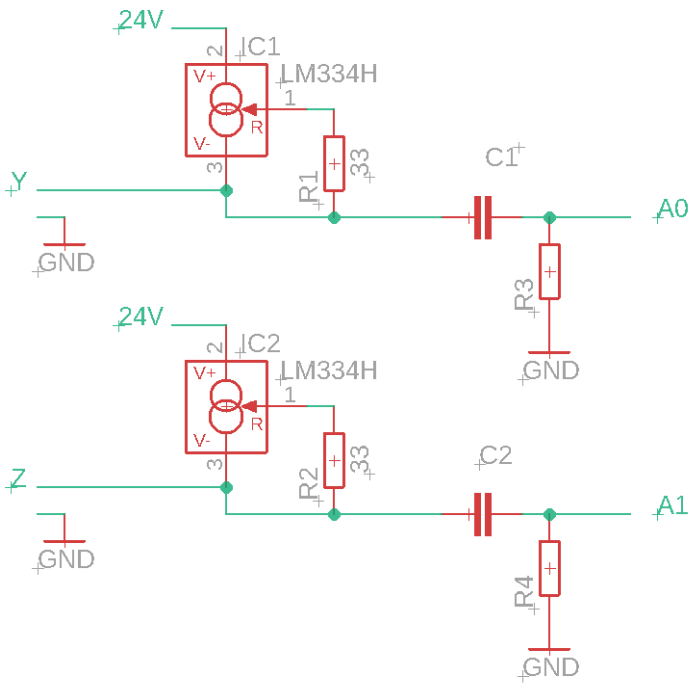

Figure 6-7. Circuit diagram for PCB used for accelerometers.

Table 6-3. Specifications of the accelerometer used in Experiment 1.

Instrument	Accelerometer
Manufacturer	Brüel & Kjær
Model	4506-B-003
Sampling Frequency (Maximum)	2 kHz
Rated capacity/ Measuring range	± 14 g
Sensitivity/Resolution	490 ± 10% mV/g
Output circuit	Analog
Voltage supply range (VDC)	+24 to +30
Output signal (VDC)	-10 to +10
Temperature error	X: 0.15, Y, Z: 0.12 %/°C
Operating temperature	(–54 to +100 °C)
Dimensions, mm	17×17×17

6.6 Switch

An Advantech Ethernet switch (EKI-2728-BE) was utilized to create a network to communicate between the laser sensors and PC in Experiment 2 (Table 6-4). The switch had 8 ports and compatibility with various Ethernet protocols, including Institute of Electrical and Electronics Engineers (IEEE) 802.3, IEEE 802.3u, and IEEE 802.3ab. The switch is designed for industrial settings and can function within temperatures ranging from -10°C to 60°C. It includes multiple features that bolster network reliability and security, such as redundant power inputs, port-based virtual local area network (VLAN), QoS, and storm control. Additionally, the switch allows for various management options, such as simple network management protocol (SNMP), web browser, and command line interface (CLI), rendering it effortless to configure and monitor.

6.7 Geolocation system

Experiment 1 involved using a Universal Total Station (UTS) SPS930 from Trimble, which is a surveying instrument that measures angles and distances to determine the location of points in three-dimensional space. This high-precision total station model is specifically designed for

challenging surveying applications, utilizing advanced tracking and measuring technology to ensure accurate measurements.

Table 6-4. Switch specifications used for Experiment 2 to acquire signals from laser sensors.

Instrument	Switch
Manufacturer	Advantech
Model	EKI-2728/I
Connectors	8 × RJ 45
Transmission speed	Up to 1000 Mbps
Voltage supply range (VDC)	+12 to +48
Operating temperature	-10 to 60 °C
Protection class	IP 30
Dimensions	30 × 140 × 95 mm

Experiment 2 used a global positioning system (GPS) with a fixed real-time kinematic (RTK) correction for precise positioning of the roller in the outdoor environment rather than the UTS. GPS is a satellite-based navigation system that provides location information with high accuracy. RTK is a GPS surveying technique that utilizes a fixed base station to correct errors in the GPS signal, providing even higher accuracy.

6.8 Other steps to detect and prevent noise in the system

Several studies were conducted to measure the noise sources in the sensors and the DAQ. One study involved acquiring data from all the sensors mounted on a stationary roller. The lasers, IMU, and accelerometer data were collected with the stationary machine on the construction site.

Upon analyzing the samples, it was found that the noise due to electronic interference under regular operation was minimal, with a standard deviation of approximately 1 milli-g for accelerometers. Three main factors contributed to this observation:

a) The use of shielded or coaxial cables to connect all the sensors, combined with the use of differential inputs of the DAQ;

b) Keeping the cable length as short as possible; and

c) Powering the sensors with two 12V Lithium-ion batteries connected in series to provide 24V, rather trhan a single 12V battery.

6.9 Installation of all the sensors on the roller

All of the sensors were attached to the compactor using custom-made brackets because off-the-shelf mounting solutions were not suitable for this application. The brackets were fabricated by the technical team at the Department of Civil Engineering at Monash University. Figure 6-8 shows the different brackets used for Experiments 1 and 2. As Experiment 2 used three sensors instead of one, three attachments were made as represented. Custom-made brackets allowed the sensors to be attached to any type or size compactor.

(a) (b)

Figure 6-8. Custom designed brackets to install the sensors to the compactor.

6.10 Summary

The instrumentation required to measure deformation accurately during compaction was determined. Highly precise equipment and advanced data analysis were used to reduce measurement errors, as the field environment is very dynamic. The deformation was measured using laser sensors attached before and after the drums. Correction of the measured plastic deformation was necessary to account for inclination of the roller caused by uneven surfaces, and a roll correction was needed to address the potential for the compactor to experience rocking motion and rotation around an axis parallel to the movement direction of the platform.

Pre-processing signals were also required to remove electrical noise to improve measurement accuracy. In addition, the distance sensor system data were pre-processed to correct for vibrations/movement. The instrumentation and methodology were developed in stages, and the first trial of the instrumentation conducted in an indoor setting, followed by an outdoor field experiment.

The accurate measurement of deformation is necessary for the precise estimation of compacted density. The next chapter presents the methodology and analytics developed to convert the deformation measurements from the instrumentation described here to density, along with the results from Experiments 1 and 2 mentioned here.

Chapter 7 Deformation to density calculation

Chapter 7 of the thesis is the second chapter in Part 4: Instrumentation and Field Study. The preceding chapter provided a detailed account of the instrumentation and methodology employed to measure deformation during compaction and mitigate data noise; while this chapter expands upon these foundations by presenting various approaches to estimating density based on the obtained deformation data. Furthermore, it offers a concise summary of the experimental procedure conducted during field testing. It also includes details regarding the materials tested and the diverse rollers utilized. Specifically, the chapter explores different methods for converting deformation measurements to density values. It explores the potential of the previously developed model from earlier chapters to enhance density estimation accuracy.

This chapter constitutes a pivotal element within the overarching focus of the thesis on estimating density during compaction through advanced instrumentation. The chapter augments the comprehensiveness of the methods employed and the results obtained during the field study by encompassing information on estimating density from deformation data and summarising the experimental procedure.

7.1 Methodology to correlate deformation to density

Once the deformation caused by the compactor has been measured, it can be utilized to estimate density. The relationship between deformation and density depends on factors such as material type, compactor type, material initial condition, and moisture content. The influence of material type, different loading conditions, and moisture content has already been investigated at a laboratory scale and presented in Chapters 4-6. Accordingly, in the field study here, greater emphasis was placed on studying the effect of the material's initial condition while keeping other factors constant. Two main methodologies were employed to establish a correlation between deformation and density: (a) regression-based and (b) classification-based.

7.1.1 Regression-based method

The regression-based method employs deformation measurements to establish a mathematical relationship that can estimate the numerical value of density. To assess the accuracy of density estimation, the performance of the models was evaluated against ground truth density

measured using nuclear density gauge (NDG). This evaluation involved calculating the mean absolute error (MAE) between the estimated or predicted density from the deformation (ρ_p) and measured density from NDG (ρ_m) as a benchmark according to

$$\text{MAE} = \frac{|\rho_m - \rho_p|}{N_m}, \tag{11}$$

where N_m is the total number of measurements.

7.1.2 Classification-based method

For a geotechnical engineer, comparing measured and predicted densities with regard to MAE does not provide sufficient information. Therefore, the assessment was also based on classification accuracy, specifically determining whether the area was correctly classified as compacted. Classification is a predictive modelling technique that assigns data into discrete classes or categories based on input variables. In classification, the objective is to learn a decision boundary that effectively separates the different classes. The prediction process for this study was divided into four parts, as shown in Figure 7-1: true positive (when both the predicted and measured densities are above MDD or target density) (marked as area (1) in Figure 7-1), false negative (when the predicted density is below MDD while the measured density is above MDD) (marked as area (2) in Figure 7-1), true negative (when both densities are below MDD) (marked as area (3) in Figure 7-1), and false positive (when the predicted density is above MDD while the measured density is below MDD) (marked as area (4) in Figure 7-1). These four outcomes are collectively known as the confusion matrix of a model. For this study, a false positive is hereafter assumed to be the critical error, as it shows that the predicted density is more than the target density. However, in reality, the density is inadequate and less than the target density.

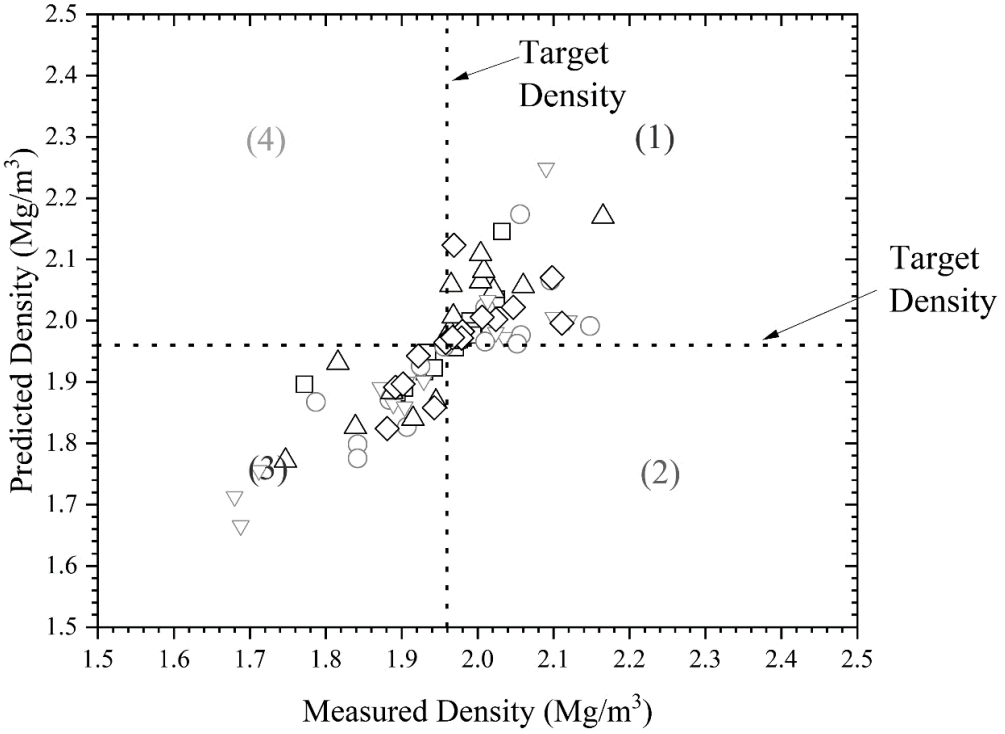

Figure 7-1. Illustration of classification of the compacted area in terms of predicted and measured densities: (1) true positive; (2) false negative; (3) true negative; (4) false positive.

7.1.3 1D compression equation

In the previous chapter, it was discussed that during one compaction pass, the plastic deformation is estimated as Δ_N. Summing all the plastic deformations from each pass, the total plastic deformation (hereafter plastic deformation is referred to as deformation) (ΔH_N) until pass N can be calculated as

$$\Delta H_N = \sum_{i=1}^{N} \Delta_N. \tag{12}$$

In 1D compaction, the material is assumed to deform solely in the vertical direction (see Figure 7-2), with no lateral spreading (thus maintaining a constant cross-sectional area). Recently, Tophel et al. (2022) proposed that the compaction process of geomaterials could be approximated as 1D compaction, a hypothesis that was subsequently validated by (Brzeziński et al. 2022; Yin et al. 2023) using the photogrammetry method. The final density (ρ_f) after compaction can be calculated using

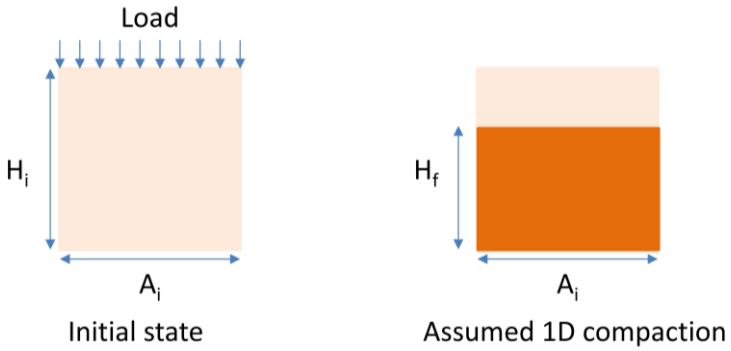

Figure 7-2. 1D compression schematic showing the deformed state before and after compaction.

$$\frac{\Delta H_N}{H_i} = \frac{\rho_f - \rho_i}{\rho_f}, \tag{13}$$

where H_i is the initial layer thickness, ΔH_N is the total deformation or compaction of the layer ($H_i - H_f$), H_f is the layer thickness after compaction, and ρ_i is the initial layer density. The input parameters for this model are: initial height (H_i), initial density (ρ_i), and deformation (ΔH_N). The output is the final density (ρ_f). After the density is estimated, MAE and the critical error based on the target density can be computed as the percentage of false positives. The advantage of this model is that it does not require any calibration before it can be used and does not depend on material or roller type. ρ_i can be either measured or estimated, more details are provided in section 7.5.

7.1.4 Machine learning models

As described in Chapter 3, machine learning classifier models, such as artificial neural networks (ANNs), Random Forest (RF), and Scholastic Gradient Descent (SGD) classifiers, can be employed to capture non-linear relationships between input and output variables. For this study, Scikit-Learn's SGD Classifiers were implemented in Python and other required modules, including Pandas, Numpy, and Seaborn, to develop the model (Van Rossum and Drake Jr 1995; McKinney 2010; Pedregosa et al. 2011; Harris et al. 2020). The entire dataset was divided into 80% training data for model development and 20% test data for model validation. The input parameters remained the same as the 1-D model (initial height, initial density, and deformation), while the two-classification output values represented i) density

more than MDD or ii) density less than MDD. These models require initial development and training with the obtained data before being deployed for prediction. It is also important to note that this method depends on the material and compactor types, meaning the model would need to be retrained if any of these parameters changed.

7.2 Materials and Test Methods

As discussed in the preceding chapter, the instrumentation and hypothesis were examined in two distinct field settings: (a) indoors (Experiment 1) and (b) outdoors (Experiment 2). Each field setting offered its own advantages and limitations. The indoor field setting of Experiment 1 allowed for testing the instrumentation and demonstrating the proof of concept for the hypothesis. It also enabled control over the environmental factors influencing data collection during the tests. Conversely, the outdoor field setting of Experiment 2 provided an opportunity to scale up the methodology to resemble the actual field conditions. This involved utilizing a larger roller than the one used in Experiment 1, as illustrated in Table 7-1. Images of the rollers can be found in Figure 7-3. Further details regarding the experimental setup are provided in the subsequent sections.

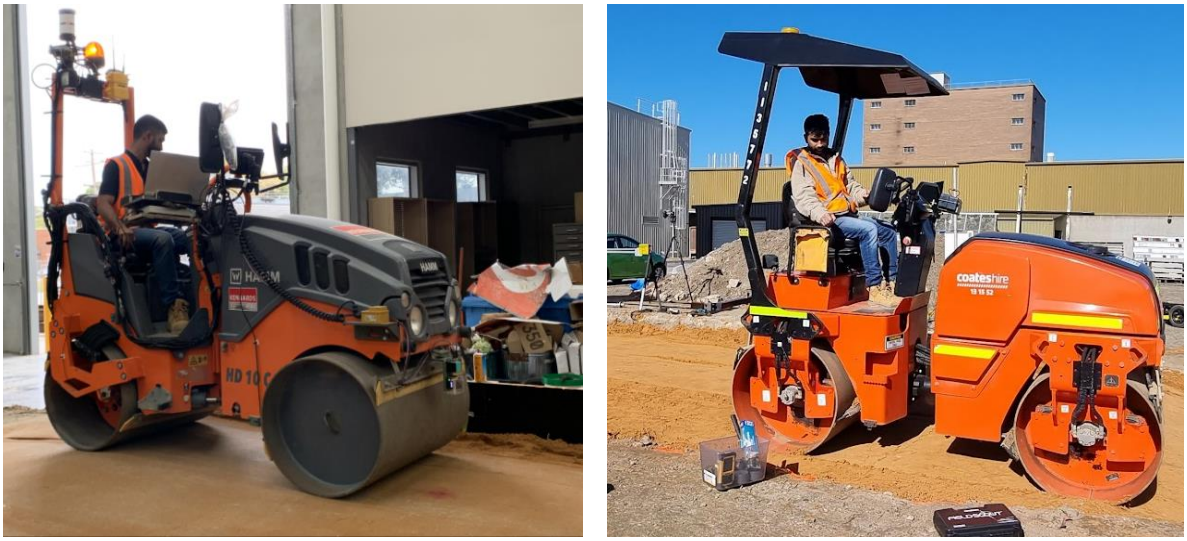

(a) (b)

Figure 7-3. Rollers used for this study (a) 1.5t roller for Experiment 1; (b) 4t roller for Experiment 2.

The material utilized for Experiment 1 was identified as sand with silty fines (referred to as Material 1). In contrast, for Experiment 2, a Class 2 UGM classified by VicRoads was employed (referred to as Material 2) which was selected as it was more representative of the

base layer of a pavement. The geotechnical properties of these materials and additional details can be found in Figure 7-4 and Table 7-2.

Table 7-1. Details about the rollers used for this study.

	Experiment 1	**Experiment 2**
Manufacturer	HAMM	DYNAPAC
Model	HD 10C VV	CC1300
Type	Articulated tandem roller with two vibratory drums	Articulated tandem roller with two vibratory drums
Total length (mm)	2260	2725
Width (mm)	1056	1450
Roller drum width (mm)	1000	1300
Drum diameter (mm)	620	802
Speed range (km/h)	0 to 11	0 to 10
Theoretical gradeability	30 % (vibration ON), 40 % (vibration OFF)	37 %
Static Mass (kg)	1670	3900
Static Drum Linear Load, front/rear (kg/cm)	8.1/8.6	14.5/15.4
Vibration frequency (Hz)	52	52
Amplitude (mm)	0.45	0.5
Centrifugal force (kN)	16	33

The test procedure for both experiments consisted of the following steps:

(a) Placing the material using a bobcat.

(b) Spreading the material manually using shovels and rakes and levelling it with a bubble level.

(c) Compacting the material using the instrumented roller.

(d) Conducting in-situ tests for material density.

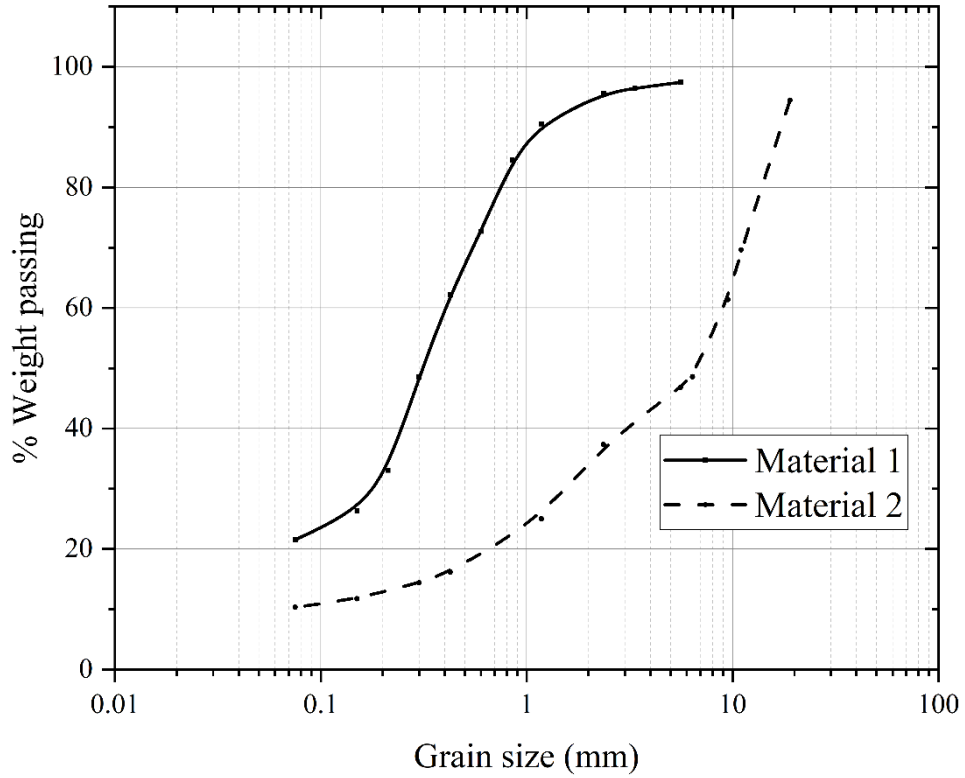

Figure 7-4. Grain size distribution of the two materials used in this study.

The detailed test procedure involved the following steps:

[Step 1] The material was conditioned to an appropriate moisture content (8% w/w) for site 1 and covered with a tarp for storage, ensuring consistent and ready-to-test material.

[Step 2] The material was placed into the test setup using a bobcat and spread as evenly as possible.

[Step 3] Shovels and rakes were used to spread the material further, followed by levelling using a large spirit level to achieve a smooth finish.

[Step 4] Before compaction, measurements were taken, including density and moisture measurements using NDG sampling.

[Step 5] The instrumentation system was checked, the signal was zeroed, and the data acquisition (DAQ) system kept running.

[Step 6] The instrumented roller was then used to compact the material, dividing the entire width (approximately three times the width of the compactor) into three lanes (A, B, and C) shown in Figure 7-5 (d).

[Step 7] The data from the instruments for each lane and pass were saved to the computer in separate files.

[Step 8] Density data from sampling (sand cone test) were utilized to determine the end of compaction. NDG tests were performed at the end of compaction for validation.

[Step 9] After compacting one layer, the material for the subsequent layer was placed, and Steps 2 to 8 mentioned above were repeated.

Table 7-2. Geotechnical properties of each material.

Geotechnical property	Material 1	Material 2	Standard
	Value	Value	
Specific gravity (G_S)	2.70	2.78	AS 1289.3.5.2 (Standards Australia 2002)
Median diameter (D_{50}) mm	0.32	6.5	AS 1289.3.6.1 (Standards Australia 2009)
Fines content (%)	20	10	AS 1289.3.6.1 (Standards Australia 2009)
MDD standard proctor (Mg/m^3)	1.96	2.28	AS 1289.5.1.1 (Standards Australia 2017)
OMC standard (%)	9.8	6.5	AS 1289.5.1.1 (Standards Australia 2017)
MDD modified Proctor (Mg/m^3)	2.08	2.35	AS 1289 5.2.1 (Standards Australia 2003)
OMC modified Proctor (%)	8	5.8	AS 1289 5.2.1 (Standards Australia 2003)
Optimum degree of saturation (S_{ropt}) (%)	70	85	AS 1289.5.1.1 (Standards Australia 2017)
USCS classification	SM	GW	AS 1289.3.6.1 (Standards Australia 2009)

7.2.1 Setup for Experiment 1

The site chosen for the experiment was an indoor facility located within the premises of Monash University. This indoor setting was selected to minimize errors arising from the outdoor environment. To create the site, a large wooden box was fabricated, measuring 7.5 m in length, 4 m in width, and 0.8 m in height. Additionally, an open area was included to accommodate the ramp for moving the roller into the box, as depicted in Figure 7-5.

The sides of the box were reinforced with bracing, as depicted in Figure 7-5(b) and (c), using wooden angle brackets spaced at 125 mm intervals. This reinforcement was implemented to ensure the safety of the box during the vibration caused by the roller during the compaction of the soil layers inside the box. Moreover, the structural capacity of the box was designed with a factor of safety exceeding 5 to enhance its stability further.

7.2.2 Results for Experiment 1

The test consisted of compacting five layers. To facilitate NDG measurements for validation, each layer was divided into three lanes (Lanes A, B, and C). Each lane was subdivided into a 1 m^2 grid area comprising five points (the edge points were not taken into consideration as the roller was not placed entirely to the edge). Consequently, the total number of data points for one layer amounted to 15. Therefore, the number of data points for the entire test encompassing five layers was 75. The vertical plastic deformation values obtained from the instrumentation are depicted in Figure 7-6.

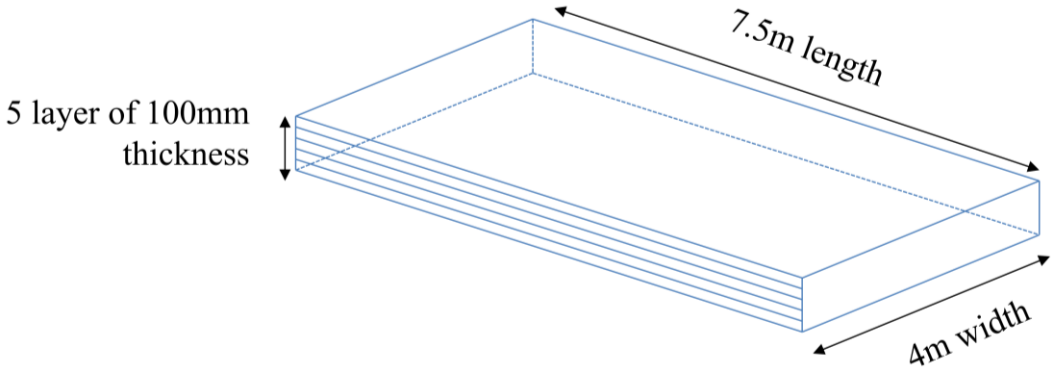

(a) Schematic diagram

(b) Fabricated Large soil box

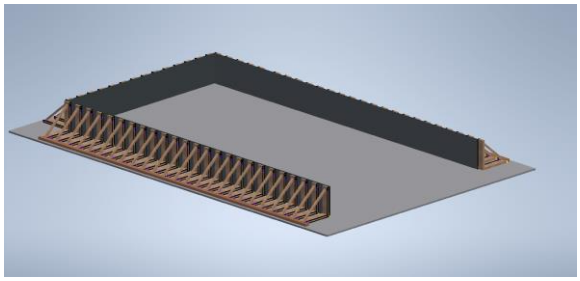

(c) AutoCAD diagram of the site

(d) Lanes A, B and C

Figure 7-5. Images of the test site used for this study.

The comparison between the measured and predicted density is illustrated in Figure 7-7, demonstrating that the predicted density yielded a remarkably low MAE of only 0.08 Mg/m^3 when employing the 1-D compaction model. The classification-based differentiation is based on the MDD, obtained from the standard compaction test, achieving a value greater than 1.96 Mg/m^3, approximately 94% of the MDD.

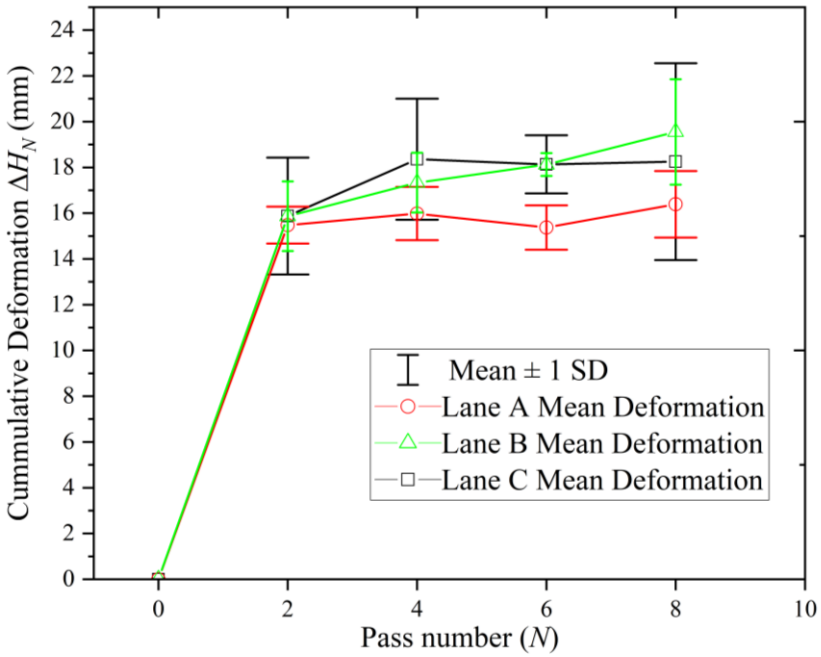

Figure 7-6. Average Deformation vs Pass Number for all the lanes for Experiment 1.

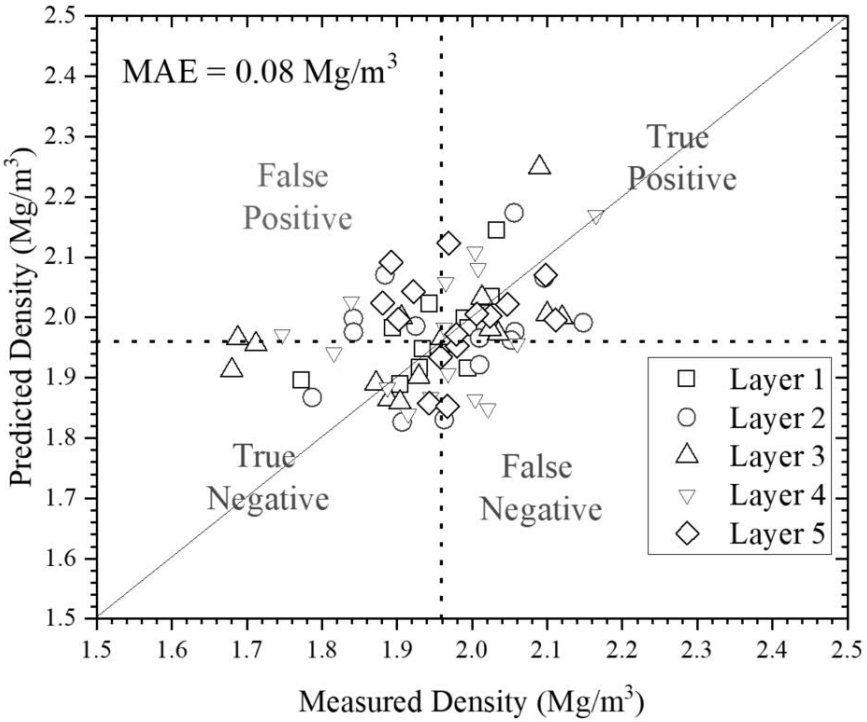

Figure 7-7. Comparison of predicted dry density using the 1-D compaction assumption from the instrumented roller and measured dry density from NDG for Experiment 1.

Regarding the 1-D model utilized, the confusion matrix comprised 29 true positives, 19 true negatives, 15 false positives, and 12 false negatives out of the 75 data points. This yielded a critical error of only 20%, indicating that the 1-D model can predict the field behaviour with reasonable accuracy, as also discussed in (Tophel et al. 2022). Nevertheless, the accuracy could be enhanced by considering a non-linear relationship.

The number of data points for the SGD classifier in the confusion matrix was 29 true positives, 25 true negatives, 12 false positives, and 9 false negatives. The aforementioned critical error for the SGD classifier amounts to only 16%, indicating a 20% improvement compared to the 1-D model. The confusion matrix for both methodologies is presented in Table 7-3. The heat maps of the area are shown in Figure 7-8. The red area shows a compacted area density of less than the target density, and the green area shows a compacted area density of more than the target density.

Table 7-3. Comparison of the density predictions from the 1-D and ML models as a confusion matrix.

		Predicted Values	
		Positive	Negative
Actual Values	True	29	12
	False	15	19

(a) 1-D model

		Predicted Values	
		Positive	Negative
Actual Values	True	29	09
	False	12	25

(b) ML model

7.2.3 Setup for Experiment 2

As mentioned in Chapter 6, Experiment 1 employed two triangulation laser sensors. One sensor was attached in front of the front drum, while the other was attached to the rear. In contrast, Experiment 2 utilized a more advanced roller instrumentation system that incorporated three triangulation laser sensors at the front and three at the back. This was done to mitigate the error associated with using only one sensor before and after the roller, allowing for accurate measurement of deformations over the width of the roller caused by a larger roller and larger material particle size (Material 2), as depicted in Figure 7-9. The test area for Experiment 2 measured 8 m in length, 5 m in width, and 0.8 m in depth, surpassing the dimensions of Experiment 1. An image of the test area can be seen in Figure 7-10. The procedure followed for this experiment was identical to that of Experiment 1, as was described in the above section.

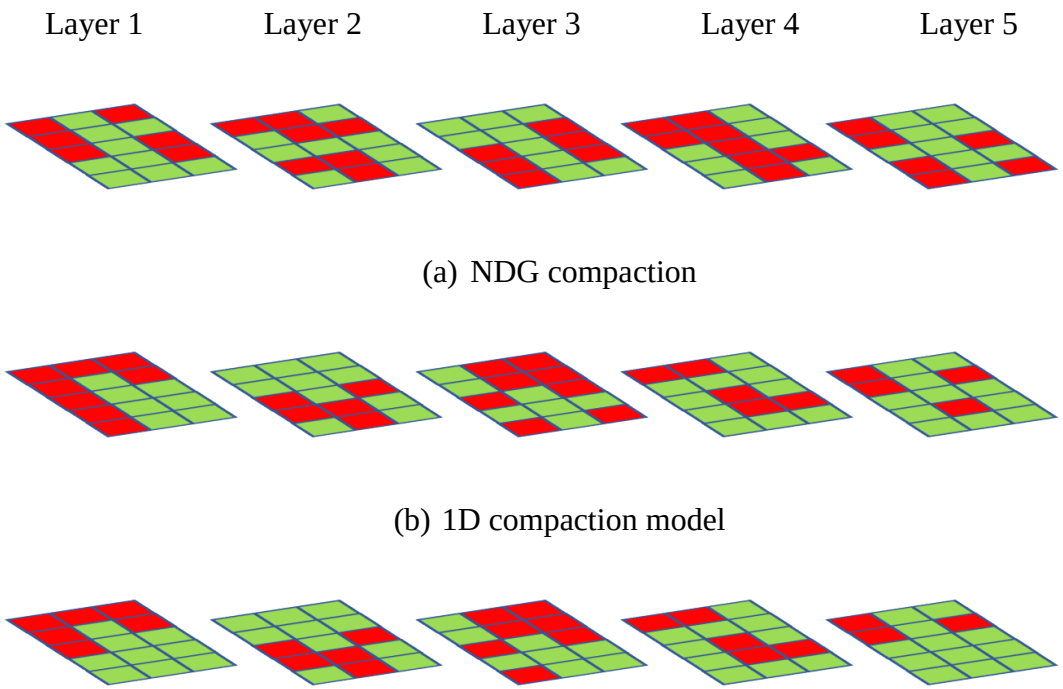

(a) NDG compaction

(b) 1D compaction model

(c) SGD classifier model

Figure 7-8. Heatmaps of the area characterized using (a) NDG compaction; (b) 1D compaction model; (c) SGD classifier model.

Figure 7-9. Three laser sensors are attached to the back of the roller.

Figure 7-10. Test setup for Experiment 2.

7.2.4 Results for Experiment 2

The advantages of using multiple sensors are illustrated in Figure 7-11(a), where it can be observed that using multiple sensors led to a reduction in standard deviation. Furthermore, the standard deviation decreased with increasing passes as the surface became smoother. However, because the mean deformation reduces, the variance increases with number of cycles (Figure 7-11 (b)). Nevertheless, due to the use of multiple sensors, the variance also reduced. The comparison between the measured and predicted density is illustrated in Figure 7-12, demonstrating that the predicted density yielded a remarkably low MAE of only 0.06 Mg/m^3 when employing the 1-D compaction model, being lower than that obtained in Experiment 1 whereas, Figure 7-13 shows the heatmap.

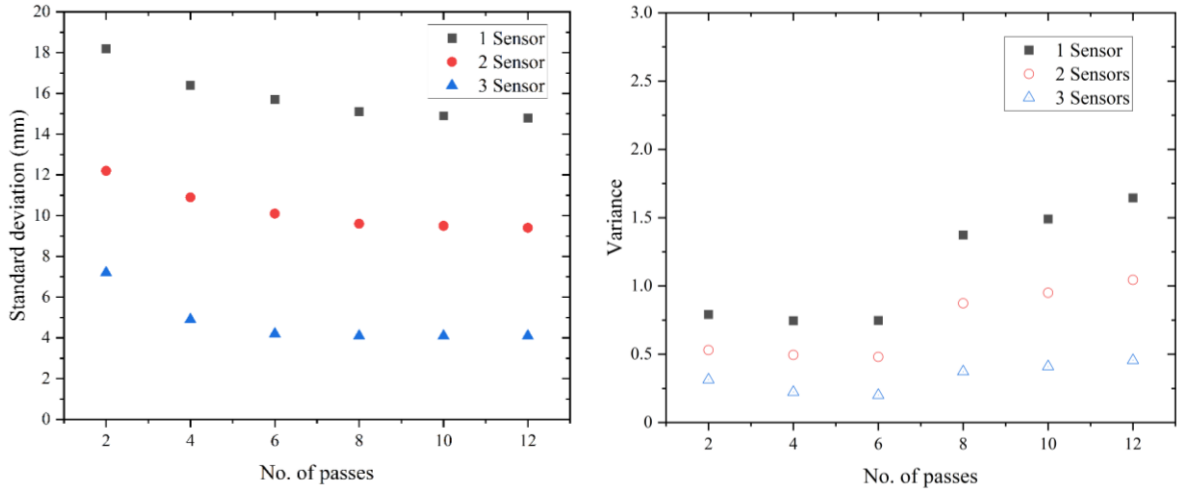

(a) (b)

Figure 7-11. (a) Standard deviation and (b) variance in the deformation measurement with the number of passes.

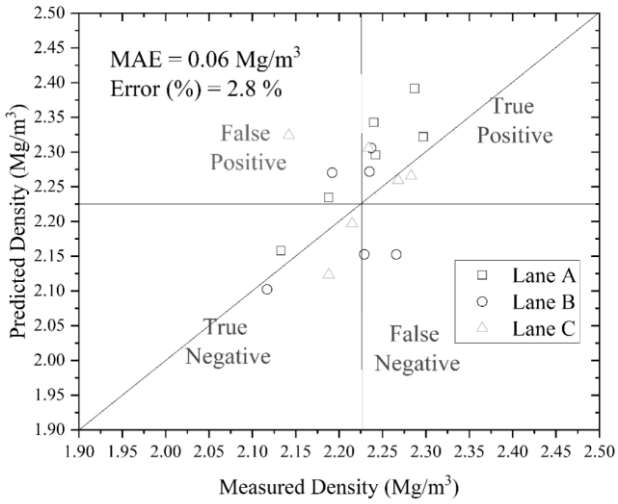

Figure 7-12. Comparison of predicted dry density using 1-D compaction assumption from the instrumented roller and measured dry density from NDG for Experiment 2.

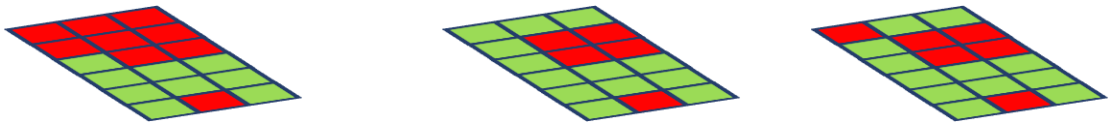

(a) (b) (c)

Figure 7-13. Heatmaps of the area due to (a) NDG compaction; (b) 1D compaction model; (c) SGD classifier model for Experiment 3.

Regarding the 1-D model utilized, out of the 18 data points, the confusion matrix comprised 9 true positives, 4 true negatives, 3 false positives, and 2 false negatives. This indicates a critical error of only 16%, indicating again that the 1-D model can predict field behaviour with reasonable accuracy.

The number of data points for the SGD classifier in the confusion matrix was 9 true positives, 6 true negatives, 3 false positives, and 0 false negatives. The aforementioned critical error for the SGD classifier amounts to only 16%, indicating that both methods had the same error; however, the SGD classifier could classify more true positives and negatives than the 1D model.

7.3 Acceptance criteria based on statistics

Road building materials, whether natural or manufactured, are not perfectly uniform. This means their physical properties can vary. Therefore, statistical form of specification is provided to replace the traditional form of specification in which density requirements were required to be not less than some nominated/specified value. Statistical form of specification recognises that a proportion of works may have a density less than the specified value and still the work can be considered satisfactory (Main Roads 2008).

In the statistical form of specification, a characteristics density (R_c) is specified which is used to decide if the work is satisfactory or not. It can be calculated based on the mean density $(\overline{x})$, standard deviation (s) and a multiplier (k) as:

$$R_c = (\overline{x} - ks) \geq L, \tag{14}$$

where L is the specification limit. The multiplier (k) can be calculated based on total number of tests (n) carried out, producers' risk (α) and proportion defective (p) as following:

$$k_\alpha = \frac{k_p - k}{\left(\frac{1}{n} + \left(\frac{k^2}{2(n-1)}\right)\right)^{0.5}}, \tag{15}$$

where k_α and k_p is the standard normal variate corresponding to the producer's risk (α) and proportion defective respectively. The values of α, p, and n are recommended by road authorities. One such example is described from (Main Roads 2008) recommends number of test per lot (n) as 6, α of 10% and p of 10% and 15% for freeways and highways respectively. Using Equation 22 with the value, k is calculated as 0.72 and 0.5 for freeways and highways respectively.

The value of k decides how stringent is the specification limit and higher the value of k, more stringent is the specification. A parametric study was conducted to see the effect of number of tests on proportion defective (p) as shown in Figure 7-14. It can be seen from the figure that if we conduct more tests in a lot, the allowed proportion defective can be higher for both freeways and highways. Therefore, this study even though has 16% false positive can be accepted as it measures density of the entire compacted area.

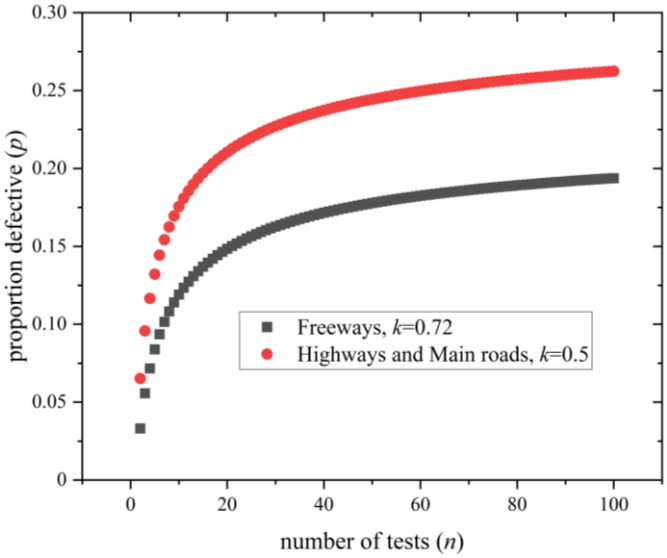

Figure 7-14. Parametric study on proportion defective (p) with number of tests (n) for different values of multiplier (k).

7.4 Application of TGML to remove noise from the deformation measurement

The test plastic deformation ΔH_N measured in the field contains noise because of uncertainties involved with testing, measurement, equipment limitations, and human error. Therefore, the raw value of the ΔH_N was de-noised using the TGML3 technique developed in Chapter 4 to smoothen the behaviour. After the deformation values were de-noised, the corrected deformation data was used to estimate the density using either a 1-D or ML-based model. As discussed in Chapter 4, in TGML3, the artificial neural network (ANN) model is informed about the noise using a restriction relationship/equation as an input to the training. The restriction relationship/equation represents ΔH_N as increasing monotonically; or in other words, with an increase in total passes (N), ΔH_N always increases, which can be written as $\Delta H_{N+1} - \Delta H_N > 0$. The regular loss function of the ANN model was modified by adding a denoising loss function (L_{DN}). The denoising loss function depends on a difference in the predicted deformation as a pair (J_N), which was calculated as

$$J_N = \Delta H_N - \Delta H_{N+1} \quad (16)$$

To enforce the restriction relationship/equation, any positive value of J_N is defined as a noise in the measurement, and thus L_{DN} was calculated as a non-zero occurrence of a Rectified Linear Unit of the difference of the predicted deformation, ReLU(J_N), summed over all the

cycles, then multiplied by a hyperparameter λ_{DN}, which was decided using trial and error such that

$$L_{DN} = \lambda_{DN} \sum_{N=1}^{N} \mathrm{ReLU}(J_N). \tag{17}$$

The technique described above is demonstrated for Experiment 1 data as an example where all the lanes' measured deformation patterns did not increase monotonically (see Figure 7-6). TGML3 was used for deformation data to get the corrected deformation measurements. For demonstration, Lane B deformation data is presented in Figure 7-15. Figure 7-15 (a) shows the predictions of TGML3 when only 6 passes of data are collected, whereas Figure 7-15 (b) shows the correction after 8 passes. This was done to demonstrate the recursive correction in deformation data. As the data are collected, they will be retrained recursively (also known as online training) to get better predictions.

After deformation correction, the data obtained in Experiment 3 were used to predict the density using the 1D compaction model in Equation (13). It was found that the prediction improved slightly with an improved MAE of 0.07 Mg/m^3 compared to MAE 0f 0.08 Mg/m^3 without correction.

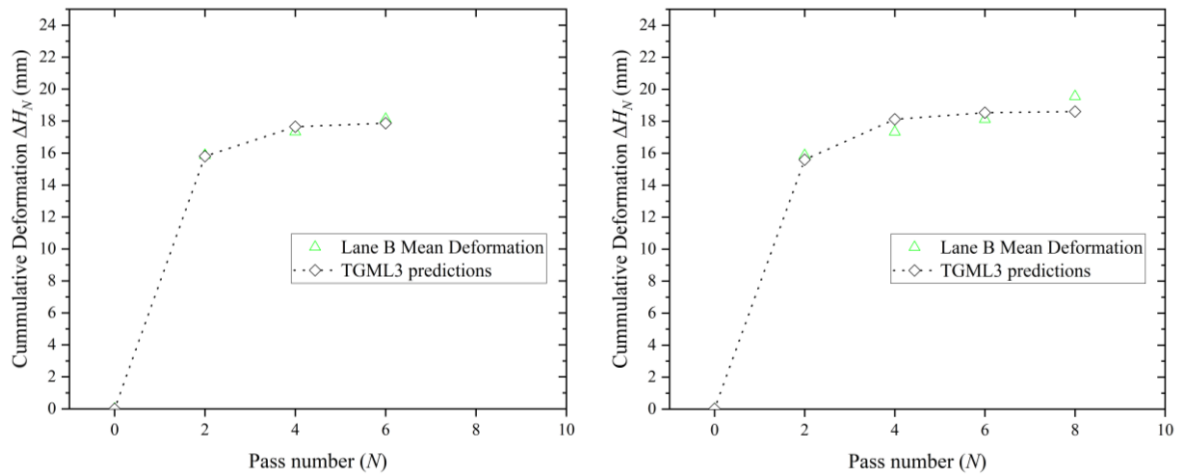

(a) (b)

Figure 7-15. TGML3 predictions for Lane B deformation (a) after 6 passes; (b) after 8 passes.

7.5 Use of constitutive model developed to estimate initial density

The 1D compaction model and SGD classifier model described above both require the input of initial density (ρ_i), measured using the NDG here. But when NDG tests cannot be carried out before the compaction starts due to restrictions in entering the test site, two possible methodologies can be followed.

1. The initial density is approximately determined by a lookup table for common materials used for road construction. Such a lookup table can be generated by testing the material in the laboratory by subjecting the materials to nominal stress conditions. In Chapter 5, materials were placed and spread manually, and then a nominal load of 1 kN was applied. It was found that even when trying to maintain the uniform condition, the initial density or void ratio varied considerably, being from 0.38 to 0.6 (see Chapter 4, Fig. 7). Therefore, the estimation of initial density using this method can be very erratic.
2. Estimate the initial density using a model such as that developed in Chapter 5, which provides total plastic deformation (ΔH_N) as a function of initial height (H_i) and compactor force/load (F) with model parameters (α, β, C_1 and m) and number of cycles/pass (N) as

$$\Delta H_N = H_i C_1 (1 + \beta m) ln \left(1 + \frac{1}{1 + \beta m} \left(\frac{4F}{\pi L \alpha}\right)^m N\right). \quad (18)$$

Recalling from Chapters 4 and 5, the model parameters (α, β, and C_1) were constant for a given material at one moisture content, whereas m was found to be a linear function of the initial void ratio (e_0) or initial density. The model was trained with Lanes A and C data of Experiment 1 to evaluate the model parameters listed in Table 7-4. The model parameter m was also found to be a linear variation of initial density similar to what was found in Chapters 5 and 6 and is shown in Figure 7-16.

Table 7-4. Model Parameters for Lanes A and C.

Model parameter	Value
C_1	0.010
α	0.83
β	0.16

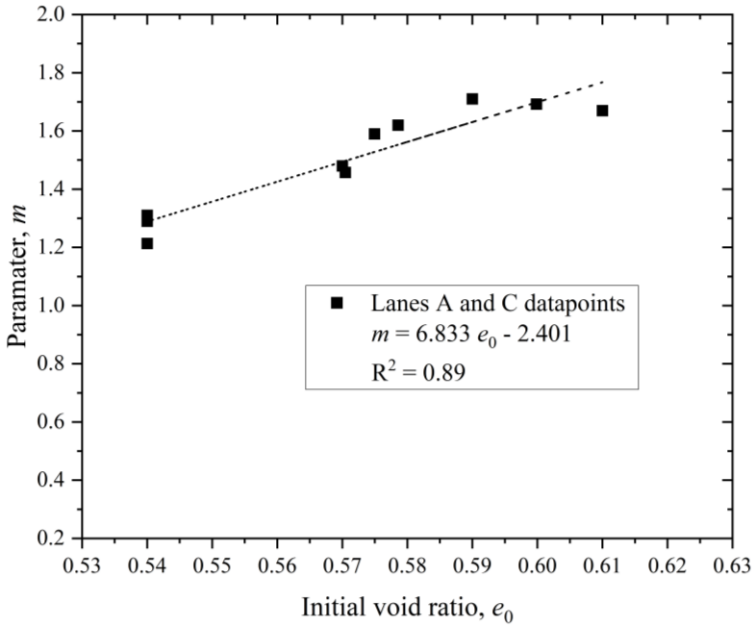

Figure 7-16. Variation of model parameter m with initial void ratio (e_0).

The linear relationship between m and e_0 was used for Lane B to evaluate the value of e_0,which was then used to calculate the density instead of the initial density using the NDG. Using this approach, it was found that density could be estimated with MAE of 0.1 Mg/m^3. This error was higher than the density evaluated using the NDG data; however, it removes the requirement for NDG tests before compaction.

7.6 Application of this study to accurate estimation of density during compaction

7.6.1 With test/correlation strips

The models' training can be carried out in a test strip/correlation strip before a large compaction area is planned, using, for example, one roller width and around 10 m in length). The correlation strips can also be used to develop the theoretical model and evaluate the model parameters measured/determined experimentally using each material type and compactor in the test strip/correlation strip, for example, one roller width and around 10 m in length. The developed model can then be used to obtain a better density estimate; however, this method would be expensive as it involves establishing a prior small-scale testing site. The overall methodology is shown in Figure 7-17. In step 3, if the initial density using the NDG is not possible, the methodology described above can approximate the initial density of the material.

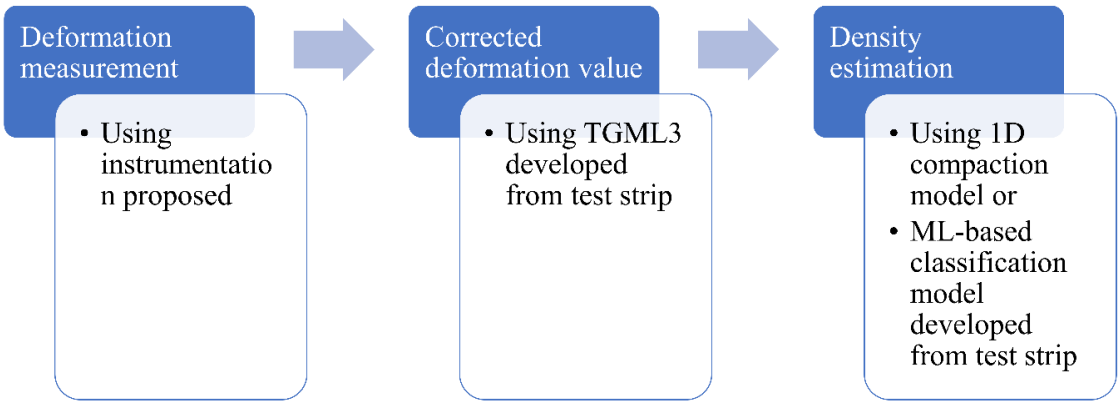

Figure 7-17. Flow chart of the density estimation with test/correlation strip.

7.6.2 Without test/correlation strips

If the project is small, having a test strip could be costly; therefore, as mentioned in the previous section, the density can be estimated using a recursive estimation of parameters as the data are collected. This methodology would be cheaper but less accurate and more computationally expensive as it involves online training. The overall flow chart is shown in Figure 7-18. Similar to the test strip, in step 3, if the initial density using the NDG is not possible, the methodology described above can approximate the initial density of the material.

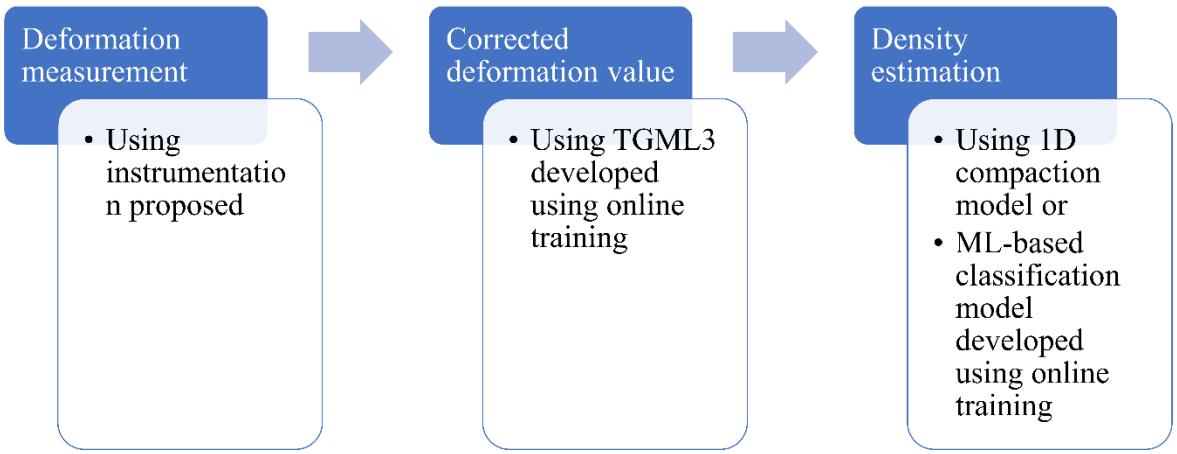

Figure 7-18. Flow chart of the density estimation without test/correlation strip involving online training.

7.7 Summary

Building upon the previous chapter's discussion on measuring deformation during compaction and reducing data noise, methods for estimating density based on obtained deformation data were presented and an overview of the experimental procedure used in field testing was provided, including details on materials and rollers.

The importance of estimating density during compaction using advanced instrumentation was emphasized, with different approaches (1-D compaction and ML-based classification model) to convert deformation measurements into density values were discussed. Moreover, the potential of a previously developed model to enhance density estimation accuracy was highlighted.

Two distinct field settings were described: indoor (Experiment 1) and outdoor (Experiment 2). Experiment 1 focused on testing instrumentation and validating hypotheses. In contrast, Experiment 2 aimed to replicate real field conditions on a larger scale with two different materials.

In Experiment 1, a comparison between measured and predicted density demonstrated a low mean absolute error (MAE) of 0.08 Mg/m^3 using the 1-D compaction model. A classification-based approach was used to differentiate density based on the Modified Proctor Maximum Dry Density (MDD), achieving a 64% accuracy with a simplified 1-D model. Minimizing false positives in density prediction was emphasized, suggesting a non-linear relationship be considered for improved accuracy. In Experiment 2, using multiple sensors yielded a better accuracy even with material with larger particle size. Using the 1-D model, the accuracy, MAE of 0.06 Mg/m^3 was observed. Instrumentation details and the benefits of using multiple sensors during compaction were also discussed. Figure 7-11illustrated the reduction in standard deviation and variation achieved with multiple sensors and the smoothing effect from increased passes.

Overall, the chapter demonstrated the ability to estimate density during compaction using advanced instrumentation with various methodologies, models, and field-testing procedures. To utilize the approach developed in this chapter, it is recommended to incorporate a test strip or correlation strip (with a width equivalent to that of one roller and a length of approximately 10m) before compaction over a larger area to get higher accuracy. This test strip serves the purpose of developing the model specific to the material conditions at the site. Once the model

has been successfully developed and validated, it can be employed for the actual compaction process. However, if implementation of the test strip is not possible, TGML3 correction or recursive estimation of model parameters can be used to estimate density with a slight reduction in accuracy.

Part 5: Implications and Conclusions

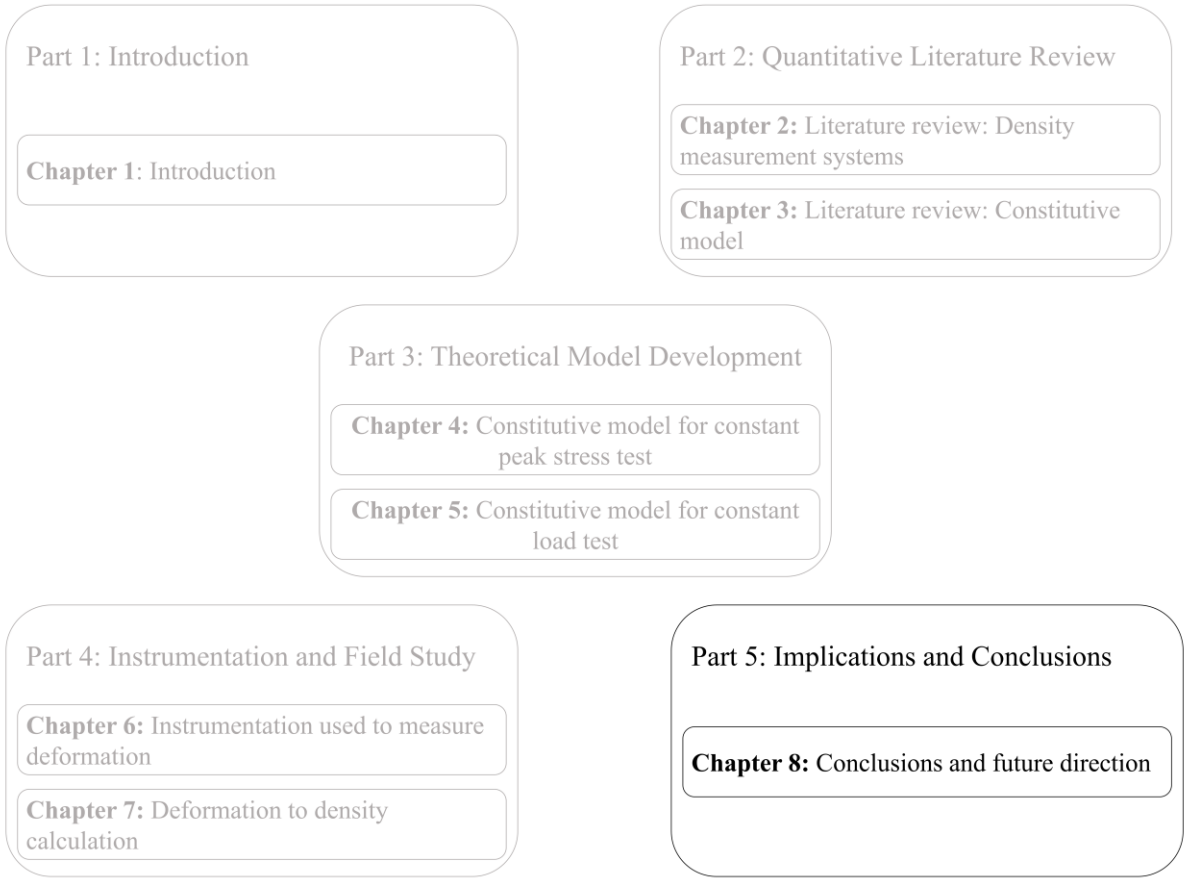

Chapter 8 Conclusions and future direction

The thesis contributed to the field of compaction by presenting a novel methodology for estimating density during the compaction of geomaterials for a smoothed drum roller. The research included theoretical development and practical validation through experimental investigations. The proposed methodology utilizes non-contact distance sensors, orientation sensors, and data processing algorithms to measure accurate geomaterial properties during compaction. The system for estimating density during compaction includes the following components:

- A distance sensor system for continuously measuring the surface deformation (Δ_N) of a geomaterial portion during compaction without physical contact.
- A motion/orientation sensor system is mounted on the compactor to synchronously measure the motions/orientations of the platform with the deformation measurements.
- An electronic processing system that incorporates the motion/orientation signals to generate corrected deformation estimates.
- A geolocation unit which measures the geolocation (latitude and longitude) of the geomaterial portion synchronously with the deformation measurements.
- An electronic processing system that receives deformation signals from the distance sensor system to generate numerical estimates of the density based on the measured deformation and a constitutive relationship or model.

8.1 Implications of this study

The accurate measurement of deformation during compaction allows the estimation of density proximally or non-destructively and in real-time. The suitability of this methodology has been demonstrated for road construction; however, this method can easily be extended to other activities involving compaction, such as earthworks in landfills and foundations of buildings and bridges. Other advantages and implications of this study include:

a. The density estimation covers the entire area to be assessed rather than at discrete locations;

b. The approach can be used with either a vibratory or static roller as the measurement system and the methodology has the capability to reduce the noise coming from vibration;

c. Alerts are provided the user about problematic or under-compacted areas based on the geomaterial layer density, e.g., when used for QA/QC purposes.

d. The system indicates compliance with end-result specifications or method specifications: the end-result specifications are relevant when the compaction takes place until the material has achieved the required density or value of another geomaterial layer property. If measurements of the geomaterial layer properties are not possible because of very large size materials being present, the method specification is relevant, which requires compaction until a selected compaction (deformation) threshold is reached—the system and method described herein improves on previous methods that rely on contractors visually checking whether the deformation has reached a threshold value;

e. Indicates compliance with performance-based specifications: the performance-based specification necessitates density as a critical parameter, and therefore, this study has the potential to transform current design practice and thus make present intelligent compaction 'truly' intelligent.

f. Indicates compliance during 'proof rolling', which is carried out in some parts of the world after the end of compaction to check if the material has been compacted sufficiently: proof rolling involves loading the material manually using a water truck or a suitable vehicle and checking the deformation visually. The system and method described herein may improve on such methods.

In addition to the advantages above, the deformation measurement system can also be used to estimate other geomaterial layer properties (layer thickness, stiffness, modulus, and energy imparted to geomaterial).

8.1.1 Layer thickness measurement

The layer thickness information after a particular pass N (H_N), can be estimated using initial layer thickness (H_i) and a total deformation value until pass N (ΔH_N) as

$$H_N = H_i - \Delta H_N. \tag{19}$$

8.1.2 Stiffness measurement

Different deformations measured during compaction can be used to estimate the stiffness during compaction as illustrated in Figure 6-1. Two types of stiffness values (K_N) – secant

stiffness value ($K_{N,secant}$) and elastic stiffness value ($K_{N,elastic}$) − of the material at a particular pass N can be calculated with the information of the applied force (F) due to the compactor (which includes static and vibratory load), and either the total ($\Delta_{N,total}$) or elastic ($\Delta_{N,elastic}$) deformation during pass N according to:

$$K_{N,secant} = \frac{F}{\Delta_{N,total}}, \tag{20}$$

$$K_{N,elastic} = \frac{F}{\Delta_{N,elastic}}. \tag{21}$$

8.1.3 Modulus measurement

To calculate/generate/estimate/measure the modulus values, e.g., the two moduli of the material at a particular pass N (M_N) − secant modulus value ($M_{N,secant}$) or elastic modulus value ($M_{N,elastic}$) − can be calculated using stress applied by the compactor (σ_Z) and the model developed in Chapter 4 from the total and elastic deformation during pass N ($\Delta_{N,total}$, $\Delta_{N,elastic}$) as

$$M_{N,secant} = \frac{\sigma_Z}{(\frac{\Delta_{N,total}}{H_N})}, \tag{22}$$

$$M_{N,elastic} = \frac{\sigma_Z}{(\frac{\Delta_{N,elastic}}{H_N})}. \tag{23}$$

8.1.4 Total energy imparted by a vibratory roller to the ground

The total energy imparted to the ground (E_{total}) due to a roller, can be represented as a sum of three terms: rotational energy (E_1), static energy (E_2), and vibrational energy (E_3) as

$$E_{total} = E_1 + E_2 + E_3. \tag{24}$$

The free body diagram of a drum in contact with the ground is shown in Figure 8-1, with the roller movement details shown in Figure 8-2.

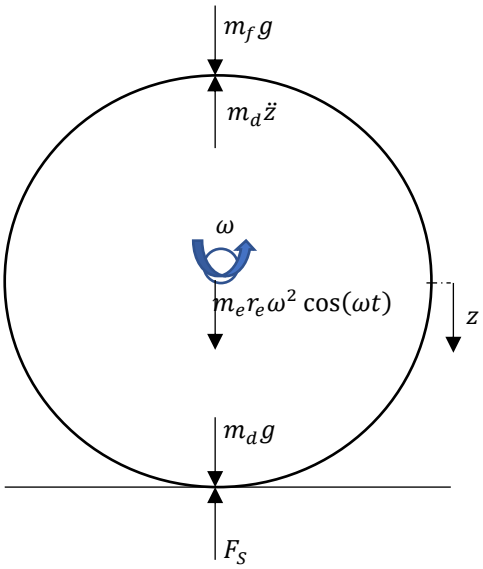

Figure 8-1. Simplified free body diagram for soil-drum interaction (modified after (Anderegg and Kaufmann 2004)).

The terms shown in the figures are defined as:

a. F_S = soil-drum interaction force (N);

b. m_d = drum mass (kg);

c. m_f = frame mass (kg);

d. m = total mass $\left(m_f + m_d\right)$ (kg);

e. $\omega = 2\pi f$ = circular vibration frequency (rad/s);

f. f = frequency of excitation (Hz);

g. z = displacement of drum (m);

h. $\ddot{z}$ = acceleration of drum (m/s^2);

i. $m_e r_e$ = eccentric moment of unbalanced mass (kg-m);

j. t = time (s);

k. g = gravitational acceleration (9.81 m/s^2);

l. V = linear velocity (m/s);

m. Δl = travel width (m);

n. r=radius of the drum (m);

o. I = moment of inertia $\frac{1}{2}mr^2$ (kg-m^2); and

p. Δ_N = change in layer thickness (deformation).

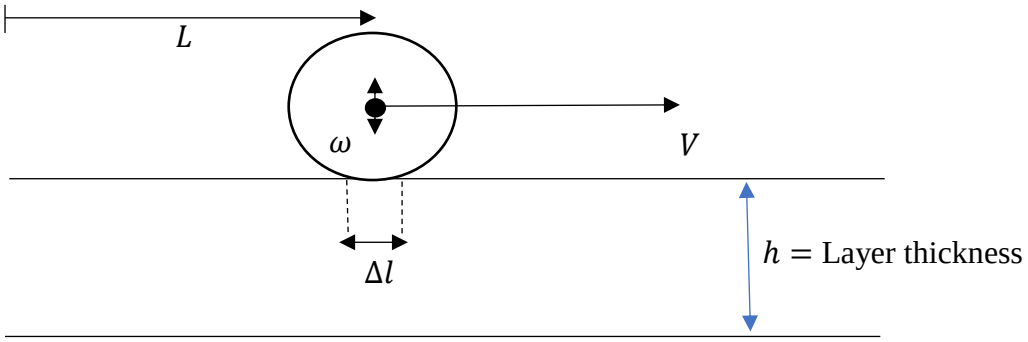

Figure 8-2. Roller movement details.

The energy contributions rotational energy (E_1), static energy (E_2), and vibrational energy (E_3) is written as:

$$E_1 = \left(\frac{\frac{1}{2}IV^2}{r^2} + \frac{1}{2}mV^2\right) \times \frac{\Delta l}{2\pi r} + mg\Delta_N f\frac{\Delta l}{V} \quad (25)$$

$$E_2 = \left(mg + \frac{1}{2}m_e r_e \omega^2\right) \times zf\frac{\Delta l}{V} \quad (26)$$

$$E_3 = \left(\frac{1}{2}m_e r_e \omega^2\right) \times \Delta_N f\frac{\Delta l}{V}. \quad (27)$$

8.2 Conclusions

Density, a gravimetric parameter, cannot be measured without taking a sample; hence, most tests are intrusive. Moreover, the commonly performed NDG test emits harmful rays, and so appropriate certification is needed to execute such a test. Sampling and performing the test is time-consuming and thus seen as a drawback. Therefore, the need for a proximal density estimation methodology in the field arises. The method would allow the contractor or the field practitioner to asses compaction quality in real-time.

The soil density measurement involves collecting a physical sample and then obtaining the value by measuring the mass and volume collected from the field. Density measurement tests take time and often hinders the contractor who wants to compact another layer of soil as soon as possible, because delaying means paying extra money for the equipment and labour. This drawback has led to the development of other QA criteria for estimating the earthwork quality; one of them is modulus-based QA. Modulus-based QA is quicker than density measurement and is thus advocated to be superior to density-based QA. The modulus, considered to have a unique and direct correlation with density, is considered to replace the density measurement; however, it has been found that the correlation between density and modulus is not unique, depending also on the water content of the sample.

This study proposed a methodology where the density can be measured in real-time by using surface deformation measurements during compaction and then correlating it to material density. This study was a proof of concept for the proposed methodology. The results showed that measuring the density with high accuracy is possible. Two models, 1-D and ML, were evaluated to estimate the density from measured deformation. It is shown that the nonlinear ML model was superior to the 1-D model by 20%; however, the 1-D model also yielded a satisfactory result. The error in density estimation could be attributed to the limitation of the sensor's accuracy and measurement error from NDG. In future, the accuracy can be improved by using advanced sensors, more sophisticated analytics and validation through field trials.

8.3 Future direction

Based on the research in this thesis, several potential future directions could be pursued:

a. Advanced Sensor Technology: Further advancements in sensor technology for distance measurement could enhance the accuracy and capabilities of the proposed methodology. Exploring new sensor designs, improved measurement techniques, and higher precision sensors with measuring the small deformation during the end of compaction at faster rate could lead to more accurate density estimations during compaction.
b. Field Trials and Validation: Conducting extensive field trials to validate the proposed methodology in different real-world construction scenarios would be beneficial. This would involve testing the system under various soil conditions, compaction equipment, and construction practices to ensure its effectiveness and reliability.
c. Expansion to Other Geomaterial Properties: Building upon the success of estimating density, the methodology could be extended to estimate other important geomaterial properties. For example, investigating the correlation between deformation measurements and parameters such as shear strength, permeability, or moisture content could provide valuable insights for construction and quality control.
d. Integration with Intelligent Compaction: Intelligent compaction techniques involve using advanced technologies to optimize the compaction process. Integrating the proposed methodology with intelligent compaction systems could enhance their capabilities and provide real-time feedback on compaction quality. The data acquired from field trials, there's potential to delve deeper into the realm of machine learning to enhance the understanding of Intelligent Compaction (IC). Leveraging this rich dataset, exploration into machine learning models that juxtapose parameters like ICMV against deformation measurements is feasible. Such an approach might bridge the uncertainties associated with traditional IC density estimations. Although this avenue wasn't covered in the current scope of the thesis, it signifies a promising direction for future research. Subsequent investigations could focus on developing and validating these machine learning models, potentially offering a more refined and accurate IC methodology.
e. Development of Standard Guidelines: Collaborating with industry organizations, regulatory bodies, and researchers to standard guidelines should be developed for implementing the proposed methodology. Establishing standardized protocols, calibration procedures, and acceptance criteria would ensure consistent and reliable

application of the methodology in practice.

f. Cost-Effectiveness Analysis: Conducting a comprehensive cost-effectiveness analysis of the proposed methodology compared to traditional density measurement methods would be useful. Evaluating the potential savings in time, resources, and labour costs could provide a strong economic justification for adopting the new approach.
g. Optimization Algorithms: Exploring advanced data processing algorithms and machine learning techniques could improve the accuracy and efficiency of density estimation. Developing algorithms that handle complex soil behaviours and variations would enhance the methodology's robustness and applicability.
h. Integration with Construction Management Systems: Integrating the proposed methodology with construction management systems and software could streamline data collection, analysis, and reporting processes. This integration would facilitate seamless communication and decision-making during compaction operations.
i. Collaboration and Knowledge Sharing: Encouraging collaboration among researchers, practitioners, and industry stakeholders would foster knowledge sharing and exchange of best practices. This could lead to further advancements in compaction techniques and the broader field of geotechnical engineering.

By pursuing these future directions, the proposed methodology would continue to evolve, leading to improved compaction practices, enhanced quality control, and more efficient construction processes in geotechnical engineering.

References

Abu-Farsakh MY, Nazzal MD, Alshibli K, Seyman E (2005) Application of Dynamic Cone Penetrometer in Pavement Construction Control. Transp Res Rec J Transp Res Board 1913:53–61. https://doi.org/10.1177/0361198105191300106

Allen JJ, Thompson MR (1974) Resilient response of granular materials subjected to time dependent lateral stresses. Transp Res Rec 1–13

Alonso EE, Pinyol NM, Gens A (2013) Compacted soil behaviour: Initial state, structure and constitutive modelling. Partial Satur Compact Soils Geotech Symp Print 2011 3–18. https://doi.org/10.1680/geot.11.P.134

American Portable Nuclear Gauge Association (APNGA) (2009) American Portable Nuclear Gauge Association Manual

An Z, Liu T, Zhang Z, et al (2020) Dynamic optimization of compaction process for rockfill materials. Autom Constr 110:103038. https://doi.org/10.1016/j.autcon.2019.103038

Anderegg R, Kaufmann K (2004) Intelligent Compaction with Vibratory Rollers: Feedback Control Systems in Automatic Compaction and Compaction Control. Transp Res Rec J Transp Res Board 1868:124–134. https://doi.org/10.3141/1868-13

Anderson DM, Ehni WJ, Lundstrom J (2001) Electrical Density Gauge Replacement For Nuclear Density Gauge. In: 14th EEGS Symposium on the Application of Geophysics to Engineering and Environmental Problems. European Association of Geoscientists & Engineers

Berney ES, Kyzar JD (2012) Evaluation of Nonnuclear Soil Moisture and Density Devices for Field Quality Control. Transp Res Rec J Transp Res Board 2310:18–26. https://doi.org/10.3141/2310-03

Bishop AW (1959) The principle of effective stress. Tek Ukebl 39:

Bodin D, Moffatt M, Jameson G (2013) Development of a Wheel-tracking Test for Rut Resistance Characterisation of Unbound Granular Materials. Austroads Publ AP-T240-13

Borja RI (2006) On the mechanical energy and effective stress in saturated and unsaturated

porous continua. Int J Solids Struct 43:1764–1786. https://doi.org/10.1016/j.ijsolstr.2005.04.045

Braspenning PJ, Thuijsman F, Weijters AJMM (1995) Artificial neural networks: an introduction to ANN theory and practice. Springer Science & Business Media

Brown SF, Hyde AFL (1975) Significance of cyclic confining stress in repeated-load triaxial testing of granular material. Transp Res Rec 537:. https://doi.org/10.1016/0148-9062(76)90013-9

Brzeziński K, Ciężkowski P, Kwaśniewski A, et al (2022) Soil compaction monitoring via photogrammetric settlement measurement – Feasibility study. Meas J Int Meas Confed 205:. https://doi.org/10.1016/j.measurement.2022.112164

Caicedo B (2019) Geotechnics of Roads: Fundamentals. CRC Press, Taylor & Francis Group

Cao L, Zhou J, Li T, et al (2021) Influence of roller-related factors on compaction meter value and its prediction utilizing artificial neural network. Constr Build Mater 268:121078. https://doi.org/10.1016/j.conbuildmat.2020.121078

Chen L, Ghorbani J, Zhang C, et al (2021) A novel unified model for volumetric hardening and water retention in unsaturated soils. Comput Geotech 140:104446. https://doi.org/10.1016/j.compgeo.2021.104446

Chong SH, Santamarina JC (2016) Sands subjected to repetitive vertical loading under zero lateral strain: Accumulation models, terminal densities, and settlement. Can Geotech J 53:2039–2046. https://doi.org/10.1139/cgj-2016-0032

Commuri S, Mai AT, Zaman M (2011) Neural network-based intelligent compaction analyzer for estimating compaction quality of hot asphalt mixes. J Constr Eng Manag 137:634–644. https://doi.org/10.1061/(ASCE)CO.1943-7862.0000343

Coussy O (2011) Mechanics and physics of porous solids. John Wiley & Sons

Department of Infrastructure, Planning, and Logistics N Testing Field Compaction for Conformance. NTCP 1021

Depina I, Jain S, Mar Valsson S, Gotovac H (2021) Application of physics-informed neural networks to inverse problems in unsaturated groundwater flow. Georisk Assess Manag

Risk Eng Syst Geohazards 0:1–16. https://doi.org/10.1080/17499518.2021.1971251

Dutta TT, Kodikara J (2022) Evaluation of unbound/subgrade material rutting and resilient behaviour based on initial density and saturation degree. Transp Geotech 35:100782. https://doi.org/10.1016/j.trgeo.2022.100782

EN BS (2004) 13286-7 (2004) Unbound and Hydraulically Bound Mixtures–Cyclic Load Triaxial Test for Unbound Mixtures. Br Stand Institute, UK

Foroutan M, Ghazanfari E (2018) Implementation of Intelligent Compaction (IC) for Pavement Construction in Vermont

Géron A (2017) Hands-on machine learning with Scikit-Learn and TensorFlow : concepts, tools, and techniques to build intelligent systems. O'Reilly Media

Ghorbani J, Nazem M, Kodikara J, Wriggers P (2021) Finite element solution for static and dynamic interactions of cylindrical rigid objects and unsaturated granular soils. Comput Methods Appl Mech Eng 384:113974. https://doi.org/10.1016/j.cma.2021.113974

Hager M, Pistrol J, Kopf F, Adam D (2021) Verdichtung mit Vibrationswalzen. Semi-analytische Modellierung des Interaktionssystems Bandage-Boden mit Berücksichtigung der veränderlichen Bandagenaufstandsbreite. Bauingenieur 96:

Harris CR, Millman KJ, van der Walt SJ, et al (2020) Array programming with NumPy. Nature 585:357–362. https://doi.org/10.1038/s41586-020-2649-2

He X, Xu H, Sabetamal H, Sheng D (2020) Machine learning aided stochastic reliability analysis of spatially variable slopes. Comput Geotech 126:103711. https://doi.org/10.1016/j.compgeo.2020.103711

Houlsby GT (1997) The work input to an unsaturated granular material. Geotechnique 47:193–196. https://doi.org/10.1680/geot.1997.47.1.193

Hu W, Jia X, Zhu X, et al (2020) Influence of moisture content on intelligent soil compaction. Autom Constr 113:103141. https://doi.org/10.1016/j.autcon.2020.103141

Hu W, Shu X, Huang B, Woods M (2017) Field investigation of intelligent compaction for hot mix asphalt resurfacing. Front Struct Civ Eng 11:47–55. https://doi.org/10.1007/s11709-016-0362-x

Imran SA, Barman M, Commuri S, et al (2018) Artificial neural network-based intelligent compaction analyzer for real-time estimation of subgrade quality. Int J Geomech 18:1–14. https://doi.org/10.1061/(ASCE)GM.1943-5622.0001089

Jaffar STA, Muneeb Abid M, Khan SZ, et al (2022) Evaluation of Conventional and Sustainable Modifiers to Improve the Stiffness Behavior of Weak Sub-Grade Soil. Sustainability 14:2493. https://doi.org/10.3390/su14052493

Jia X, Karpatne A, Willard J, et al (2018) Physics Guided Recurrent Neural Networks For Modeling Dynamical Systems: Application to Monitoring Water Temperature and Quality in Lakes. 8th Int Work Clim Informatics

Kang J, Zhaofeng C, Zhaoyu L, Wang SY (2021) Characterization of particle orientation of kaolinite samples using the deep learning-based technique. Acta Geotech 0123456789: https://doi.org/10.1007/s11440-021-01266-x

Kargl G (1995) Modellversuche zur Ermittlung des Last-Deformationsverhaltens geschichteter Modellböden unter ebenen und zylindrisch gekrümmten Belastungsflächen und vergleichende Computerberechnungen. TU Wien

Karpatne A, Atluri G, Faghmous JH, et al (2017a) Theory-Guided Data Science: A New Paradigm for Scientific Discovery from Data. IEEE Trans Knowl Data Eng 29:2318–2331. https://doi.org/10.1109/TKDE.2017.2720168

Karpatne A, Watkins W, Read J, Kumar V (2017b) Physics-guided Neural Networks (PGNN): An Application in Lake Temperature Modeling. arXiv Prepr arXiv171011431

Kenneally B, Musimbi OM, Wang J, Mooney MA (2015) Finite element analysis of vibratory roller response on layered soil systems. Comput Geotech 67:73–82. https://doi.org/10.1016/j.compgeo.2015.02.015

Kodikara J (2012) New framework for volumetric constitutive behaviour of compacted unsaturated soils. Can Geotech J 49:1227–1243. https://doi.org/10.1139/t2012-084

Kodikara J, Islam T, Sounthararajah A (2018) Review of soil compaction: History and recent developments. Transp Geotech 17:24–34. https://doi.org/10.1016/j.trgeo.2018.09.006

Kodikara J, Jayasundara C, Zhou AN (2020) A generalised constitutive model for unsaturated

compacted soils considering wetting/drying cycles and environmentally-stabilised line. Comput Geotech 118:103332. https://doi.org/10.1016/j.compgeo.2019.103332

Kolarik T, Rudorfer G (1994) Time series forecasting using neural networks. ACM Sigapl Apl Quote Quad 25:86–94

Kuczmann M, Iványi A (2008) The Finite Element Method in Magnetics. 308

Kumar D, Wong A, Taylor GW (2017) Explaining the Unexplained : A CLass-Enhanced Attentive Response (CLEAR). Arxiv 36–44

Laloy E, Javaux M, Vanclooster M, et al (2011) Electrical Resistivity in a Loamy Soil: Identification of the Appropriate Pedo-Electrical Model. Vadose Zo J 10:1023–1033. https://doi.org/10.2136/vzj2010.0095

Latter L, Rice Z, Andrews B (2019) Review of Density Compliance Systems for Subgrade and Embankment Construction - Stage 1, for Main Roads Western Australia

Lee J, Lacey D, Look B (2017) P60: Best practice in compaction QA for pavement and subgrade materials (year 1 – 2016/2017). www.nacoe.com.au. Accessed 25 May 2021

Lekarp F, Dawson A (1998) Modelling permanent deformation behaviour of unbound granular materials. Constr Build Mater. https://doi.org/10.1016/S0950-0618(97)00078-0

Li D, Selig ET (1994) Resilient Modulus for Fine-Grained Subgrade Soils. J Geotech Eng 120:939–957. https://doi.org/10.1061/(ASCE)0733-9410(1994)120:6(939)

Li N, Wang X, Qiao R, et al (2020) A prediction model of permanent strain of unbound gravel materials based on performance of single-size gravels under repeated loads. Constr Build Mater 246:118492. https://doi.org/10.1016/j.conbuildmat.2020.118492

Li Q, Garg N (2015) Evaluation of effect of rolling direction on unbound material modulus using portable seismic pavement analyzer (PSPA). In: Airfield and Highway Pavements 2015. pp 825–836

Li Q, Stein J, Garg N (2017) Characterization of Airfield Subbase Materials Using Precision Unbound Material Analyzer (PUMA). Airf Highw Pavements 370–381. https://doi.org/https://doi.org/10.1061/9780784480939.032

Liu D, Wang Y, Chen J, Zhang Y (2019) Intelligent compaction practice and development: a bibliometric analysis. Eng Constr Archit Manag 27:1213–1232. https://doi.org/10.1108/ECAM-05-2019-0252

Liu Z, Shao J, Xu W, Wu Q (2015) Indirect estimation of unconfined compressive strength of carbonate rocks using extreme learning machine. Acta Geotech 10:651–663. https://doi.org/10.1007/s11440-014-0316-1

Livneh M, Goldberg Y (2001) Quality Assessment During Road Formation and Foundation Construction: Use of Falling-Weight Deflectometer and Light Drop Weight. Transp Res Rec J Transp Res Board 1755:69–77. https://doi.org/10.3141/1755-08

Look BG (2020) Overcoming the current density testing impediment to alternative quality testing in earthworks. Aust Geomech J 55:55–74

Loret B, Khalili N (2002) An effective stress elastic-plastic model for unsaturated porous media. Mech Mater 34:97–116. https://doi.org/10.1016/S0167-6636(01)00092-8

Main Roads WA (2012) Dry Density: Sand Replacement Method. WA 3241

Main Roads WA (2013) Determination of Field Density: Nuclear Method. WA 3242

Main Roads WA (2008) Engineering Road Note 8. 1–15

Makasis N, Narsilio GA, Bidarmaghz A (2018) A machine learning approach to energy pile design. Comput Geotech 97:189–203. https://doi.org/10.1016/j.compgeo.2018.01.011

Manzanal D, Pastor M, Merodo JAF (2011) Generalized plasticity state parameter-based model for saturated and unsaturated soils. Part II: Unsaturated soil modeling. Int J Numer Anal Methods Geomech 35:1899–1917. https://doi.org/10.1002/nag.983

McKinney W (2010) Data structures for statistical computing in python. In: Proceedings of the 9th Python in Science Conference. pp 51–56

Meehan CL, Tehrani FS, Vahedifard F (2012) A comparison of density-based and modulus-based in situ test measurements for compaction control. Geotech Test J 35:387–399. https://doi.org/10.1520/GTJ103479

Modoni G, Koseki J, Anh Dan LQ (2011) Cyclic stress-strain response of compacted gravel.

Geotechnique 61:473–485. https://doi.org/10.1680/geot.7.00150

Monismith CL, Ogawa N, Freeme CR (1975) Permanent deformation characteristics of subgrade soils due to repeated loading. Transp Res Rec 537:

Mooney MA, Rinehart R V. (2007) Field Monitoring of Roller Vibration during Compaction of Subgrade Soil. J Geotech Geoenvironmental Eng 133:257–265. https://doi.org/10.1061/(asce)1090-0241(2007)133:3(257)

Neyamadpour A (2019) 3D electrical resistivity tomography as an aid in investigating gravimetric water content and shear strength parameters. Environ Earth Sci 78:. https://doi.org/10.1007/s12665-019-8603-7

Pandey LMS, Shukla SK, Habibi D (2015) Electrical resistivity of sandy soil. Géotechnique Lett 5:178–185. https://doi.org/10.1680/jgele.15.00066

Park J, Santamarina JC (2019) Sand response to a large number of loading cycles under zero-lateral-strain conditions: Evolution of void ratio and small-strain stiffness. Geotechnique 69:501–513. https://doi.org/10.1680/jgeot.17.P.124

Park SB, Lee JW, Kim SK (2004) Content-based image classification using a neural network. Pattern Recognit Lett 25:287–300

Pasten C, Shin H, Santamarina JC (2014) Long-term foundation response to repetitive loading. J Geotech Geoenvironmental Eng 140:1–11. https://doi.org/10.1061/(ASCE)GT.1943-5606.0001052

Pedregosa F, Varoquaux G, Gramfort A, et al (2011) Scikit-learn: Machine Learning in Python. J Mach Learn Res 12:2825–2830

Pestana JM, Whittle AJ (1995) Compression model for cohesionless soils. Géotechnique 45:611–631. https://doi.org/10.1680/geot.1995.45.4.611

Pestana JM, Whittle AJ, Salvati LA (2002) Evaluation of a constitutive model for clays and sands: Part I - sand behaviour. Int J Numer Anal Methods Geomech 26:1097–1121. https://doi.org/10.1002/nag.237

Plati C, Loizos A (2013) Estimation of in-situ density and moisture content in HMA pavements based on GPR trace reflection amplitude using different frequencies. J Appl

Geophys 97:3–10. https://doi.org/10.1016/j.jappgeo.2013.04.007

Pooya Nejad F, Jaksa MB (2017) Load-settlement behavior modeling of single piles using artificial neural networks and CPT data. Comput Geotech 89:9–21. https://doi.org/10.1016/j.compgeo.2017.04.003

Queensland Department of Transport and Main Roads (2017) Relative compaction of soils and crushed rock. Q140A

Rai R, Sahu CK (2020) Driven by Data or Derived through Physics? A Review of Hybrid Physics Guided Machine Learning Techniques with Cyber-Physical System (CPS) Focus. IEEE Access 8:71050–71073. https://doi.org/10.1109/ACCESS.2020.2987324

Raissi M, Karniadakis GE (2018) Hidden physics models: Machine learning of nonlinear partial differential equations. J Comput Phys 357:125–141. https://doi.org/10.1016/j.jcp.2017.11.039

Raissi M, Perdikaris P, Karniadakis GE (2017a) Machine learning of linear differential equations using Gaussian processes. J Comput Phys 348:683–693. https://doi.org/10.1016/j.jcp.2017.07.050

Raissi M, Perdikaris P, Karniadakis GE (2017b) Inferring solutions of differential equations using noisy multi-fidelity data. J Comput Phys 335:736–746. https://doi.org/10.1016/j.jcp.2017.01.060

Rezaie-Balf M, Kisi O (2018) New formulation for forecasting streamflow: Evolutionary polynomial regression vs. extreme learning machine. Hydrol Res 49:939–953. https://doi.org/10.2166/nh.2017.283

Roads and Marine Services N (2012a) Field density of road construction materials (Sand replacement method). T119

Roads and Marine Services N (2012b) Density in situ of road construction materials (fixed volume extractive method). T165

Roelofs R, Fridovich-Keil S, Miller J, et al (2019) A meta-analysis of overfitting in machine learning. Adv Neural Inf Process Syst 32:9179–9189

Sawicki A, Swidzinski W (1995) Cyclic compaction of soils, grains and powders. Powder

Technol 85:97–104. https://doi.org/10.1016/0032-5910(95)03013-Y

Schrefler BA (1984) The finite element method in soil consolidation. Doctoral disseratation, University College of Swansea

Standards Australia (2007) Soil compaction and density tests-Determination of field density and field moisture content of a soil using a nuclear surface moisture–Density gauge—Direct transmission mode. AS 1289581

Standards Australia (1998a) Methods of testing soils for engineering purposes soils — Disturbed samples — Standard method. AS 1289551 1–9

Standards Australia (1998b) Methods of testing soils for engineering purposes Soil compaction and density tests - Compaction control test - Density index method for a cohesionless material. AS 1289561 3:1–9

Standards Australia (2004) Soil compaction and density tests - Determination of the field density of a soil — Sand replacement method using a sand pouring can , with or without a volume displacer. AS 1289531

Standards Australia (2002) Soil classification tests— Determination of the soil particle density of combined soil fractions—Vacuum pycnometer method. AS 1289352

Standards Australia (2003) Soil compaction and density tests — Determination of the dry density / moisture content relation of a soil using modified compactive effort. AS 1289521 1–13

Standards Australia (2009) Soil classification tests- Determination of the particle size distribution of a soil—Standard method of analysis by sieving. AS 1289361

Standards Australia (2017) Soil compaction and density tests Determination of the dry density/moisture content relation of a soil using standard compactive effort. In: AS 1298.5.1.1

Swileam GS, Shahin RR, Nasr HM, Essa KS (2019) Assessment of soil variability using electrical resistivity technique for normal alluvial soils, Egypt. Plant Arch 19:905–912

Tatsuoka F, Gomes Correia A (2018) Importance of controlling the degree of saturation in soil compaction linked to soil structure design. Transp Geotech 17:3–23.

https://doi.org/10.1016/j.trgeo.2018.06.004

Tatsuoka F, Hashimoto T, Tateyama K (2021) Soil stiffness as a function of dry density and the degree of saturation for compaction control. Soils Found 61:989–1002. https://doi.org/10.1016/j.sandf.2021.06.007

Tompai Z (2008) Conversion between static and dynamic load bearing capacity moduli and introduction of dynamic target values. Period Polytech Civ Eng 52:97. https://doi.org/10.3311/pp.ci.2008-2.06

Tophel A, Walker JP, Dutta TT, et al (2023) Model development to Predict Dynamic Interactions of Roller and Geomaterial using Simulated Roller Compaction. Transp Geotech 39:100946. https://doi.org/10.1016/j.trgeo.2023.100946

Tophel A, Walker JP, Dutta TT, Kodikara J (2022) Theory-guided machine learning to predict density evolution of sand dynamically compacted under Ko condition. Acta Geotech. https://doi.org/10.1007/s11440-021-01431-2

Van Rossum G, Drake Jr FL (1995) Python reference manual. Centrum voor Wiskunde en Informatica Amsterdam

VicRoads (1998) Guide to general requirements for unbound pavement materials. Tech. Bull. 39

Wang N, Ma T, Chen F, Ma Y (2022) Compaction quality assessment of cement stabilized gravel using intelligent compaction technology — A case study. Constr Build Mater 345:128100. https://doi.org/10.1016/j.conbuildmat.2022.128100

Wang S, Zhao S, Al-Qadi IL (2018) Continuous real-time monitoring of flexible pavement layer density and thickness using ground penetrating radar. NDT E Int 100:48–54. https://doi.org/10.1016/j.ndteint.2018.08.005

Wang Y, Salehi S (2015) Application of Real-Time Field Data to Optimize Drilling Hydraulics Using Neural Network Approach. J Energy Resour Technol 137:. https://doi.org/10.1115/1.4030847

Weber JJ (2018) Compaction Testing of Granular Material. South Dakota State University

Wheeler SJ, Sharma RS, Buisson MSR (2003) Coupling of hydraulic hysteresis and stress-

strain behaviour in unsaturated soils. Geotechnique 53:41–54. https://doi.org/10.1680/geot.2003.53.1.41

Wheeler SJ, Sivakumar V (1995) An elasto-plastic critical state framework for unsaturated soil. Geotechnique 45:35–53. https://doi.org/10.1680/geot.1995.45.1.35

White DJ, Vennapusa PK., Thompson MJ (2007) Field Validation of Intelligent Compaction Monitoring Technology for Unbound Materials. Partnership 515:294–8103

Wichtmann T (2005) Explicit accumulation model for non-cohesive soils under cyclic loading. PhD Thesis, Inst für Grundbau und Bodenmechanik Phd:274

Xu G, Chang GK (2020) Continuous Compaction Control – Mathematical Models and Parameter Identification. In: Springer Series in Geomechanics and Geoengineering. pp 563–584

Xu Q, Chang GK, Gallivan VL (2012) Development of a systematic method for intelligent compaction data analysis and management. Constr Build Mater 37:470–480. https://doi.org/10.1016/j.conbuildmat.2012.08.001

Yin H, Tan C, Zhang W, et al (2023) Rapid Compaction Monitoring and Quality Control of Embankment Dam Construction Based on UAV Photogrammetry Technology: A Case Study. Remote Sens 15:1–20. https://doi.org/10.3390/rs15041083

Yu H-S (2007) Plasticity and geotechnics. Springer Science & Business Media

Yuan G, Che A, Feng S (2020) Evaluation method for the physical parameter evolutions of highway subgrade soil using electrical measurements. Constr Build Mater 231:117162. https://doi.org/10.1016/j.conbuildmat.2019.117162

Zargar M, Lee J (2019) P105: Implementation of Intelligent Compaction Technology in Queensland (Year 1 – 2018/2019) for Asphalt Applications

Zhang P, Jin ZYY (2021) Modelling the mechanical behaviour of soils using machine learning algorithms with explicit formulations. Acta Geotech 4:. https://doi.org/10.1007/s11440-021-01170-4

Zhang P, Yin Z-Y, Jin Y-F (2021) State-of-the-Art Review of Machine Learning Applications in Constitutive Modeling of Soils. Arch Comput Methods Eng 1–26.

https://doi.org/10.1007/s11831-020-09524-z

Zhang Y, Wang R, Zhang J-M, Zhang J (2020) A constrained neural network model for soil liquefaction assessment with global applicability. Front Struct Civ Eng 14:1066–1082. https://doi.org/10.1007/s11709-020-0651-2